

The Pennsylvania State University  
The Graduate School  
Department of Chemical Engineering

**SULFUR TOLERANCE ENHANCEMENT OF STEAM REFORMING  
BY BINARY METAL CATALYSTS**

A Dissertation in  
Chemical Engineering  
by  
Kyungtae Lee

© 2013 Kyungtae Lee

Submitted in Partial Fulfillment  
of the Requirements  
for the Degree of

Doctor of Philosophy

August 2013

The dissertation of Kyungtae Lee was reviewed and approved\* by the following:

Michael J. Janik  
Associate Professor of Chemical Engineering  
Dissertation Advisor  
Chair of Committee

Robert M. Rioux  
Friedrich G. Helfferich Assistant Professor of Chemical Engineering

Enrique D. Gomez  
Assistant Professor of Chemical Engineering

Chunshan Song  
Professor of Energy and Mineral Engineering & Director of Earth and Mineral Sciences Energy  
Institute

Andrew L. Zydney  
Walter L. Robb Chair and Professor of Chemical Engineering  
Head of the Department of Chemical Engineering

\*Signatures are on file in the Graduate School

## ABSTRACT

Hydrogen ( $H_2$ ) as one of promising clean energy carriers is mainly produced by steam reforming reactions. A steam reformer can be combined with fuel cells for an on-board or on-site hydrogen production and fuel cell conversion to electricity. These fuel cell systems may preferentially use liquid hydrocarbon fuels such as jet or diesel fuel as feedstocks due to the high gravimetric and volumetric energy density of liquid fuels. A major challenge of these systems is to overcome sulfur poisoning of reforming catalysts caused by sulfur compounds inherently present in liquid fuels. There are two ways to resolve the sulfur poisoning problem, the use of a desulfurization processor and the development of sulfur tolerant reforming catalysts. This dissertation focuses on sulfur tolerant catalysts. Sulfur tolerant catalysts either facilitate a compact reforming system by removing a desulfurization unit or further improve the sulfur tolerance of reforming reactions with a desulfurization unit.

Recent experimental results demonstrate that addition of Ni to Rh catalysts provides a higher sulfur tolerance than pure Rh catalysts. Characterizations using TPD and XPS prove that the sulfur tolerant Rh-Ni catalysts exist as a bimetallic form, however it necessitates a further study of the sulfur tolerance mechanism. This dissertation examines the mechanistic source of sulfur tolerance for bimetallic Rh-Ni catalysts using the density functional theory (DFT) methods, ab initio thermodynamics, and microkinetic modeling. This dissertation considers four metal surfaces including pure Rh, pure Ni, and binary  $Rh_1Ni_2$ ,  $Rh_2Ni_1$  with (111) and (221) facets for flat and stepped surfaces, respectively. As methane formation during steam reforming is most sensitive to sulfur poisoning, the kinetics of CO dissociation is analyzed on four metal surfaces by comparing sulfur-free and sulfur-poisoned conditions. Various sulfur poisoning species are also examined to find the thermodynamically favorable poisoning path using ab initio thermodynamics. The steam reforming of liquid hydrocarbon is modeled using propane steam reforming reactions. The potential energy surface along elementary steps of propane reforming is constructed using Brønsted-Evans-Polanyi (BEP) relations. Rh-Ni bimetallic surfaces enhance sulfur tolerance by retarding increases of activation barriers due to sulfur poisoning and lowering S coverage.

## TABLE OF CONTENTS

LIST OF FIGURES .....	vii
LIST OF TABLES .....	xi
ACKNOWLEDGEMENTS .....	xii
Chapter 1 Introduction:	
Enhanced sulfur tolerance in steam reforming by Rh-Ni catalyst .....	1
1.1 Background .....	1
1.2 Research Objectives .....	5
1.3 Summary of Chapters .....	8
1.4 References .....	10
Chapter 2 Density Functional Theory Study of Sulfur Tolerance of CO Adsorption and Dissociation on Rh-Ni Binary Metals .....	
2.1 Introduction .....	15
2.2 Methods .....	17
2.3 Results and Discussion .....	20
2.3.1 Adsorption energy of S and CO on (111) surfaces of Rh, Ni pure and binary metals .....	20
2.3.2 Influence of sulfur coadsorption on CO, C, and O adsorption energies to Rh(111) .....	22
2.3.3 Expression for the apparent CO dissociation rate used to compare among metals .....	24
2.3.4 CO dissociation configurations .....	26
2.3.5 Energetics of CO dissociation .....	26
2.3.6 Projected Density of State (PDOS) analysis .....	30
2.3.7 CO dissociation on stepped surfaces .....	33
2.4 Conclusions .....	35
2.5 References .....	36
2.6 Supporting Information .....	39
Chapter 3 An ab initio thermodynamics examination of sulfur species present on Rh, Ni, and binary Rh-Ni surfaces under steam reforming reaction conditions .....	
	41

3.1 Introduction.....	42
3.2 Methods.....	44
3.2.1 Electronic structure methods.....	44
3.2.2 Model construction. ....	45
3.2.3 Gibbs free energy determination.....	47
3.3 Results and Discussion .....	51
3.3.1 SO <sub>x</sub> (x=0~4) adsorption on Rh and Ni surfaces at 1/9 coverage.....	51
3.3.2 Sulfidation phase diagram of pure Rh and Ni metals.....	53
3.3.3 Rh-Ni binary metal surfaces at varying S* coverage.....	55
3.3.4 Rh(221) stepped surfaces and Rh <sub>4</sub> /CeO <sub>2</sub> (111). ....	57
3.4 Conclusions.....	63
3.5 References.....	64
3.6 Supporting Information.....	68
Chapter 4 Density functional theory study of propane steam reforming on Rh-Ni binary metals: Sulfur tolerance and scaling/ Brønsted-Evans-Polanyi relations .....	70
4.1 Introduction.....	71
4.2 Methods.....	74
4.2.1 Computational methods .....	74
4.2.2 Scaling and BEP relations.....	75
4.3 Results and Discussion .....	78
4.3.1 Propane reforming reaction path.....	78
4.3.2 Transition states .....	80
4.3.3 Application of scaling and BEP relations .....	83
4.3.4 Application of BEP relation without using scaling relation.....	87
4.3.5 Energy profile of propane steam reforming.....	88
4.3.6 Sulfur tolerance of Rh-Ni binary metals .....	91
4.4 Conclusions.....	94
4.5 References.....	95
4.6 Supporting Information.....	98
Chapter 5 Summary, Conclusions, and Recommendations for Future Study .....	103

5.1 Sulfur poisoning species and sulfur tolerance on Rh-Ni binary catalysts.....	103
5.2 Propane steam reforming on sulfur tolerant Rh-Ni binary catalysts.....	105
5.3 Answers for Research Questions .....	106
5.4 Perspective and Suggestions for Future Study .....	108
5.5 References.....	110

## LIST OF FIGURES

Figure 1-1. Schematic diagram of a fuel cell system combined with an on-site or on-board external reformer which converts jet fuel (JP-8) into hydrogen gas.....	2
Figure 1-2. Catalytic fuel conversion for steam reforming of 100 ppmS NORPAR-13 (NORPAR-13 is a normal paraffin with an average carbon number of 13) and the effect of Ni loading level on the sulfur tolerance of 2 % Rh–X% Ni/CeO <sub>2</sub> –Al <sub>2</sub> O <sub>3</sub> catalyst. X = 0, 2, 5, 10 and 20 wt%. For additional comparison, a catalyst with 2% Rh loaded on calcined 10% Ni/CeO <sub>2</sub> –Al <sub>2</sub> O <sub>3</sub> is also presented (2% Rh on 10% Ni).....	4
Figure 2-1. Perspective view (left) and top view (right) of the Rh-Ni (111) surfaces (dark small sphere: Rh, light large sphere: Ni); (a) Rh <sub>2</sub> Ni <sub>1</sub> , (b) Rh <sub>1</sub> Ni <sub>2</sub> . There are six possible adsorption sites for an adsorbate, as shown in (a): N and R in parenthesis indicate a site located over a Ni metal atom and a Rh metal atom, respectively. ....	18
Figure 2-2. Adsorption of a CO molecule (left) and dissociated C and O (right) in (a) 1/4 ML S coverage and (b) 1/9 ML S coverage on the Rh (111) surface. S atoms are represented with light color, C atoms with grey color, and O atoms with dark color. Arrows indicate the movement of O atom during CO dissociation. ....	23
Figure 2-3. CO dissociation configurations on each metal surface. In configuration B, S atoms are located to have a closer interaction with adsorbed CO molecules than configuration A. Arrows indicate the path taken by the O atom during dissociation with the point residing on the final O adsorption site. (Rh and Ni: dark and light spheres in the substrate, respectively. C, O, S: grey, dark, and light spheres in the adsorbate layer, respectively.).....	27
Figure 2-4. Plot of the CO dissociation activation energy versus the CO adsorption energy for the various Ni, Rh, and Ni-Rh surfaces considered. The dotted circle line indicates the catalysts under sulfur-free conditions and the other points outside the dotted circle are for the catalysts in the presence of sulfur.....	29
Figure 2-5. Projected density of states of the O 2p orbital in the initial (CO adsorbed) and transition (CO dissociation) states on a) the Rh and c) Rh <sub>1</sub> Ni <sub>2</sub> surfaces (solid line: with sulfur, dotted line: without sulfur). The energy-weighted differences of (PDOS of O 2p × energy) values between the presence and absence of sulfur on b) the Rh and d) Rh <sub>1</sub> Ni <sub>2</sub> surfaces are plotted versus energy relative to vacuum. ....	31
Figure 2-6. Partial charge density images on pure Rh at (a) -11.8 eV and (b) -11.6 eV in the presence of S. The values above 1.0×10 <sup>-5</sup> in charge density were visualized for these images. (Rh is dark spheres in the substrate. C, O, and S: grey, dark, and light spheres in the adsorbates, respectively.) .....	31
Figure 2-7. Initial (left) and transition (right) states on (a) the Rh (221) and (b) Rh <sub>1</sub> Ni <sub>2</sub> (221) stepped surfaces. (Rh and Ni: dark and light spheres in the substrate, respectively. C, O, S: grey, dark, and white spheres in the adsorbate layer, respectively.).....	34

Figure 3-1. Structural images of (a)  $\text{Rh}_1\text{Ni}_2$  surface, (b)  $\text{Rh}_2\text{Ni}_1$  surface, (c) bulk  $\text{Ni}_3\text{S}_2$ , (d) bulk  $\text{Rh}_{17}\text{S}_{15}$ , and (e)  $\text{Rh}_4$  cluster on  $\text{CeO}_2(111)$  surface. ((a-d) dark gray sphere (green): Rh, light gray sphere (blue): Ni, white sphere (yellow): S. (e) large gray sphere (red): O, small gray sphere (green): Rh, white sphere (white): Ce.) ..... 47

Figure 3-2. The most preferred adsorption configurations of S, SO,  $\text{SO}_2$ ,  $\text{SO}_3$ , and  $\text{SO}_4$  (from left to right) on Rh (top) and Ni (bottom) at 1/9 ML coverage. .... 51

Figure 3-3. Free energy changes for adsorption of S, O,  $\text{SO}_x$  ( $x=1, 2, 3, 4$ ) are calculated via Eq. 6 and plotted versus pressure of  $\text{H}_2\text{S}$  gas on Rh(111) at (a) 500 and (b) 1000 K, and Ni(111) at (c) 500 and (d) 1000 K. The shaded regions represent  $\text{H}_2\text{S}$  pressures over which the bulk metal sulfides ( $\text{Rh}_{17}\text{S}_{15}$  or  $\text{Ni}_3\text{S}_2$ ) are determined to be stable. Gas pressures used for this graphs were calculated to satisfy Eq. 2 at varying  $\text{H}_2\text{S}$  pressures:  $P(\text{H}_2\text{O})=0.411\sim0.415$  atm,  $P(\text{H}_2)=0.347\sim351$  atm,  $P(\text{CH}_4)=0.0925\sim0.0935$  atm,  $P(\text{CO}_2)=0.1157\sim0.1169$  atm,  $P(\text{CO})=0.0231\sim0.0234$  atm, and  $P(\text{H}_2\text{S})=1.07\times10^{-2}\sim1.80\times10^{-11}$  atm. .... 53

Figure 3-4. Sulfidation phase diagrams of (a) Rh (thick solid and short-dashed lines, red) and Ni (thin solid and short-dashed lines, blue), (b) comparison of our calculated Ni(111) phase diagram (thick solid and short-dashed lines, blue) with literature data: experimental data for the  $\text{S}^*$ -clean surface transition ( $\blacktriangle$ ) and bulk sulfide formation (thick long-dashed line, red) and Wang et al.'s calculation for the  $\text{S}^*$ -clean surface transition (thin solid line, green) and bulk sulfide formation (thin short-dashed line, green) ..... 55

Figure 3-5. (a) Phase diagram of 1/9 ML to “clean surface” transition of Rh (solid line, red), Ni (long-dashed line, blue),  $\text{Rh}_1\text{Ni}_2$  (short-dashed line, green), and  $\text{Rh}_2\text{Ni}_1$  (dotted line, black) (111) surfaces. (b) Phase diagram of Rh (thick solid and short-dashed lines, red) and  $\text{Rh}_1\text{Ni}_2$  (thin solid and short-dashed lines, green) at various sulfur coverages with an indication of the experimental conditions studied by Strohm et al [6]. (clean to 1/9 ML S coverage: solid line, 1/9 to 1/3 ML S coverage: dashed line). .... 57

Figure 3-6. Phase diagrams of considering  $\text{S}^*$ ,  $\text{O}^*$ , and  $\text{SO}_x^*$  adsorption on (a) Rh(111) and (b) Ni(111) surfaces at various temperatures under a high  $\text{O}_2$  pressure ( $P(\text{O}_2) = 0.17$  atm). Other gas pressures used here were calculated based on Eq. 2:  $P(\text{H}_2)=0.629\sim0.634$  atm,  $P(\text{CH}_4)=0.0768\sim0.0774$  atm,  $P(\text{CO}_2)=0.0959\sim0.0968$  atm,  $P(\text{CO})=0.0192\sim0.0194$  atm,  $P(\text{H}_2\text{S})=8.86\times10^{-3}\sim1.49\times10^{-11}$  atm. .... 59

Figure 3-7. DFT optimized structures of  $\text{SO}_4$  adsorbed at the step-top site of the Rh(221) surface. .... 59

Figure 3-8. DFT optimized structures for adsorption of (a) S and (b)  $\text{SO}_4$  on a  $\text{Rh}_4$  cluster on the  $\text{CeO}_2(111)$  surface and (c) adsorption of  $\text{SO}_4$  on a  $\text{Rh}_4$  cluster on the  $\text{CeO}_2(111)$  surface with an O vacancy ... 62

Figure 3-9. Phase diagrams of Rh flat surface and a  $\text{Rh}_4$  cluster on ceria surface with an oxygen vacancy at (a) 500 K and (b) 1000 K. S adsorption on the Rh flat surface included various sulfur coverages such as 1/3, 1/4, and 1/9 ML. The gas pressures used here are the same with those of Figure 3-3. .... 63

Figure 4-1 Initial and final states of C-C dissociation of propyne (a, b), propynyl (c, d),  $\text{CH}_2\text{C}^*$  (e, f), and  $\text{CHC}^*$  (g, h) on the  $\text{Rh}_1\text{Ni}_2(111)$  surface. Dark-gray spheres (green), Rh; large light-gray sphere (blue), Ni; small light-gray spheres (gray), C; white spheres (white), H. .... 79



Figure 4-2. Initial (top), transition (middle top), final (middle bottom) states, and initial states with co-adsorbed sulfur (bottom) on the Rh(111) surface of C-H dissociation of (a) propane and (b) CHOH; C-O dissociation of (c) CHO and (d) CO; O-H dissociation of (e) COH and (f) OH; C-C dissociation of (g) propyne and (h) propynyl. Large gray sphere (green), Rh; small gray spheres (gray), C; white spheres (white), H; dark sphere (red), O; light gray sphere (yellow), S. .... 81

Figure 4-3. Comparison of three different BEP plots according to reaction types (C-H dissociation, a; O-H dissociation, b; C-C dissociation, c; C-O dissociation, d; C-OH dissociation, e) on Rh(111); Left plots are  $E_a$  (activation barrier) versus  $E_{rxn}$  (reaction energy), middle plots are  $E_{TS}$  (relative transition state energy) versus  $E_{IS}$  (relative initial state energy), and right plots are  $E_{TS}$  versus  $E_{FS}$  (relative final state energy). Relative energies are based on the reference state of propane gas, steam, and a corresponding metal surface. .... 84

Figure 4-4. Comparison between the  $E_a$  estimates (blue solid bar) (by scaling and BEP relations, a and c; by BEP relations only, b and d) and DFT  $E_a$  values (red diagonal striped bar) for two C-H dissociation reactions of CHOH (a, b) and CHO (c, d). The difference between the two values is indicated by a green horizontal striped bar with a number indicating the size of the bar. Estimation accuracy is compared in e, f by plotting activation barrier estimates (by scaling and BEP relations, e; by BEP relations only, f) versus DFT-calculated barriers for the C-H dissociation reactions of both CHOH and COH. .... 85

Figure 4-5. Deviation levels of initial (a) and final (b) state energies estimated by scaling relationships from DFT-calculated values on each metal surface for seven elementary steps;  $\text{CHOH}^* \rightarrow \text{COH}^* + \text{H}^*$ ,  $\text{CHO}^* \rightarrow \text{CO}^* + \text{H}^*$ ,  $\text{CHOH}^* \rightarrow \text{CH}^* + \text{OH}^*$ ,  $\text{CHO}^* \rightarrow \text{CH}^* + \text{O}^*$ ,  $\text{CO}^* \rightarrow \text{C}^* + \text{O}^*$ ,  $\text{COH}^* \rightarrow \text{CO}^* + \text{H}^*$ , and  $\text{OH}^* \rightarrow \text{O}^* + \text{H}^*$ . The boxes represent the middle 50 % of the data points (i.e. the bottom and top boundaries of a box indicate a lower quartile and an upper quartile, respectively) and the line in the box indicates the median. The minimum and maximum values among a given data set are indicated by whiskers. .... 86

Figure 4-6. Deviation of activation barriers estimated by various estimation methods from DFT  $E_a$  values calculated by the NEB method on each metal for the C-H dissociation reactions of CHOH (a) and CHO (b), the C-OH dissociation reaction of CHOH (c), and seven elementary steps (d) which are  $\text{CHOH}^* \rightarrow \text{COH}^* + \text{H}^*$ ,  $\text{CHO}^* \rightarrow \text{CO}^* + \text{H}^*$ ,  $\text{CHOH}^* \rightarrow \text{CH}^* + \text{OH}^*$ ,  $\text{CHO}^* \rightarrow \text{CH}^* + \text{O}^*$ ,  $\text{CO}^* \rightarrow \text{C}^* + \text{O}^*$ ,  $\text{COH}^* \rightarrow \text{CO}^* + \text{H}^*$ , and  $\text{OH}^* \rightarrow \text{O}^* + \text{H}^*$ . SR, scaling relations; BEP(I), use of an identical BEP relation for all metals for a given reaction type; BEP(II), use of a different BEP relation for each metal for a given reaction type. .... 88

Figure 4-7. Energy profile of propane steam reforming reaction estimated by the BEP relation on four metal surfaces under sulfur free condition (a) and under sulfur poisoned condition (b). The relative energy of each intermediate is defined by Eq. 7. .... 90

Figure 4-8. Average activation barriers of elementary steps along the preferred reaction paths of propane steam reforming reaction on sulfur-poisoned four metal surfaces. .... 92

Figure 4-9. Comparison of activation barriers across metals for four elementary reactions with high activation barriers along the reaction path of propane steam reforming..... 92

Figure 4-10. Average activation barrier changes on each metal due to co-adsorbed S\* according to reaction types including (a) dissociation of O-H, C-H, C-C bonds and (b) association of C-H, C-O bonds. (c) Average destabilization levels of all elementary reactions on each metal. .... 93

## LIST OF TABLES

Table 1-1. Comparison of reforming technologies .....	2
Table 2-1. Adsorption energies ( $\Delta E_{ads}$ , eV) and bond distances ( $\text{\AA}$ ) for S and CO adsorbed to high symmetry sites on Ni, Rh monometallic and Ni-Rh bimetallic (111) surfaces.....	21
Table 2-2. Adsorption energies of CO and C + O on the Rh (111) surface in the presence of S. Adsorption energies calculated by Zhang et al. are shown in parenthesis. The reference states for the calculation of $\Delta E_{ads}^{w/o S}$ and $\Delta E_{ads}^{w/ S}$ use the energy of an isolated CO molecule for the initial state and the energies of isolated C and O atoms for the final state. ....	23
Table 2-3. Relative CO dissociation rate, activation energy of CO dissociation and adsorption energies of CO on each metal surface. CO dissociation rates were calculated at the reaction temperature of 773.15 K. ....	28
Table 2-4. Differences in the integrated energy-weighted PDOS ( $E_{inv}$ , equation (9)) between the sulfur free and sulfur coadsorbed conditions on Rh and Rh <sub>1</sub> Ni <sub>2</sub> . ....	32
Table 2-5. Adsorption energies of S and CO, activation energies of CO dissociation, and CO dissociation rates on Rh and Rh <sub>1</sub> Ni <sub>2</sub> (221) stepped surfaces. CO dissociation rates were calculated at the reaction temperature of 773.15 K, and are given as relative values to the CO dissociation rate on the Rh(111) surface .....	34
Table 3-1. Adsorption energies and bond lengths of SO <sub>x</sub> adsorption at the most preferred sites on the Rh(111) and Ni(111) surfaces.....	52
Table 3-2. Gibbs free energy changes (eV) of S and SO <sub>4</sub> adsorption from H <sub>2</sub> S and H <sub>2</sub> O gases on Rh and Ni (111) and (221) surfaces as well as a Rh cluster on the ceria surface. All free energies were calculated at 1000 K and gas pressures of P(H <sub>2</sub> O)=0.42 atm, P(H <sub>2</sub> )=0.35 atm, P(CH <sub>4</sub> )=0.09 atm, P(CO <sub>2</sub> )=0.12 atm, P(CO)=0.02 atm, and P(H <sub>2</sub> S)=3.24×10 <sup>-6</sup> atm. ....	60
Table 4-1. DFT calculated activation energies ( $E_a$ , eV) and reaction energies ( $E_{rxn}$ , eV) on each metal surface classified according to reaction type. ....	82
Table 4-2. Representative BEP relations on each metal according to reaction types where $a$ and $b$ indicate slope and intercept in a BEP plot, respectively.....	83

## ACKNOWLEDGEMENTS

I'd like to thank my advisor Michael Janik for all his passionate help and kind advice to develop my scientific thinking/communication and guide me to my next career during my Ph.D. studies. He is an excellent educator, dedicating his time and talents to teaching. I feel very lucky to have him as my advisor. I thank Chunshan Song who funded my five-year study and provides experimental information to improve my computational research. I am grateful to my senior students to teach me computational techniques and share their academic experience with me. I mention in particular Adam Mayernick, Gholamreza Rostamikia, and Kuan-Yu Yeh. I also appreciate other members of the Janik lab and wish the best to them, specifically Matthew Krcha, Tomas Senftle, Huai-Suen Shiau, Nate Gifford, Hao Kuang, Sneha Akhade, and Ian McCrum with whom I've been able to enjoy computational study and laboratory life. I owe a debt of gratitude to Eunmin Lee who contributed to completing numerous calculation data to establish the potential energy surfaces of propane steam reforming. I had the pleasure of mentoring and learning from him. It was my great pleasure to work with smart and kind people in Penn State, and the experience will undoubtedly be a valuable asset for my future life.

I want to thank my family in my home country who has made sacrifices to support my Ph.D. study while living away from me, my wife, and my son. Finally, I'd like to thank my wife and my son who have always encouraged and loved me during my entire study. I devote this dissertation to them.

## **Chapter 1**

### **Introduction:**

### **Enhanced sulfur tolerance in steam reforming by Rh-Ni catalyst**

#### **1.1 Background**

Hydrogen ( $H_2$ ) is considered as one of major carriers of clean energy in the future due to the possibility of efficient and environmentally friendly energy conversion of hydrogen gas.<sup>1</sup> Hydrogen is produced from hydrocarbon energy sources, primarily through steam reforming, autothermal reforming, and partial oxidation (POX).<sup>2,3</sup> Table 1-1 summarizes the advantages and disadvantages of these processes. Among them, the steam reforming of natural gas accounts for most of industrial hydrogen production<sup>4</sup> because it offers higher selectivity to hydrogen at a lower operating temperature and from a compact system due to no need for an air compressor.<sup>5</sup> With such advantages of steam reforming, it can be combined with a fuel cell system for on-board and on-site fuel cell applications as shown in Figure 1-1.<sup>6</sup> Hydrogen gas can be used to generate electricity for fuel cells (e.g., proton exchange fuel cells (PEMFC) and solid oxide fuel cells (SOFC)).<sup>7</sup> This integrated reformer-fuel cell system catalyzes various feedstock including natural gas, liquid hydrocarbons or alcohols.<sup>8-10</sup> Especially, liquid hydrocarbon fuels such as jet fuels and diesel fuels are suitable for on-board/site electricity supply because of the high energy density of the liquid fuels with the advantages of safety, handling, and established infrastructures.

Our study was funded by the U.S. Department of Energy (DOE) for research and development of an integrated reformer (diesel or biogas feed) and SOFC system.

Table 1-1. Comparison of reforming technologies.<sup>5</sup>

Technology	Advantages	Disadvantages
Steam reforming	<ul style="list-style-type: none"> <li>✓ Most extensive industrial experience</li> <li>✓ Oxygen not required</li> <li>✓ Lowest process temperature</li> <li>✓ Best H<sub>2</sub>/CO ratio for H<sub>2</sub> production</li> </ul>	<ul style="list-style-type: none"> <li>✓ High CO<sub>2</sub> emissions</li> </ul>
Autothermal reforming	<ul style="list-style-type: none"> <li>✓ Lower process temperature than POX</li> <li>✓ Low methane slip</li> </ul>	<ul style="list-style-type: none"> <li>✓ Limited commercial experience</li> <li>✓ Requires air or oxygen</li> </ul>
Partial oxidation (POX)	<ul style="list-style-type: none"> <li>✓ Decreased desulfurization requirement</li> <li>✓ No catalyst required</li> <li>✓ Low methane slip</li> </ul>	<ul style="list-style-type: none"> <li>✓ Low H<sub>2</sub>/CO ratio</li> <li>✓ Very high processing temperatures</li> <li>✓ Soot formation/handling adds process complexity</li> </ul>

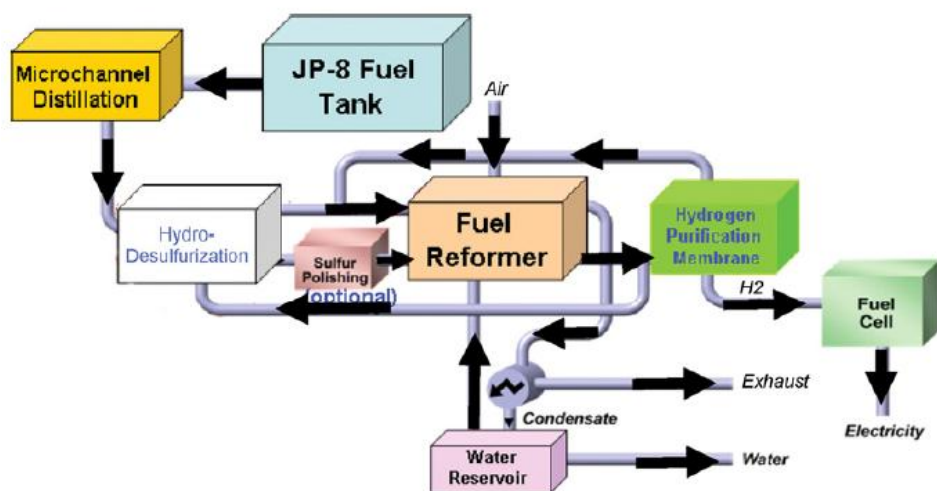


Figure 1-1. Schematic diagram of a fuel cell system combined with an on-site or on-board external reformer which converts jet fuel (JP-8) into hydrogen gas.<sup>6</sup>

Steam reforming catalysts encounter four challenges including limited catalytic activity, sulfur poisoning, carbon deposits, and catalyst particle sintering.<sup>11</sup> Among them, sulfur poisoning is a major challenge in the steam reforming of liquid hydrocarbon fuels as jet fuel and diesel fuel inherently contain a certain amount of sulfur compounds which mainly consist of benzothiophene derivatives.<sup>12</sup> During reforming catalysis, sulfur poisoning species arise from the sulfur compounds and accumulate on catalyst surfaces due to strong sulfur adsorption.<sup>13,14</sup> As a result, the reforming catalysts lose their catalytic activity for the reforming reaction, whereas activity for carbon deposit formation continues and eventually catalytic sites are blocked.<sup>15</sup> The sulfur content in fuels can be reduced to a few hundred ppm level using desulfurization processes such as hydrodesulfurization, selective alkylation of organo-sulfur molecules, and adsorptive approaches, however they increase the complexity of a total process to limit an industrial scale-up, and cannot completely remove sulfur contents in fuels.<sup>12,16,17</sup> Another approach to resolve the sulfur poisoning problem is to develop sulfur tolerant catalysts, which allows for either a simpler system by eliminating a desulfurization process or a better sulfur-resistant system with a desulfurization process.

Sulfur tolerance of catalysts can be enhanced by bimetallic structures that alter properties of pure metals by various compositional and morphological configurations.<sup>18-20</sup> Recently, several experimental studies have reported the combination effect of Rh and Ni<sup>21-23</sup> where non-noble Ni, as a catalyst widely used in the industrial steam reforming, provides low-cost with high activity and noble Rh reduces the carbon deposit formation problem prevalent on pure Ni catalysts during liquid hydrocarbon reforming. With these advantages, Strohm et al. demonstrated that addition of Ni to a Rh catalyst supported on CeO<sub>2</sub>-modified Al<sub>2</sub>O<sub>3</sub> enhances the sulfur tolerance of reforming catalysts.<sup>24</sup> When a Rh catalyst only is used, the fuel conversion reached over 97%

under sulfur-free conditions, but rapidly dropped in the sulfur content over 15 ppmS, indicating the weak resistance of Rh to sulfur poisoning. Such deactivation was prevented by adding Ni to Rh with the best performance of 2 wt%Rh-10 wt% Ni (Rh/Ni atomic ratio of 0.1) as shown in Figure 1-2. With such strong sulfur resistance, the Rh-Ni catalysts also minimize carbon formation, unlike Ni catalysts showing a drastic pressure drop across a reactor due to extensive carbon formation on the catalyst surface. The Rh-Ni catalysts are present as a bimetallic structure which is verified by various experimental analysis tools such as temperature-programmed reduction (TPR) and X-ray photoelectron spectroscopy (XPR), however the mechanism of their high sulfur tolerance is still unclear. In this study, we use density functional theory (DFT) methods to elucidate the elementary mechanism of the high sulfur tolerance over Rh-Ni catalysts. DFT methods enable us to investigate elementary steps and key intermediates during steam reforming which are difficult to identify experimentally.

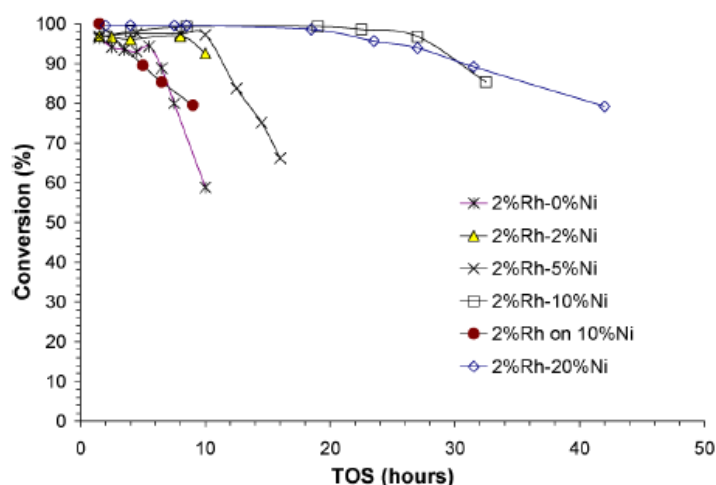


Figure 1-2. Catalytic fuel conversion for steam reforming of 100 ppmS NORPAR-13 (NORPAR-13 is a normal paraffin with an average carbon number of 13) and the effect of Ni loading level on the sulfur tolerance of 2 % Rh–X% Ni/CeO<sub>2</sub>–Al<sub>2</sub>O<sub>3</sub> catalyst. X = 0, 2, 5, 10 and 20 wt%. For additional comparison, a catalyst with 2% Rh loaded on calcined 10% Ni/CeO<sub>2</sub>–Al<sub>2</sub>O<sub>3</sub> is also presented (2% Rh on 10% Ni).<sup>24</sup>



## 1.2 Research Objectives

Interestingly, during the reforming of sulfur-doped fuels, methane selectivity declines before a drop in fuel conversion, suggesting that methane formation is most sensitive to sulfur poisoning.<sup>24</sup> This is also found in the analysis of  $S_{\text{fuel}}/Rh_{\text{surf}}$  ratio ( $S_{\text{fuel}}$  and  $Rh_{\text{surf}}$  represent the amount of sulfur in the fuel and surface Rh, respectively) where the methane formation is deactivated at a 0.15 ratio as opposed to a 0.28-0.30 ratio for the overall reforming reaction. Strohm et al. suggested two possible routes for methane formation, hydrogenation of CO and C-C cleavage of hydrocarbons to  $C_1(CH_x)$  fragments followed by hydrogenation. The hydrogenation of CO is selected as our first study due to its simplicity as compared to the cleavage of hydrocarbons producing other short-chain hydrocarbons. CO dissociation is known to be a rate determining step for the hydrogenation of CO,<sup>25</sup> so we examine the impact of a co-adsorbed sulfur atom on CO adsorption and dissociation over Rh-Ni bimetallic surfaces using DFT methods.

A surface sulfur atom is used as the poisoning species in our CO dissociation study<sup>26</sup>, but we also examine whether there are other possible sulfur poisoning species present under steam reforming conditions. The sulfur compounds in liquid hydrocarbon fuels are converted into  $H_2S$  gas in a reducing environment,<sup>15</sup> from which a variety of sulfur poisoning species may be formed on catalyst surfaces. One possible sulfur poisoning path is through the formation of sulfur oxides (i.e.,  $SO_x$  ( $x=1\sim4$ )) as sulfur compounds are known to be converted into  $SO_2$  in an oxidizing environment.<sup>27</sup> Another path is through metal sulfide formation. Previous reports show that Ni catalysts turn into  $Ni_3S_2$  at lower temperatures and higher  $H_2S$  pressures than the conditions leading to S adsorption on the Ni surface.<sup>28-30</sup> The binary phase diagram<sup>31</sup> indicates the formation

of  $\text{Ni}_3\text{S}_2$  and  $\text{Rh}_{17}\text{S}_{15}$  at a sulfur/metal atomic ratio of 0.3 at 500 °C corresponding to the experimental conditions where sulfur poisoning begins to influence fuel conversion.<sup>24</sup> Thus, we consider  $\text{S}^*$ ,  $\text{SO}_x^*$  ( $x=1\sim4$ ), and metal sulfides ( $\text{Ni}_3\text{S}_2$  and  $\text{Rh}_{17}\text{S}_{15}$ ) to determine the thermodynamically preferred sulfur poisoning species and their surface coverage differences among pure metals (Rh, Ni) and binary metals ( $\text{Rh}_1\text{Ni}_2$ ,  $\text{Rh}_2\text{Ni}_1$ ) under steam reforming conditions. The ab initio thermodynamics approach, based on DFT results and statistical mechanics formulas, is used to examine the stability of the various sulfur poisoning species.

The CO dissociation step, as particularly relevant for methane production, is examined first, however it is essential to ultimately examine all elementary steps of steam reforming to understand the impact of S poisoning and bimetallic formulation. The reforming of long-chain liquid hydrocarbon fuels such as jet or diesel fuel<sup>32</sup> involves numerous elementary steps which require enormous computational cost for analysis. Thus, we choose propane ( $\text{C}_3\text{H}_8$ ) as a model fuel instead of longer chain liquid hydrocarbons for the energetic analysis of reforming reactions. Propane is the smallest alkane allowing us to probe C-C cleavage and C-H dissociation for both primary and secondary carbon atoms. Previous computational studies of steam reforming focused on C1, C2 hydrocarbons or alcohols.<sup>33-35</sup> Thus, our work for propane can offer insight into sulfur tolerance of other catalytic reactions such as biomass reforming and Fischer-Tropsch synthesis because these processes also include the cleavage and formation of C-H, C-O, and C-C bonds in long-chain hydrocarbons.

Though propane is considered herein for simplicity, propane reforming also entails numerous elementary steps. A previous report listed 36 elementary steps for steam reforming of methane, and propane reforming adds considerably beyond this number.<sup>36</sup> It takes tremendous efforts to calculate the energetics of all elementary steps in the propane reforming on all

interesting metal surfaces. Thus, we use scaling and Brønsted-Evans-Polanyi (BEP) relations as estimation methods to map out the potential energy surfaces of all elementary steps. Scaling relations correlate atomic binding energies with molecular binding energies, thereby predicting all the minima of potential energy surfaces.<sup>37-41</sup> All the maxima can be predicted by BEP relations which linearly relate reaction energies to activation barriers or initial (or final) state energies to transition state energies.<sup>37,42-44</sup> The entire energetics of propane reforming thus can be estimated by the combination of scaling and BEP relations simply using atomic binding energies on a metal surface of interest. It is, however, inevitable that these methods involve estimation errors. For this reason, most previous computational studies applied these methods for a wide range of pure transition metals where errors scattered over 1 eV throughout data points are acceptable.<sup>45-48</sup> Thus, we examine whether the combination of these estimation methods can be applicable over similar metal surfaces such as our system ranging from pure Rh, to binary  $\text{Rh}_1\text{Ni}_2$ ,  $\text{Rh}_2\text{Ni}_1$ , to pure Ni. In this study, this issue is discussed by comparing the combined use of scaling and BEP relations with the use of BEP relations only.

Finally, using the optimal estimation method, we construct the potential energy surface of propane steam reforming where we can identify kinetically significant reaction steps. By comparing the energetic data in the key elementary steps between pure metals and Rh-Ni binary metals, we elucidate the sulfur tolerance mechanism of Rh-Ni binary metals.

In this dissertation, the following questions are addressed;

- 1) Why do Rh-Ni binary catalysts maintain the catalytic activity for methane formation under sulfur poisoning condition while the methane selectivity is rapidly dropped on the Rh catalyst?

- 2) Why is the sulfur poisoning impact of co-adsorbed sulfur atom reduced on Rh-Ni binary metals compared to pure Rh?
- 3) Is there any difference in sulfur poisoning species and their surface coverage between pure metals and Rh-Ni binary metals under reforming conditions?
- 4) Which elementary steps and surface intermediates are critical in the propane steam reforming reaction?
- 5) Do Rh-Ni binary metals provide higher sulfur tolerance for the energetics of either critical steps or the overall reforming reactions?
- 6) What are important factors to design a new sulfur tolerant catalyst?

### 1.3 Summary of Chapters

This dissertation examines the mechanism of sulfur tolerant Rh-Ni binary metals for the CO dissociation step (Chapter 2), sulfur poisoning species (Chapter 3), and the propane steam reforming reaction (Chapter 4) by comparing pure Rh, Ni metals and binary  $\text{Rh}_1\text{Ni}_2$ ,  $\text{Rh}_2\text{Ni}_1$  metals. Two surface facets of (111) and (221) are used to model flat and stepped surfaces, respectively. In Chapter 2, we search preferred adsorption sites for sulfur adsorption on each metal and compare sulfur binding energies. Sulfur binding energy differences represent sulfur coverage differences on catalyst surfaces which are a key factor to determine sulfur poisoning levels. With a  $1/9$  ML S coverage, the adsorption energies and dissociation barriers of CO are compared between sulfur-free and sulfur-present conditions on both flat and stepped surfaces. These two energy parameters are substituted to a rate equation for CO dissociation, thus one can

see whether Rh-Ni binary metals provide the fastest CO dissociation rate in the presence of sulfur. Chapter 2 also illustrates electronic interactions between adsorbed CO and co-adsorbed S using partial charge density images based on the projected density of state (PDOS) analysis to clarify the mechanistic reason of the high sulfur tolerance of Rh-Ni binary metals.

Chapter 3 considers the thermodynamic stability of possible sulfur poisoning species such as S,  $\text{SO}_x$  ( $x=1\sim4$ ), and metal sulfides ( $\text{Ni}_3\text{S}_2$  and  $\text{Rh}_{17}\text{S}_{15}$ ) on each metal. We consider a broad range of experimental conditions by varying the range of computational  $\text{H}_2\text{S}$  pressure from  $1.0 \times 10^{-9}$  to  $6.0 \times 10^{-1}$  atm and temperature from 400 to 1800 K. Gibbs free energies of formation for each sulfur poisoning species were calculated using DFT energy values and statistical formulas to construct phase diagrams at various pressure and temperature conditions. In these phase diagrams, we reveal whether binary metals have different sulfur poisoning species from pure metals at specific experimental conditions of interest as a different poisoning species is likely to have a different sulfur poisoning impact on catalytic reactions. Additionally, since there are controversial experimental reports whether the preferred sulfur poisoning species on Rh is S or  $\text{SO}_4$ ,<sup>49-53</sup> the preference for  $\text{SO}_4$  formation on Rh are probed in various ways by constructing phase diagrams at high  $\text{O}_2$  pressures and calculating the binding energies of  $\text{SO}_4$  at either the Rh stepped surface or a Rh cluster supported on the  $\text{CeO}_2(111)$  surface.

The energetics of propane steam reforming is discussed in Chapter 4 and the entire potential energy surfaces are constructed using BEP relations. To find linear BEP relations, transition state searches were carried out for representative reactions of each reaction type such as C-H, C-O, O-H, and C-C dissociation. Chapter 4 also evaluates two estimation approaches, the BEP relation only and the combined use of BEP relations with scaling relations, to determine which approach is appropriate for our system. Mapping of the entire potential energy surfaces of

propane steam reforming is done for the important reaction paths chosen by referring to previous computation studies. Using the completed energetics of propane reforming, the sulfur tolerance mechanism of binary Rh-Ni metals is analyzed in terms of the impact of sulfur poisoning on both significant elementary steps and overall reactions. The results of this dissertation guide us to the important factors (i.e., key intermediates and elementary steps) to design new sulfur tolerant reforming catalysts. Chapter 5 summarizes all the conclusion of Chapter 2-4 and discusses recommendations for future work.

#### 1.4 References

- (1) Bockris, J. O. *Int J Hydrogen Energ* **2008**, *33*, 2129.
- (2) Bshish, A.; Yakooob, Z.; Narayanan, B.; Ramakrishnan, R.; Ebshish, A. *Chem Pap* **2011**, *65*, 251.
- (3) Trimm, D. L.; Onsan, Z. I. *Catal Rev* **2001**, *43*, 31.
- (4) Dal Santo, V.; Gallo, A.; Naldoni, A.; Guidotti, M.; Psaro, R. *Catal Today* **2012**, *197*, 190.
- (5) Holladay, J. D.; Hu, J.; King, D. L.; Wang, Y. *Catal Today* **2009**, *139*, 244.
- (6) Huang, X. W.; King, D. A.; Zheng, F.; Stenkamp, V. S.; TeGrotenhuis, W. E.; Roberts, B. Q.; King, D. L. *Catal Today* **2008**, *136*, 291.
- (7) Armor, J. N. *Appl Catal a-Gen* **1999**, *176*, 159.
- (8) Schadel, B. T.; Duisberg, M.; Deutschmann, O. *Catal Today* **2009**, *142*, 42.
- (9) Kang, I.; Bae, J.; Bae, G. *J Power Sources* **2006**, *163*, 538.

- (10) Palo, D. R.; Dagle, R. A.; Holladay, J. D. *Chem Rev* **2007**, *107*, 3992.
- (11) Sehested, J. *Catal Today* **2006**, *111*, 103.
- (12) Selvavathi, V.; Chidambaram, V.; Meenalkshisundaram, A.; Sairam, B.; Sivasankar, B. *Catal Today* **2009**, *141*, 99.
- (13) Hepola, J.; Simell, P. *Appl Catal B-Environ* **1997**, *14*, 305.
- (14) Inoglu, N.; Kitchin, J. R. *J Catal* **2009**, *261*, 188.
- (15) Lakhapatri, S. L.; Abraham, M. A. *Appl Catal a-Gen* **2009**, *364*, 113.
- (16) Bu, J.; Loh, G.; Gwie, C. G.; Dewiyanti, S.; Tasrif, M.; Borgna, A. *Chem Eng J* **2011**, *166*, 207.
- (17) Arias, M.; Laurenti, D.; Geantet, C.; Vrinat, M.; Hideyuki, I.; Yoshimura, Y. *Catal Today* **2008**, *130*, 190.
- (18) Oezaslan, M.; Heggen, M.; Strasser, P. *J Am Chem Soc* **2012**, *134*, 514.
- (19) Rizzi, M.; Furlan, S.; Peressi, M.; Baldereschi, A.; Dri, C.; Peronio, A.; Africh, C.; Lacovig, P.; Vesselli, E.; Comelli, G. *J Am Chem Soc* **2012**, *134*, 16827.
- (20) Nikolla, E.; Schwank, J.; Linic, S. *J Am Chem Soc* **2009**, *131*, 2747.
- (21) Kugai, J.; Velu, S.; Song, C. S. *Catal Lett* **2005**, *101*, 255.
- (22) Kugai, J.; Subramani, V.; Song, C. S.; Engelhard, M. H.; Chin, Y. H. *J Catal* **2006**, *238*, 430.
- (23) Li, Y.; Wang, X. X.; Xie, C.; Song, C. S. *Appl Catal a-Gen* **2009**, *357*, 213.
- (24) Strohm, J. J.; Zheng, J.; Song, C. S. *J Catal* **2006**, *238*, 309.
- (25) Engbaek, J.; Lytken, O.; Nielsen, J. H.; Chorkendorff, L. *Surf Sci* **2008**, *602*, 733.
- (26) Alfonso, D. R.; Cugini, A. V.; Sholl, D. S. *Surf Sci* **2003**, *546*, 12.
- (27) Cheekatamarla, P. K.; Lane, A. M. *J Power Sources* **2005**, *152*, 256.

- (28) Wang, J. H.; Liu, M. L. *Electrochem Commun* **2007**, 9, 2212.
- (29) Rosenqvist, T. *J Iron Steel I* **1954**, 176, 37.
- (30) Barbouth, N.; Oudar, J. *Cr Acad Sci C Chim* **1969**, 269, 1618.
- (31) Massalski, T. B.; Okamoto, H.; ASM International. *Binary alloy phase diagrams*; 2nd ed.; ASM International: Materials Park, Ohio, 1990.
- (32) Rothamer, D. A.; Murphy, L. *P Combust Inst* **2013**, 34, 3021.
- (33) Lin, S.; Xie, D. Q.; Guo, H. *J Phys Chem C* **2011**, 115, 20583.
- (34) Blaylock, D. W.; Zhu, Y. A.; Green, W. H. *Top Catal* **2011**, 54, 828.
- (35) Ribeiro, R. U.; Liberatori, J. W. C.; Winnishofer, H.; Bueno, J. M. C.; Zanchet, D. *Appl Catal B-Environ* **2009**, 91, 670.
- (36) Blaylock, D. W.; Ogura, T.; Green, W. H.; Beran, G. J. O. *J Phys Chem C* **2009**, 113, 4898.
- (37) Saliccioli, M.; Stamatakis, M.; Caratzoulas, S.; Vlachos, D. G. *Chem Eng Sci* **2011**, 66, 4319.
- (38) Ferrin, P.; Simonetti, D.; Kandoi, S.; Kunkes, E.; Dumesic, J. A.; Norskov, J. K.; Mavrikakis, M. *J Am Chem Soc* **2009**, 131, 5809.
- (39) Abild-Pedersen, F.; Greeley, J.; Studt, F.; Rossmeisl, J.; Munter, T. R.; Moses, P. G.; Skulason, E.; Bligaard, T.; Norskov, J. K. *Physical Review Letters* **2007**, 99.
- (40) Jones, G.; Studt, F.; Abild-Pedersen, F.; Norskov, J. K.; Bligaard, T. *Chem Eng Sci* **2011**, 66, 6318.
- (41) Saliccioli, M.; Chen, Y.; Vlachos, D. G. *J Phys Chem C* **2010**, 114, 20155.
- (42) Evans, M. G.; Polanyi, M. *T Faraday Soc* **1938**, 34, 0011.



- (43) Norskov, J. K.; Bligaard, T.; Logadottir, A.; Bahn, S.; Hansen, L. B.; Bollinger, M.; Bengaard, H.; Hammer, B.; Sljivancanin, Z.; Mavrikakis, M.; Xu, Y.; Dahl, S.; Jacobsen, C. J. H. *J Catal* **2002**, *209*, 275.
- (44) Loffreda, D.; Delbecq, F.; Vigne, F.; Sautet, P. *Angew Chem Int Edit* **2009**, *48*, 8978.
- (45) Jones, G.; Bligaard, T.; Abild-Pedersen, F.; Norskov, J. K. *J Phys-Condens Mat* **2008**, *20*.
- (46) Wang, S. G.; Temel, B.; Shen, J. A.; Jones, G.; Grabow, L. C.; Studt, F.; Bligaard, T.; Abild-Pedersen, F.; Christensen, C. H.; Norskov, J. K. *Catal Lett* **2011**, *141*, 370.
- (47) Andersson, M. P.; Bligaard, T.; Kustov, A.; Larsen, K. E.; Greeley, J.; Johannessen, T.; Christensen, C. H.; Norskov, J. K. *J Catal* **2006**, *239*, 501.
- (48) Studt, F.; Abild-Pedersen, F.; Wu, Q. X.; Jensen, A. D.; Temel, B.; Grunwaldt, J. D.; Norskov, J. K. *J Catal* **2012**, *293*, 51.
- (49) Chen, Y. S.; Xie, C.; Li, Y.; Song, C. S.; Bolin, T. B. *Phys Chem Chem Phys* **2010**, *12*, 5707.
- (50) Xie, C.; Chen, Y. S.; Li, Y.; Wang, X. X.; Song, C. S. *Appl Catal a-Gen* **2010**, *390*, 210.
- (51) Nomoto, T.; Miura, K.; Yagi, S.; Kutluk, G.; Sumida, H.; Soda, K.; Hashimoto, E.; Namatame, H.; Taniguchi, M. *Surf Sci* **2007**, *601*, 3784.
- (52) Yagi, S.; Nomoto, T.; Kutluk, G.; Sumida, H.; Namatame, H.; Taniguchi, M.; Soda, K. *Rev Adv Mater Sci* **2005**, *10*, 277.
- (53) Nomoto, T.; Sumi, O.; Yagi, S.; Soda, K.; Namatame, H.; Taniguchi, M. *Surf Interface Anal* **2008**, *40*, 391.

## Chapter 2

### **Density Functional Theory Study of Sulfur Tolerance of CO Adsorption and Dissociation on Rh-Ni Binary Metals**

This chapter is published as: Kyungtae Lee, Chunshan Song, Michael J. Janik. *Applied Catalysis A: General*, 389 (2010), 122-130

**ABSTRACT:** The effect of Ni addition to improve the sulfur tolerance of a Rh catalyst for CO dissociation was studied using density functional theory (DFT) methods. Adsorption and dissociation were considered over the (111) surfaces of binary  $\text{Rh}_1\text{Ni}_2$  and  $\text{Rh}_2\text{Ni}_1$  metals with comparison to pure Rh and Ni surfaces. Sulfur adsorption on the  $\text{Rh}_1\text{Ni}_2(111)$  surface is 0.21 eV more endothermic than on the Rh(111) surface, suggesting that a  $\text{Rh}_1\text{Ni}_2$  bimetallic catalyst has a higher sulfur tolerance than pure Rh catalysts due to a lower surface coverage of the sulfur poison. To compare catalytic activity in the presence of adsorbed sulfur, the CO dissociation rates over the binary and pure metals were calculated with 1/9 sulfur coverage. CO dissociation is fastest on the pure Rh surface under sulfur-free conditions, whereas among sulfur poisoned surfaces, the  $\text{Rh}_1\text{Ni}_2$  surface shows the fastest CO dissociation rate. The CO dissociation barrier on  $\text{Rh}_1\text{Ni}_2$  is destabilized less by a S coadsorbate than for the other metals. The addition of Ni atoms to a Rh catalyst improves the sulfur tolerance of the catalyst for CO dissociation by minimizing the repulsion between the adsorbed S atom and the CO dissociation transition state, as evidenced through a projected density of states analysis. The  $\text{Rh}_1\text{Ni}_2(221)$  stepped surface also shows a lower activation barrier and higher CO dissociation rate in the presence of sulfur than the Rh(221) stepped surface.

## 2.1 Introduction

Hydrocarbon reforming processes are used industrially to produce hydrogen gas, which may become an important alternative energy carrier.<sup>1</sup> In the reforming process for fuel cell applications, hydrogen is produced from natural gas, liquid hydrocarbons ( $C_mH_n$ ), or alcohols.<sup>2-4</sup> These fuels contain a ppm level of sulfur containing species, or a ppb level following a desulfurization process.<sup>5,6</sup> For reforming of most liquid hydrocarbon fuels, catalysts are continuously exposed to the sulfur compounds, which accumulate on the catalyst's surface due to strong sulfur surface adsorption.<sup>7,8</sup> Reforming catalysts lose their activity for converting liquid hydrocarbon fuels due to sulfur poisoning, which can further increase the formation of carbon deposits on the surface.<sup>9,10</sup> To overcome such deactivation, Strohm et al. introduced Rh-Ni catalysts with high sulfur tolerance for steam reforming of liquid hydrocarbon fuels.<sup>11</sup> The mechanism accounting for such an improvement is not clear, which motivates our study. The reforming process involves a complex reaction network at temperatures over 500 °C, making experimental elucidation of the elementary mechanistic impact of S adsorption over the binary metal catalysts difficult.

Density functional theory (DFT) methods allow us to analyze individual elementary reactions and examine their mechanistic impact within the overall reforming reaction. Herein, we use DFT methods to examine the sulfur tolerance of bimetallic Rh-Ni catalysts by analyzing CO adsorption and dissociation in the presence of sulfur. Carbon monoxide (CO) dissociation is an important step in determining activity and selectivity.<sup>12,13</sup> Carbon monoxide (CO) dissociation is also a critical step in other catalytic processes such as Fischer-Tropsch synthesis and methanation,<sup>14,15</sup> and our results provide insight into evaluating sulfur tolerance in these processes.

Sulfur compounds in hydrocarbon fuels are converted into hydrogen sulfide ( $H_2S$ ) during the reforming process, which dissociatively adsorbs leaving sulfur atoms on the catalyst surface.<sup>5</sup> Once sulfur

poisoning occurs on the catalyst surface, the catalyst loses its reforming activity and pyrolysis of the hydrocarbon fuel mainly occurs.<sup>16</sup> This pyrolysis leads to carbon deposits on the catalyst and prevents the catalyst from reforming the hydrocarbon fuel.<sup>10</sup> Sulfur tolerance may be enhanced in binary metal catalysts. Non-noble Ni catalysts have been mainly used in industry for low-cost reforming processes.<sup>17</sup> Noble metals such as Rh and Ru are expensive, but advantageous to minimizing carbon formation.<sup>11</sup> Recently, several studies have reported that Rh addition to Ni catalysts combines benefits of a low-cost process with high activity, high selectivity, and lower formation of carbon deposits.<sup>18-20</sup> In addition to the advantages mentioned above, Strohm et al. showed that the addition of Ni to a Rh reforming catalyst supported on  $\text{CeO}_2\text{-Al}_2\text{O}_3$  enhances sulfur tolerance with the highest performance of 2 wt% Rh-10 wt% Ni (Ni: Rh atomic ratio of 1:0.1).<sup>11</sup> TPR and XPS analysis indicated a close interaction between Rh and Ni, implying that Rh-Ni is present as a bimetallic form during the reforming process.

Interestingly, the methane selectivity during reforming over Rh and Ni-Rh catalysts declines in advance of the fuel conversion decrease, implying that methane formation is most sensitive to sulfur poisoning.<sup>11</sup> There are two possible routes for methane formation, hydrogenation of CO and cleavage of C-C bonds followed by hydrogenation of  $\text{C}_1$  ( $\text{CH}_3$ ) fragments. Whereas the cleavage of hydrocarbons also produces other short-chain hydrocarbons, the hydrogenation of CO leads to only methane as the final product. The rate-determining step of hydrogenation of CO is the CO dissociation step,<sup>12</sup> therefore we initially examine the sulfur tolerance mechanism by analyzing CO adsorption and dissociation on Rh-Ni surfaces in the presence of adsorbed sulfur.

The impact of S presence on CO adsorption has been previously considered using DFT methods. Zhang et al. reported the influence of a sulfur atom on the adsorption energy of CO on the Rh(111) surface.<sup>21</sup> The CO adsorption energy is destabilized by 0.2 eV for a S coverage of 1/4 monolayer (ML) and by 0.05 ~ 0.1 eV for 1/9 ML. The effect of S on the CO dissociation step was examined over the Fe(100) surface.<sup>22</sup> This DFT study found that the presence of S increases the activation barrier of CO

dissociation by 0.15 eV and makes the reaction energy endothermic, indicating that an adsorbed S atom slows the CO dissociation step.

The adsorption and dissociation of CO on a sulfur-free surface has been extensively investigated using DFT methods. On Rh(111), CO initially adsorbs on top of a Rh atom and then C and O atoms dissociate into hollow sites with an intrinsic activation energy based on the energy of CO gas of 1.2 to 1.3 eV.<sup>23-25</sup> On Ni(111), CO initially adsorbs at a fcc hollow site and dissociation moves the O atom into another hollow site with an intrinsic activation energy of 1.1 to 1.4 eV.<sup>15,26,27</sup> The activation energy values of CO dissociation are similar on Rh and Ni surfaces. However, Stroppa et al. revealed that Ni decoration of a Rh stepped surface lowers the activation barrier of CO dissociation by 0.09 eV under a sulfur-free condition.<sup>28</sup> This study did not consider the impact of S coadsorption, however they suggest that Rh-Ni binary surfaces may show lower CO dissociation barriers than the pure metal surfaces. Previous studies also have clearly demonstrated the importance of stepped surfaces in catalyzing CO dissociation. The activation barrier for CO dissociation on the Rh(211) stepped surface is 0.87 eV lower than on the flat (111) surface.<sup>24,25</sup> Therefore, we analyze the effect of binary Rh-Ni on sulfur tolerance for CO dissociation by varying the ratio of Rh to Ni on both the flat (111) and stepped (221) surfaces.

We examine CO adsorption and dissociation on Rh-Ni (111) and (221) surfaces. The adsorption of S on these surfaces and its impact on CO adsorption and dissociation is considered. Comparison is made with the pure Ni and Rh surfaces. Our results show that Rh<sub>1</sub>Ni<sub>2</sub> surfaces maintain the greatest activity for CO dissociation in the presence of sulfur.

## 2.2 Methods

Calculations were carried out using the Vienna Ab-initio Simulation Program (VASP), an ab initio total-energy and molecular dynamics program developed at the Institute for Material Physics at the

University of Vienna.<sup>29-31</sup> The Perdew-Wang (PW91) version of the generalized gradient approximation (GGA) is used for exchange and correlation energies.<sup>32,33</sup> The electron-ion interactions are described by the projector augmented wave (PAW) method by Blöchl.<sup>34</sup> The cut-off energy of the plane-waves basis set used to represent valence electrons was 400 eV. The reciprocal space has been sampled with a  $(5 \times 5 \times 1)$  gamma centered grid for  $3 \times 3$  metal surfaces, a  $(7 \times 7 \times 1)$  grid for  $2 \times 2$  metal surfaces, and the gamma point only for isolated molecules. The carbon monoxide molecule was optimized in a  $10 \times 10 \times 10$  Å cubic unit cell. Spin-polarized calculations were applied for pure Ni structures, Rh-Ni binary structures and the isolated S atom. The isolated S atom had two unpaired electrons. Structural optimization was stopped when the forces on all atoms were minimized to less than  $0.05 \text{ eV } \text{\AA}^{-1}$ .

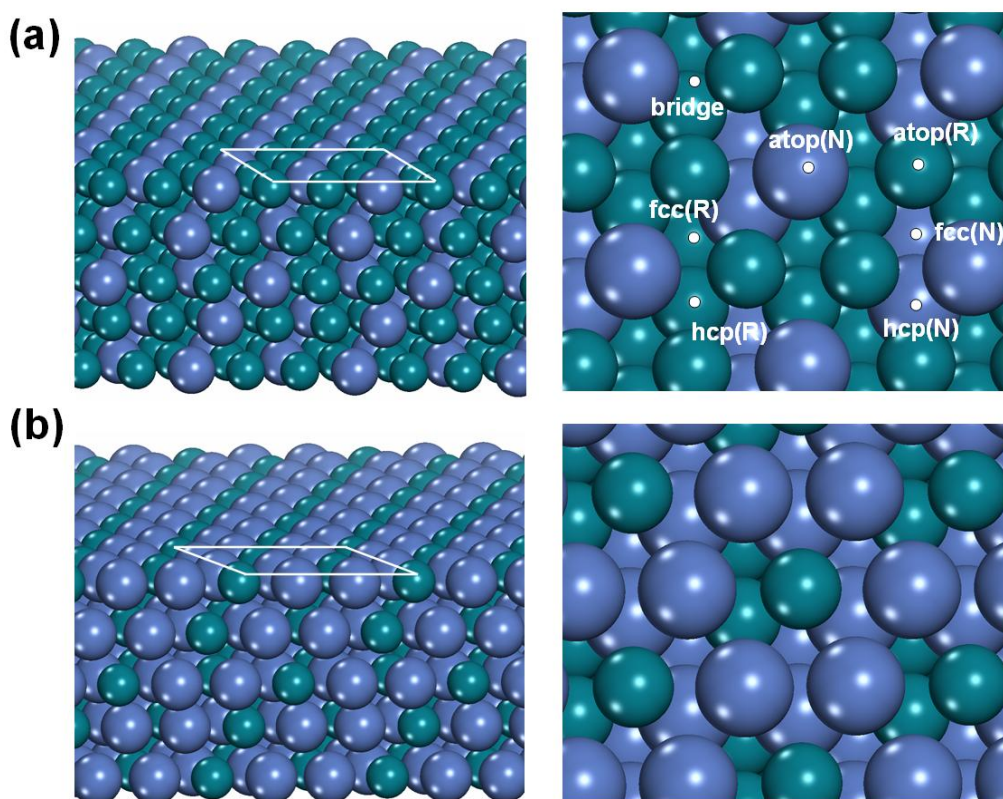


Figure 2-1. Perspective view (left) and top view (right) of the Rh-Ni (111) surfaces (dark small sphere: Rh, light large sphere: Ni); (a)  $\text{Rh}_2\text{Ni}_1$ , (b)  $\text{Rh}_1\text{Ni}_2$ . There are six possible adsorption sites for an adsorbate, as shown in (a): N and R in parenthesis indicate a site located over a Ni metal atom and a Rh metal atom, respectively.

The optimized lattice parameters for Rh and Ni are 3.800 Å (3.803 Å experimentally,<sup>35</sup> 0.08 % difference) and 3.520 Å (3.524 Å experimentally,<sup>35</sup> 0.11%), respectively. The Rh-Ni binary metal model evenly distributes Ni and Rh atoms in the structure shown in Figure 2-1. The optimized lattice parameters are 3.758 Å for Rh<sub>2</sub>Ni<sub>1</sub> and 3.658 Å for Rh<sub>1</sub>Ni<sub>2</sub>. DFT calculations indicate that the formation of these two bimetallic phases from the constituent pure metals is thermodynamically favorable over 100 °C.<sup>36</sup> To model flat surfaces, the (111) surface was used with a five metal layer slab (top three layers relaxed). Each slab was separated by 10 Å of vacuum normal to the surface. For the stepped surfaces of Rh and Rh<sub>1</sub>Ni<sub>2</sub>, we used the (221) surface which has a similar geometry with the (553) surface examined by others,<sup>28,37</sup> the difference being that (221) has one less row in the (111) terrace than the (553) surface. The Rh<sub>1</sub>Ni<sub>2</sub> stepped surface was made by cleaving the Rh<sub>1</sub>Ni<sub>2</sub> bulk metal. The stepped surfaces consist of a total of six metal layers with the top three layers relaxed and periodic slab repetitions are separated by 10 Å of vacuum.

The climbing image nudged elastic band (CI-NEB) method was used to locate the transition states and calculate the activation barriers for CO dissociation on flat surfaces. To apply the CI-NEB, the interpolated four images between the initial and final states were optimized along the reaction coordinate. The image with a maximum energy value and an absolute tangential force below 0.05 eV Å<sup>-1</sup> is the transition state. The transition states on the Rh and Rh<sub>1</sub>Ni<sub>2</sub> stepped surfaces were first approximated with the CI-NEB method based on the previously reported configurations of CO dissociation on Rh stepped surface<sup>24,28</sup> and the isolated highest energy image was used as input to a dimer transition state search calculation<sup>38</sup>. All transition states were confirmed to have a single imaginary vibrational frequency.

## 2.3 Results and Discussion

### 2.3.1 Adsorption energy of S and CO on (111) surfaces of Rh, Ni pure and binary metals

The configurations for CO dissociation on pure and binary metal surfaces can be constructed based on the preferred adsorption sites for S and CO on those surfaces. The various high-symmetry adsorption sites on the binary metal surface that were considered for adsorption are illustrated in Figure 2-1a. Atop, hollow (hcp and fcc), and bridge sites were considered on the single metal (111) surface. The adsorption energies of CO and S on each site are listed in Table 2-1 along with bond lengths of C-O, C-M, and S-M. The adsorption of CO on both Rh and Ni is stronger at the hcp and fcc hollow sites than the atop and bridge sites. Strong adsorption at the hollow site includes electron back-donation to the C-O antibonding orbital, lengthening the C-O distance from 1.14 Å in gas phase to 1.19 Å on the surface. The energy differences between the hollow sites and the other sites are greater for S than for CO adsorption. For example, on Rh(111), S atoms prefer hollow sites by ~0.5 eV whereas the preference for CO is 0.05~0.1 eV. This suggests that with S coadsorbed, CO dissociation configurations on pure metals should retain S at its preferred adsorption site.

Hollow sites are assumed to be preferred for CO and S adsorption to the  $\text{Rh}_2\text{Ni}_1$  and  $\text{Rh}_1\text{Ni}_2$  bimetallic surfaces. We considered four types of hollow sites, indicated as hcp(R), fcc(R), hcp(N), and fcc(N). The adsorption energies and distances between the atoms on the binary metals are also listed in Table 2-1. Based on the preferred adsorption sites and strong S preference, we placed the S atom in the fcc(N) site on both  $\text{Rh}_2\text{Ni}_1$  and  $\text{Rh}_1\text{Ni}_2$  surfaces while examining CO coadsorption sites.

The differences in S adsorption energies among Ni, Rh, and Ni-Rh bimetallics provide insight into the S tolerance of the bimetallic catalysts. The adsorption energy of S at the preferred fcc site on pure Ni(111) surface is 0.31 eV more endothermic than that on the pure Rh(111) surface, indicating that the



Table 2-1. Adsorption energies ( $\Delta E_{ads}$ , eV) and bond distances ( $\text{\AA}$ ) for S and CO adsorbed to high symmetry sites on Ni, Rh monometallic and Ni-Rh bimetallic (111) surfaces.

pure metals	Rh					Ni				
	CO			S		CO			S	
	$\Delta E_{ads}$	$d_{C-O}$	$d_{C-M}^a$	$\Delta E_{ads}$	$d_{S-M}^a$	$\Delta E_{ads}$	$d_{C-O}$	$d_{C-M}^a$	$\Delta E_{ads}$	$d_{S-M}^a$
atop	-1.90	1.16	1.84	-3.55	2.13	-1.59	1.16	1.74	-3.60	2.01
hcp	-2.01	1.20	2.09	-5.47	2.26	-1.92	1.19	1.95	-5.09	2.14
fcc	-1.96	1.19	2.10	-5.48	2.27	-1.91	1.19	1.95	-5.17	2.14
bridge	-1.91	1.19	2.02	-5.00	2.22	-1.80	1.19	1.88	-4.91	2.10
alloy metals	Rh <sub>2</sub> Ni <sub>1</sub>					Rh <sub>1</sub> Ni <sub>2</sub>				
	CO			S		CO			S	
	$\Delta E_{ads}$	$d_{C-O}$	$d_{C-M}^b$	$\Delta E_{ads}$	$d_{S-M}^b$	$\Delta E_{ads}$	$d_{C-O}$	$d_{C-M}^b$	$\Delta E_{ads}$	$d_{S-M}^b$
hcp(R)	-1.99	1.20	2.07 (2.00)	-5.36	2.26 (2.15)	-1.92	1.19	2.06 (1.97)	-5.15	2.29 (2.14)
fcc(R)	-1.94	1.19	2.07 (2.04)	-5.35	2.26 (2.14)	-1.91	1.19	2.06 (1.98)	-5.21	2.28 (2.14)
hcp(N)	-1.93	1.20	2.08 (1.97)	-5.37	2.26 (2.14)	-1.93	1.19	2.07 (1.96)	-5.22	2.27 (2.13)
fcc(N)	-1.98	1.19	2.07 (2.02)	-5.45	2.27 (2.15)	-1.92	1.19	2.05 (1.98)	-5.27	2.28 (2.14)

<sup>a</sup>  $d_{C-M}$  and  $d_{S-M}$  are the distances of surface metal atom from C atom and S atom, respectively. Hollow sites are represented with the average value of distances from three metal atoms to C or S atom.

<sup>b</sup> Since each hollow site is surrounded by both Rh and Ni metal atoms, the first value is an average distance of S or C to Rh metal atoms and the value in parenthesis is an average distance to Ni atoms.

equilibrium adsorption S coverage will be less on Ni than Rh catalysts. The Rh<sub>1</sub>Ni<sub>2</sub> metal containing a high ratio of Ni also has a 0.21 eV weaker adsorption energy of S at the preferred fcc(N) site than at the fcc site of pure Rh, suggesting that the coverage of S on Rh-Ni metals will be less than on pure Rh. However, the Rh<sub>2</sub>Ni<sub>1</sub> metal containing a high ratio of Rh has a similar adsorption energy of S to that on pure Rh. Experimental deactivation studies of jet fuel reforming showed that the sulfur tolerance of a 2 wt% Rh catalyst was improved by increasing the amount of Ni up to 10 wt% (Ni:Rh atomic ratio of 1:0.1).<sup>11</sup> We conclude that one reason a Rh-Ni binary metal has a high sulfur tolerance compared to pure Rh is due to the weaker S binding on Rh-Ni compared to pure Rh.

### 2.3.2 Influence of sulfur coadsorption on CO, C, and O adsorption energies to Rh(111)

Sulfur has a short-range influence on CO molecules adsorbed to the catalyst surface.<sup>21,22</sup> Thus, we need to identify a feasible sulfur coverage at which CO may adsorb and dissociate in the presence of adsorbed sulfur. We considered the effect of Rh(111) S coverage on CO adsorption as well as on the dissociation products of adsorbed C and O atoms. Figure 2-2 illustrates the coadsorption structures considered, which are equivalent to those used by Zhang et al.<sup>21</sup> The adsorption energies at the initial and final states of CO dissociation are summarized in Table 2-2. The trends of adsorption energies at the initial state are consistent with the result of Zhang et al., but there are absolute differences in adsorption energies. These small differences are accounted for by method variations; Zhang et al. used three layer slabs with 2x2 and 3x3 surface cells and 2, 8 k-points for structure optimization, whereas we used five layers with the top three layers relaxed and 13, 25 k-points for 2x2 and 3x3 cells.

In the presence of sulfur, adsorption energies at the initial and final states are destabilized. The extent of destabilization is described by the difference in adsorption energy with and without S present ( $\Delta E_{\text{ads}}^{\text{w/S}} - \Delta E_{\text{ads}}^{\text{w/o S}}$ ). While the extent of destabilization at the final state on the 1/9 S coverage is 0.29 eV, the extent on the 1/4 S coverage is as high as 1.29 eV. This implies that CO dissociation will not occur to a significant extent with 1/4 ML S coverage. The change of the dissociation reaction energies ( $\Delta E_{\text{diss}}$ ) in the presence of S atoms on surface is given by  $(\Delta E_{\text{ads}}^{\text{w/S}} - \Delta E_{\text{ads}}^{\text{w/o S}}$  at the final state)  $- (\Delta E_{\text{ads}}^{\text{w/S}} - \Delta E_{\text{ads}}^{\text{w/o S}}$  at the initial state). The change of  $\Delta E_{\text{diss}}$  due to the presence of S coadsorbed is 0.86 eV for the 1/4 ML S coverage and 0.19 eV for the 1/9 ML S coverage. Therefore, the high endothermic dissociation energy and extremely unstable condition for the dissociated C and O atoms on the 1/4 ML S coverage lead us to exclude the 1/4 S coverage and apply the 1/9 S coverage to modeling CO dissociation in the presence of coadsorbed sulfur.

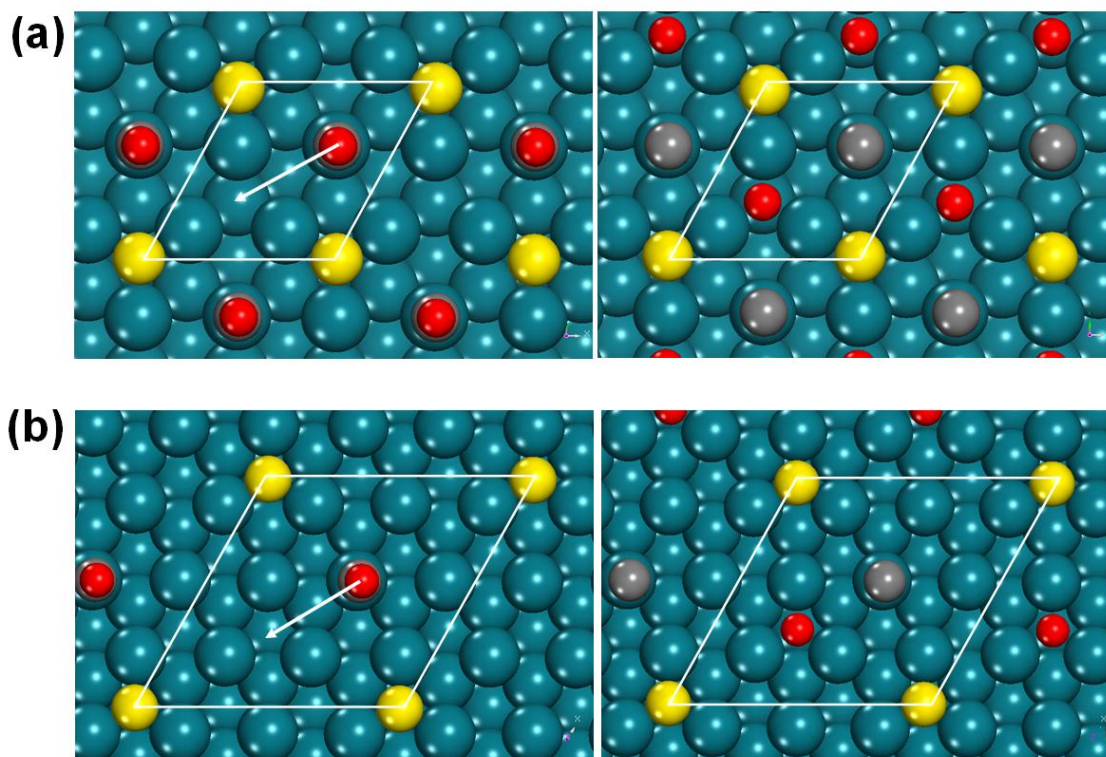


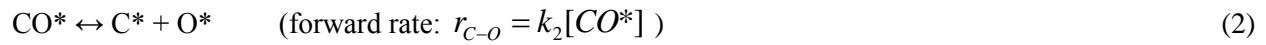
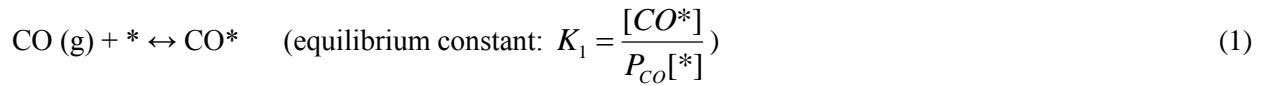
Figure 2-2. Adsorption of a CO molecule (left) and dissociated C and O (right) in (a) 1/4 ML S coverage and (b) 1/9 ML S coverage on the Rh (111) surface. S atoms are represented with light color, C atoms with grey color, and O atoms with dark color. Arrows indicate the movement of O atom during CO dissociation.

Table 2-2. Adsorption energies of CO and C + O on the Rh (111) surface in the presence of S. Adsorption energies calculated by Zhang et al. are shown in parenthesis <sup>21</sup>. The reference states for the calculation of  $\Delta E_{ads}^{w/o S}$  and  $\Delta E_{ads}^{w/S}$  use the energy of an isolated CO molecule for the initial state and the energies of isolated C and O atoms for the final state.

	CO (initial state)		C + O (final state)	
	1/4 ML	1/9 ML	1/4 ML	1/9 ML
$\Delta E_{ads}^{w/o S}$ (eV)	-1.91 (-1.80)	-1.90 (-1.88)	-10.29	-10.45
$\Delta E_{ads}^{w/S}$ (eV)	-1.48 (-1.60)	-1.79 (-1.83)	-9.00	-10.16
$\Delta E_{ads}^{w/S} - \Delta E_{ads}^{w/o S}$ (eV)	0.43	0.10	1.29	0.29

### 2.3.3 Expression for the apparent CO dissociation rate used to compare among metals

The extent of sulfur tolerance for CO dissociation can be compared across surface compositions by analyzing variations of the CO dissociation rate. Carbon monoxide dissociation occurs through the following two steps,



$P_{\text{CO}}$  is the partial pressure of CO gas,  $(\text{CO}^*)$  is the concentration of adsorbed CO molecules, and  $k_2$  is the rate constant of CO dissociation. For simplicity, we assume that the CO dissociation step is irreversible and examine the forward CO dissociation rate. Using the  $K_1$  equation, the CO dissociation rate in Eq. (2) is expressed as

$$r_{\text{C-O}} = k_2 K_1 P_{\text{CO}}[*] \quad (3)$$

The rate constant ( $k_2$ ) and equilibrium constant ( $K_1$ ) are related to thermodynamic parameters such as reaction Gibbs energy and entropy as described by the following equations.

$$K_1 = \exp(-\Delta G_1 / RT) = \exp\{-(\Delta H_1 - T\Delta S_1) / RT\} \quad (4)$$

$$k_2 = A \exp(-\varepsilon_{\text{act},2} / RT) \quad (5)$$

where  $\Delta G_1$ ,  $\Delta H_1$ , and  $\Delta S_1$  are the changes of Gibbs energy, enthalpy, and entropy of CO adsorption in Eq. (1),  $A$  is a pre-exponential factor, and  $\varepsilon_{act,2}$  is the activation energy of CO dissociation step in Eq. (2). From these relationships, Eq (3) is written as

$$\begin{aligned} r_{C-O} &= A \exp(-\varepsilon_{act,2} / RT) \exp(-\Delta H_1 / RT) \exp(\Delta S_1 / R) P_{CO}[*] \\ &= A' \exp\{-(\Delta H_1 + \varepsilon_{act,2}) / RT\} P_{CO}[*] \end{aligned} \quad (6)$$

where  $A'$  represents  $A \exp(\Delta S_1 / R)$  in which  $\Delta S_1$  is regarded as a constant because the entropy change of CO adsorption is not meaningfully dependent on the identity of the metal substrate. We also assume negligible metal to metal difference in pre-exponential factor,  $A$ , allowing us to consider  $A'$  as a metal independent constant. The final rate equation used replaces the DFT energy difference ( $\Delta E_1$ ) for  $\Delta H_1$  and presumes low sulfur coverage of CO, C, O such that (\*) may also be considered metal independent:

$$r_{C-O}' = A' \exp\{-(\Delta E_1 + \varepsilon_{act,2}) / RT\} P_{CO} \quad (7)$$

where  $r_{C-O}' = r_{C-O} / (*)$

Using Eq. (7), the relative rate equation for metal substrate I and II is expressed as

$$\frac{r_{C-O}'(I)}{r_{C-O}'(II)} = \frac{\exp\{-(\Delta E_1(I) + \varepsilon_{act,2}(I)) / RT\}}{\exp\{-(\Delta E_1(II) + \varepsilon_{act,2}(II)) / RT\}} \quad (8)$$

### 2.3.4 CO dissociation configurations

The configurations for CO dissociation on each metal were constructed based on the stable adsorption sites of CO and S in Table 2-1 and the preferred dissociation path for CO dissociation reported by Morikawa et al.<sup>26</sup> According to the preferred dissociation path, the O atom moves in the  $(\bar{1}10)$  direction and finally arrives at another hollow site via the bridge site as shown in Figure 2-3. For each metal, we considered an additional configuration, configuration B, by placing the CO molecule at a hollow site close to the S atom in order to observe the results with stronger influence of S on adsorbed CO. As we have to consider both the preferred sites and preferred path, we used the second or third preferred adsorption sites for CO due to its minor site-dependence in order to place the S atom in the most preferred adsorption site and apply the identical CO dissociation path for each metal. We used the fcc hollow site for CO adsorption on Ni and the fcc(N) hollow site for CO adsorption on Rh<sub>1</sub>Ni<sub>2</sub>, both of which have a difference of 0.01 eV in energy from the most stable adsorption site. In the case of Rh<sub>2</sub>Ni<sub>1</sub>, we used the fcc(N) hollow site for CO adsorption in configuration A and the fcc(R) hollow site for CO adsorption in configuration B with differences of 0.01 and 0.05 eV from the most stable site. The CO dissociation configurations under the sulfur-free condition were equivalent to the CO adsorption configurations used under the sulfur-poisoned condition. The initial, transition, and final states on each metal are illustrated in Figure S1.

### 2.3.5 Energetics of CO dissociation

The activation energy ( $\varepsilon_{\text{act},2}$ ) and adsorption energy of CO ( $\Delta E_1$ ) were obtained using the models shown in Figure 2-3, which enable us to calculate the CO dissociation rates relative to sulfur-free Rh(111)

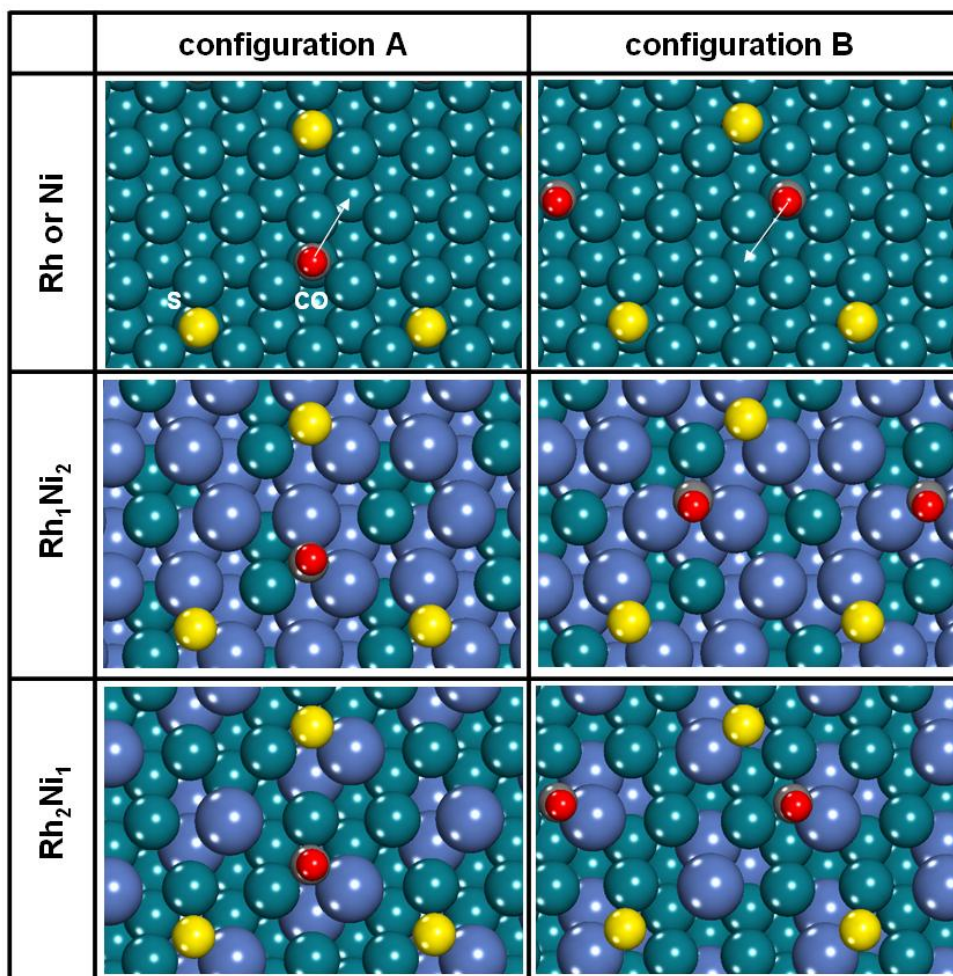


Figure 2-3. CO dissociation configurations on each metal surface. In configuration B, S atoms are located to have a closer interaction with adsorbed CO molecules than configuration A. Arrows indicate the path taken by the O atom during dissociation with the point residing on the final O adsorption site. (Rh and Ni: dark and light spheres in the substrate, respectively. C, O, S: grey, dark, and light spheres in the adsorbate layer, respectively.)

using Eq. (8), as summarized in Table 2-3. Figure 2-4 plots the activation barrier for CO dissociation versus the adsorption energy of CO, the two values that collectively determine the CO dissociation rate according to Eq. (8). A strong correlation between dissociation barrier and adsorption energy is not observed in Figure 2-4. The cause of a decreased CO dissociation rate in the presence of sulfur varies across surfaces and configurations, including weaker CO adsorption (ex. Ni (conf. B)), increased

dissociation barrier (ex.  $\text{Rh}_2\text{Ni}_1$  (conf. A)), or both weaker CO adsorption and an increased barrier (ex.  $\text{Rh}_2\text{Ni}_1$  (conf. B)). As a stronger adsorption energy of CO and a lower activation barrier lead to a higher CO dissociation rate, the bottom left area in Figure 2-4 represents the catalysts with a highest CO dissociation rate. The pure and binary metals under sulfur-free conditions appear in this area. Among them, the pure Rh surface has the highest dissociation rate under sulfur-free conditions. This is consistent with reactivity studies which showed that a fuel conversion of 98 % was maintained on the pure Rh catalyst for 83 hours under a sulfur-free condition.<sup>11</sup>

Table 2-3. Relative CO dissociation rate, activation energy of CO dissociation and adsorption energies of CO on each metal surface. CO dissociation rates were calculated at the reaction temperature of 773.15 K.

surface	metal	relative rate	adsorption energy of CO (eV)	activation energy of CO (eV)
clean surface	Rh	1	-2.01	2.97
	$\text{Rh}_1\text{Ni}_2$	$8.09 \times 10^{-1}$	-1.92	2.90
	Ni	$5.93 \times 10^{-1}$	-1.91	2.91
	$\text{Rh}_2\text{Ni}_1$	$2.95 \times 10^{-1}$	-1.98	3.02
sulfur poisoned surface	$\text{Rh}_1\text{Ni}_2$ (conf. A)	$4.96 \times 10^{-2}$	-1.80	2.96
	Rh (conf. A)	$2.16 \times 10^{-2}$	-1.94	3.16
	$\text{Rh}_2\text{Ni}_1$ (conf. A)	$1.94 \times 10^{-2}$	-1.97	3.20
	$\text{Rh}_1\text{Ni}_2$ (conf. B)	$1.10 \times 10^{-2}$	-1.66	2.92
	Ni (conf. A)	$7.18 \times 10^{-3}$	-1.93	3.22
	Ni (conf. B)	$6.72 \times 10^{-3}$	-1.62	2.91
	Rh (conf. B)	$2.90 \times 10^{-3}$	-1.72	3.07
	$\text{Rh}_2\text{Ni}_1$ (conf. B)	$4.36 \times 10^{-4}$	-1.69	3.17



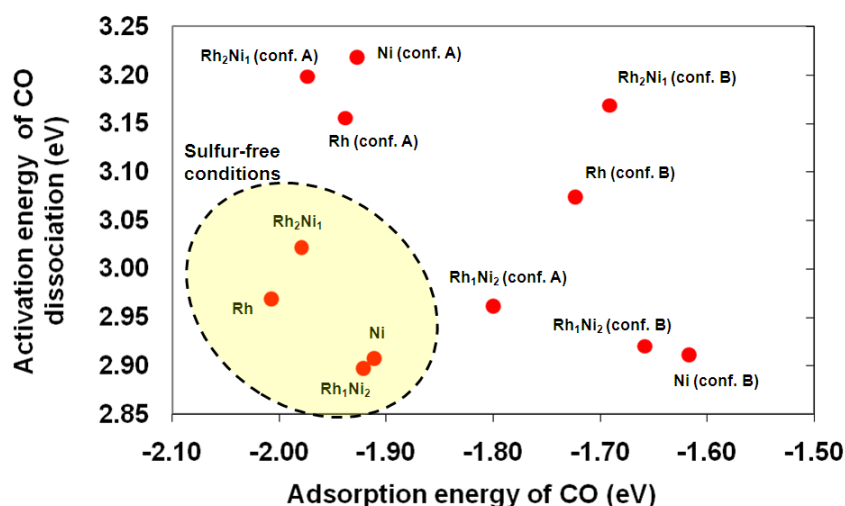


Figure 2-4. Plot of the CO dissociation activation energy versus the CO adsorption energy for the various Ni, Rh, and Ni-Rh surfaces considered. The dotted circle line indicates the catalysts under sulfur-free conditions and the other points outside the dotted circle are for the catalysts in the presence of sulfur.

The most notable result in Table 2-3 is that among all the pure and binary surfaces, the Rh<sub>1</sub>Ni<sub>2</sub> metal exhibits the best performance in the presence of sulfur for both configuration A and B, consistent with the experimental result that addition of Ni improves sulfur tolerance of Rh catalysts.<sup>11</sup> For configuration A, all metals experience an increase of activation barrier by 0.06 ~ 0.31 eV due to sulfur poisoning. Rh<sub>1</sub>Ni<sub>2</sub> is least affected by the presence of sulfur, implying that the transition state is not as destabilized by sulfur poisoning. For configuration B with S near to the CO adsorbate, the activation barriers are decreased due to the relatively larger S destabilization of the initial states compared to that of the transition states. In configuration B, the Rh<sub>1</sub>Ni<sub>2</sub> metal also shows a relatively low activation barrier compared to other metals, leading to the catalyst with the highest CO dissociation rate in configuration B. Whereas the Rh<sub>1</sub>Ni<sub>2</sub> surface has the highest sulfur tolerance in both configuration A and B, the Rh<sub>2</sub>Ni<sub>1</sub> surface, containing a smaller ratio of Ni, is not sulfur tolerant. This is also consistent with experimental results, which suggested that a high sulfur tolerance is accomplished by adding a 9:1 Ni to Rh atomic ratio at 33 ppm sulfur level.<sup>11</sup> Figure 2-4 illustrates that the Rh<sub>2</sub>Ni<sub>1</sub> metal containing a small ratio of Ni is not able to prevent a significant change in the activation barrier for CO dissociation by sulfur poisoning.

### 2.3.6 Projected Density of State (PDOS) analysis

The difference in CO dissociation energetics between the pure Rh and bimetallic Rh<sub>1</sub>Ni<sub>2</sub> surfaces was analyzed using the projected density of states (PDOS) of 2p orbitals of C and O atoms. An electronic explanation of the reduced S poisoning observed for the Rh<sub>1</sub>Ni<sub>2</sub> surface is sought as a simple geometric argument does not explain this observation. The adsorbed S atom shows a lessened effect on the CO dissociation rate on Rh<sub>1</sub>Ni<sub>2</sub> surfaces with comparison to Rh despite the adsorbed S atom being slightly closer to the CO and C+O adsorbates in the binary metal system. Figure 2-5 (a) and (c) show the initial state and transition state PDOS's of the O 2p orbital (left figures) on each metal surface with and without a coadsorbed S atom. The shift of the PDOS graph between sulfur free and sulfur coadsorbed conditions on Rh is more pronounced than on Rh<sub>1</sub>Ni<sub>2</sub>, especially in the initial state. The peak shift on Rh is due to peak broadening which occurs when the interaction between adsorbates increases.<sup>39,40</sup> Thus, the PDOS data indicates that the interaction between CO and S on Rh<sub>1</sub>Ni<sub>2</sub> is weaker than that on Rh, in agreement with the greater sulfur tolerance of Rh<sub>1</sub>Ni<sub>2</sub>. At the transition state, it is not easy to perceive the difference in the PDOS between Rh and Rh<sub>1</sub>Ni<sub>2</sub> after S adsorption because the PDOS is more disperse than in initial state.

For a further explanation of the PDOS shift in the initial states, we visualized the partial charge density associated with specific peaks in the C and O PDOS. The partial charge densities on pure Rh with S are visualized in Figure 2-6 for states at energies of -11.6 and -11.8 eV, where major peak shifts of initial states occur (Figure 2-5a). According to Figure 2-6, the peak at -11.6 eV, a reduced peak in the presence of S, does not exhibit any interaction between CO and S. The peak at -11.8 eV, a peak strengthened in the presence of S, shows the interaction of S and CO that makes the adsorbed CO molecule unstable. Although there is an increase at -11.8 eV and decrease at -11.6 eV, the net effect is to increase the energy as given in next paragraph. The partial charge density on Rh<sub>1</sub>Ni<sub>2</sub> is not shown here, as

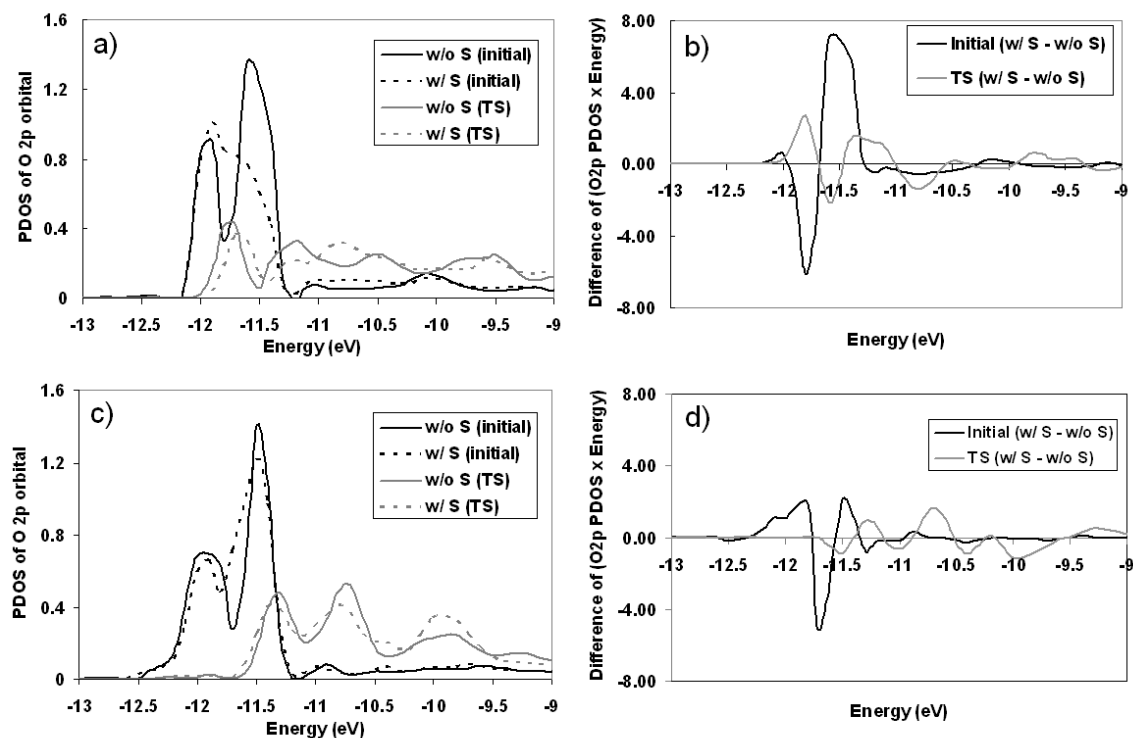


Figure 2-5. Projected density of states of the O 2p orbital in the initial (CO adsorbed) and transition (CO dissociation) states on a) the Rh and c) Rh<sub>1</sub>Ni<sub>2</sub> surfaces (solid line: with sulfur, dotted line: without sulfur). The energy-weighted differences of (PDOS of O 2p × energy) values between the presence and absence of sulfur on b) the Rh and d) Rh<sub>1</sub>Ni<sub>2</sub> surfaces are plotted versus energy relative to vacuum.

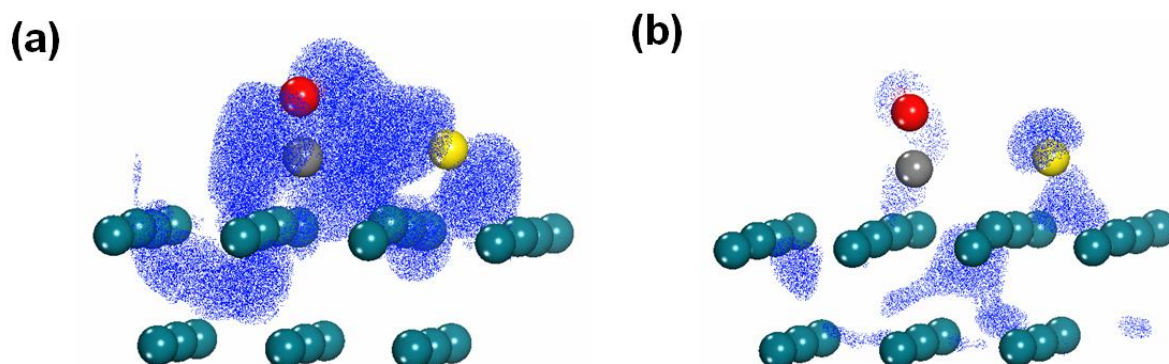


Figure 2-6. Partial charge density images on pure Rh at (a) -11.8 eV and (b) -11.6 eV in the presence of S. The values above  $1.0 \times 10^{-5}$  in charge density were visualized for these images. (Rh is dark spheres in the substrate. C, O, and S: grey, dark, and light spheres in the adsorbates, respectively.)

we could not find any direct interaction between S and CO. Therefore, the high sulfur tolerance on  $\text{Rh}_1\text{Ni}_2$  is explained by the fact that the influence of sulfur on the adsorbed CO is limited on the  $\text{Rh}_1\text{Ni}_2$  surface.

We measured the electronic energy associated with occupation of these states by the integral energy ( $E_{\text{int}}$ ) of the O projected orbital described as the following equation

$$E_{\text{int}} = \int_{-\infty}^{\epsilon_F} (\epsilon \times \text{PDOS}) d\epsilon \quad (9)$$

where  $\epsilon_F$  is the Fermi energy of a system. Comparison of sulfur induced shifts in this value between surfaces can be used to track the energetic impact of S poisoning. The energy weighted PDOS differences between with and without S are depicted in Figure 2-5 (b) and (d) and the  $E_{\text{int}}$  values are listed in Table 2-4. The C 2p orbital could equally have been used for this analysis and provides the same qualitative results as the major shift affected by S binding is the C-O  $\pi$  or  $\pi^*$  orbital. Most integral values in Table 2-4 are positive, indicating that S coadsorption destabilizes occupation of the O 2p orbital states. The integral values for the  $\text{Rh}_1\text{Ni}_2$  surface are smaller than for the pure Rh surface, implying that the C and O orbital energies become relatively less unstable on  $\text{Rh}_1\text{Ni}_2$  following S adsorption than on Rh. This trend is more conspicuous in the transition state. The integral values in C 2p orbital on  $\text{Rh}_1\text{Ni}_2$  is negative, and the sum of two integrals in C 2p and O 2p is equal to zero. This trend shows qualitative agreement with

Table 2-4. Differences in the integrated energy-weighted PDOS ( $E_{\text{int}}$ , equation (9)) between the sulfur free and sulfur coadsorbed conditions on Rh and  $\text{Rh}_1\text{Ni}_2$ .

surface (projected orbital)	CO adsorbed (eV)	CO dissociation TS (eV)	dissociation product (eV)
Rh(111) (C 2p)	0.77	0.25	0.26
Rh(111) (O 2p)	0.61	0.41	0.02
$\text{Rh}_1\text{Ni}_2(111)$ (C 2p)	0.11	-0.08	0.37
$\text{Rh}_1\text{Ni}_2(111)$ (O 2p)	0.36	0.08	0.04

the minimal changes in activation energy on  $\text{Rh}_1\text{Ni}_2$  after S adsorption in Figure 2-4. However, quantitative comparisons between these energy changes and the calculated CO dissociation energetics are not possible because the PDOS magnitude is affected by the choice of atom radii used in projecting the plane-wave states onto atomic orbitals.

### 2.3.7 CO dissociation on stepped surfaces

Carbon monoxide (CO) dissociation was also considered on stepped surfaces, as step sites are known to be more active for this reaction than flat surfaces.<sup>41</sup> The Rh and  $\text{Rh}_1\text{Ni}_2$  (221) surfaces were used to examine the impact of S coadsorption on CO dissociation energetics. The isolated transition state structures on the (221) surfaces are similar to those previously reported over the Rh(211) or (553) surfaces.<sup>24,28</sup> The adsorption site of S was chosen to give a similar distance between S and C atoms as configuration B of Figure 2-3, with S placed at the step-bottom site where the adsorption energy is most exothermic. For the  $\text{Rh}_1\text{Ni}_2$  surface, the adsorption energy difference of CO on each atop site is more pronounced than that of S on each step-bottom fcc site, thus we modeled the CO dissociation configuration based on the most preferred site for CO. For this reason, the adsorption energy of S at the most preferred site on the  $\text{Rh}_1\text{Ni}_2$  stepped surface is given separately in Table 2-5. The initial and transition states of CO dissociation on the (221) surfaces are displayed in Figure 2-7 and Figure S2 (supporting information). The calculated energetics and relative dissociation rates are listed in Table 2-5.

One of the advantages of the  $\text{Rh}_1\text{Ni}_2(111)$  surface is less exothermic adsorption of sulfur than on the other Rh-containing (111) surfaces. This is not apparent for the (221) stepped surfaces. The Rh stepped surface has a similar S adsorption energy to its flat surface whereas  $\text{Rh}_1\text{Ni}_2(221)$  has more exothermic S adsorption energy at the most preferred site for S (Table 2-5), leading to similar adsorption

Table 2-5. Adsorption energies of S and CO, activation energies of CO dissociation, and CO dissociation rates on Rh and Rh<sub>1</sub>Ni<sub>2</sub> (221) stepped surfaces. CO dissociation rates were calculated at the reaction temperature of 773.15 K, and are given as relative values to the CO dissociation rate on the Rh(111) surface .

metal surface	adsorption energy (eV)			activation energy (eV)		relative dissociation rate	
	S	CO (w/o S)	CO (w/ S)	w/o S	w/ S	w/o S	w/ S
Rh(111)	-5.48	-2.01	-1.72	2.97	3.07	1	$2.90 \times 10^{-3}$
Rh(221)	-5.47	-1.92	-1.92	2.11	2.34	$1.22 \times 10^5$	$3.05 \times 10^3$
Rh <sub>1</sub> Ni <sub>2</sub> (111)	-5.27	-1.92	-1.66	2.90	2.92	$8.09 \times 10^{-1}$	$1.10 \times 10^{-2}$
Rh <sub>1</sub> Ni <sub>2</sub> (221)	-5.12 (-5.52) <sup>a</sup>	-1.94	-1.96	2.08	2.27	$2.52 \times 10^5$	$1.67 \times 10^4$

*a* - The first value of S adsorption energy on the Rh<sub>1</sub>Ni<sub>2</sub>(221) surface is calculated at the site that was used for the CO dissociation calculation and the value in parenthesis is calculated at the most preferred site (the other step bottom fcc site) for S.

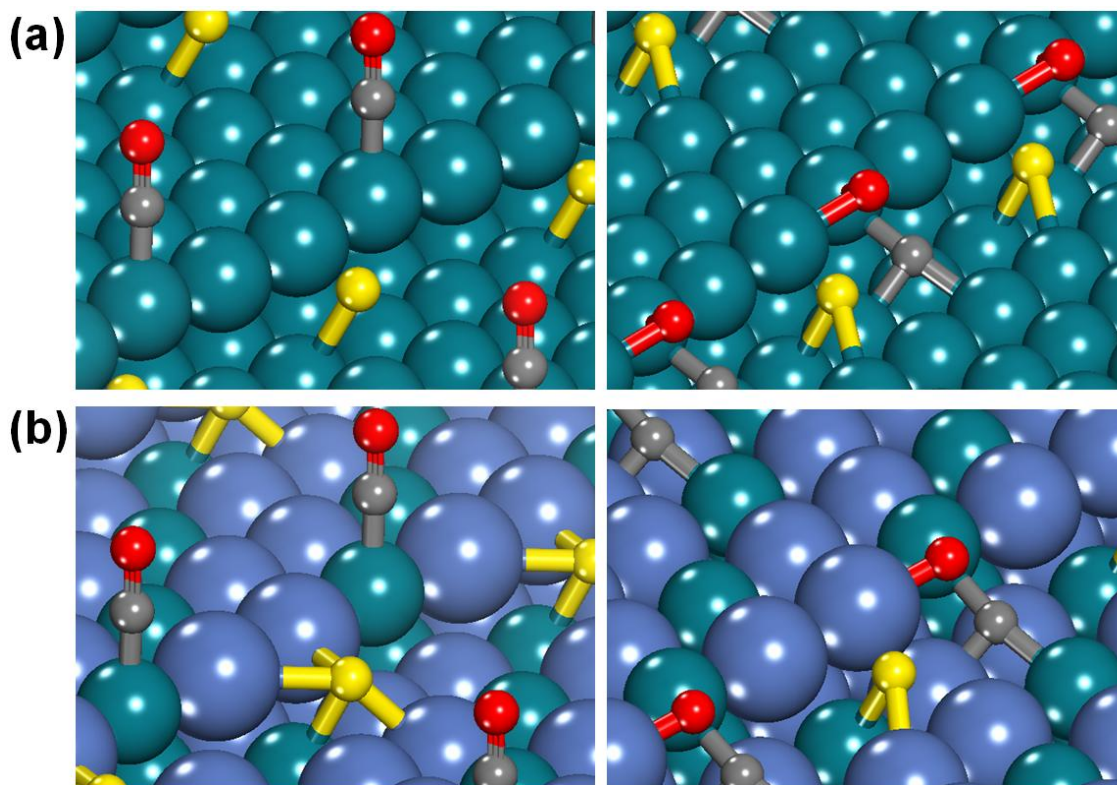


Figure 2-7. Initial (left) and transition (right) states on (a) the Rh (221) and (b) Rh<sub>1</sub>Ni<sub>2</sub> (221) stepped surfaces. (Rh and Ni: dark and light spheres in the substrate, respectively. C, O, S: grey, dark, and white spheres in the adsorbate layer, respectively.)

energies of S between Rh and Rh<sub>1</sub>Ni<sub>2</sub> stepped surfaces. A single metal atom is closely involved in S adsorption on the Rh(221) surface whereas four metal atoms are involved on the Rh<sub>1</sub>Ni<sub>2</sub>(221) surface. The difference of CO adsorption energy between the Rh and Rh<sub>1</sub>Ni<sub>2</sub> flat surfaces also does not appear on their stepped surfaces, indicating that the critical factor to determine CO dissociation rates on stepped surfaces is not the CO adsorption energy or the S adsorption energy but the CO activation barrier. According to Table 2-5, the Rh<sub>1</sub>Ni<sub>2</sub>(221) surface has the smallest barrier in the presence of S, as observed for the (111) surface of the same composition (Table 2-3). This results in a faster CO dissociation rate on the Rh<sub>1</sub>Ni<sub>2</sub> stepped surface compared to that on the Rh stepped surface. The sulfur tolerance of Rh<sub>1</sub>Ni<sub>2</sub> is not isolated to the (111) flat surfaces, and it is also significant on more active step sites.

## 2.4 Conclusions

Carbon monoxide (CO) dissociation energetics on bimetallic Rh-Ni surfaces were compared with pure Rh and Ni using DFT methods. Our results help explain experimental phenomena where the addition of Ni to a Rh catalyst improves its sulfur tolerance for steam reforming of S-containing liquid fuels. The adsorption energy of S is more endothermic on the Rh<sub>1</sub>Ni<sub>2</sub>(111) surface compared to the Rh(111) surface, suggesting that the sulfur poisoning of Rh catalysts can be reduced by the addition of Ni. The adsorption of S on metal surfaces radically increases the activation barrier for CO dissociation, but only the Rh<sub>1</sub>Ni<sub>2</sub> surfaces retarded such an increase of activation barrier. The analysis of the O 2p projected density of state shows that the repulsion between S and CO is weaker on Rh<sub>1</sub>Ni<sub>2</sub> than on Rh, minimizing the sulfur poisoning effects. A similar reduction in S poisoning of CO dissociation on the stepped Rh<sub>1</sub>Ni<sub>2</sub> surface is observed.

The conclusions noted above are based on the specific S coverage, alloy composition, and CO dissociation path chosen for study. Although the basis for each of these choices was discussed and

comparisons are made across a constant set of parameters, it is plausible that another configuration could allow for qualitatively different behavior. The results from these models provide results consistent with the reported experimental trend for bimetallic Rh-Ni catalysts,<sup>11</sup> suggesting that the sulfur tolerance for the CO dissociation reaction is improved by bimetallic catalysts that can weaken sulfur adsorption and be less affected in the elevation of CO dissociation barrier by sulfur poisoning. As C-O dissociation rates have been shown to correlate with C-H and C-C dissociation rates,<sup>13</sup> these results help explain the observed enhancement of S tolerance of Rh-Ni binary metal catalysts for hydrocarbon reforming reactions.

## 2.5 References

- (1) Holladay, J. D.; Hu, J.; King, D. L.; Wang, Y. *Catal Today* **2009**, *139*, 244.
- (2) Schadel, B. T.; Duisberg, M.; Deutschmann, O. *Catal Today* **2009**, *142*, 42.
- (3) Kang, I.; Bae, J.; Bae, G. *J Power Sources* **2006**, *163*, 538.
- (4) Palo, D. R.; Dagle, R. A.; Holladay, J. D. *Chem Rev* **2007**, *107*, 3992.
- (5) Sehested, J. *Catal Today* **2006**, *111*, 103.
- (6) Galea, N. M.; Lo, J. M. H.; Ziegler, T. *J Catal* **2009**, *263*, 380.
- (7) Hepola, J.; Simell, P. *Appl Catal B-Environ* **1997**, *14*, 305.
- (8) Inoglu, N.; Kitchin, J. R. *J Catal* **2009**, *261*, 188.
- (9) Lakhapatri, S. L.; Abraham, M. A. *Appl Catal a-Gen* **2009**, *364*, 113.
- (10) Chen, Y. S.; Xie, C.; Li, Y.; Song, C. S.; Bolin, T. B. *Phys Chem Chem Phys* **2010**, *12*, 5707.
- (11) Strohm, J. J.; Zheng, J.; Song, C. S. *J Catal* **2006**, *238*, 309.
- (12) Engbaek, J.; Lytken, O.; Nielsen, J. H.; Chorkendorff, L. *Surf Sci* **2008**, *602*, 733.
- (13) Wang, J. H.; Lee, C. S.; Lin, M. C. *Journal of Physical Chemistry C* **2009**, *113*, 6681.



- (14) Chen, J.; Liu, Z. P. *J. Am. Chem. Soc.* **2008**, *130*, 7929.
- (15) Andersson, M. P.; Abild-Pedersen, E.; Remediakis, I. N.; Bligaard, T.; Jones, G.; Engbæk, J.; Lytken, O.; Hørch, S.; Nielsen, J. H.; Sehested, J.; Rostrup-Nielsen, J. R.; Nørskov, J. K.; Chorkendorff, I. *J. Catal.* **2008**, *255*, 6.
- (16) Rostrup-Nielsen, J. R. *Phys Chem Chem Phys* **2001**, *3*, 283.
- (17) Song, C. S. *Catal Today* **2002**, *77*, 17.
- (18) Kugai, J.; Velu, S.; Song, C. S. *Catal Lett* **2005**, *101*, 255.
- (19) Kugai, J.; Subramani, V.; Song, C. S.; Engelhard, M. H.; Chin, Y. H. *J Catal* **2006**, *238*, 430.
- (20) Li, Y.; Wang, X. X.; Xie, C.; Song, C. S. *Appl Catal a-Gen* **2009**, *357*, 213.
- (21) Zhang, C. J.; Hu, P.; Lee, M. H. *Surf Sci* **1999**, *432*, 305.
- (22) Curulla-Ferre, D.; Govender, A.; Bromfield, T. C.; Niemantsverdriet, J. W. *J. Phys. Chem. B* **2006**, *110*, 13897.
- (23) Liu, Z. P.; Hu, P. *J. Chem. Phys.* **2001**, *114*, 8244.
- (24) Mavrikakis, M.; Baumer, M.; Freund, H. J.; Nørskov, J. K. *Catal. Lett.* **2002**, *81*, 153.
- (25) Liu, Z. P.; Hu, P. *J. Am. Chem. Soc.* **2003**, *125*, 1958.
- (26) Morikawa, Y.; Mortensen, J. J.; Hammer, B.; Nørskov, J. K. *Surf. Sci.* **1997**, *386*, 67.
- (27) Li, T.; Bhatia, B.; Sholl, D. S. *J. Chem. Phys.* **2004**, *121*, 10241.
- (28) Stroppa, A.; Mittendorfer, F.; Andersen, J. N.; Parteder, G.; Allegretti, F.; Surnev, S.; Netzer, F. P. *Journal of Physical Chemistry C* **2009**, *113*, 942.
- (29) Kresse, G.; Furthmüller, J. *Computational Materials Science* **1996**, *6*, 15.
- (30) Kresse, G.; Furthmüller, J. *Physical Review B* **1996**, *54*, 11169.
- (31) Kresse, G.; Hafner, J. *Physical Review B* **1993**, *47*, 558.
- (32) Perdew, J. P.; Burke, K.; Ernzerhof, M. *Physical Review Letters* **1996**, *77*, 3865.
- (33) Perdew, J. P.; Chevary, J. A.; Vosko, S. H.; Jackson, K. A.; Pederson, M. R.; Singh, D. J.; Fiolhais, C. *Physical Review B* **1992**, *46*, 6671.

- (34) Blochl, P. E. *Physical Review B* **1994**, *50*, 17953.
- (35) Donnay, J. D. H. *Crystal data; determinative tables*; 2d ed.; American Crystallographic Association: [Washington], 1963.
- (36) J. Guo, C. Xie, K. Lee, J. T. Miller, N. Guo, M. J. Janik, C.S. Song In *submitted to Journal of Catalysis* 2010.
- (37) Koch, H. P.; Singnurkar, P.; Schennach, R.; Stroppa, A.; Mittendorfer, F. *Journal of Physical Chemistry C* **2008**, *112*, 806.
- (38) Henkelman, G.; Jonsson, H. *J. Chem. Phys.* **1999**, *111*, 7010.
- (39) Hoffmann, R. *Reviews of Modern Physics* **1988**, *60*, 601.
- (40) vanDaelen, M. A.; Li, Y. S.; Newsam, J. M.; vanSanten, R. A. *J. Phys. Chem.* **1996**, *100*, 2279.
- (41) Nilsson, A.; Pettersson, L.; Nørskov, J. K. *Chemical bonding at surfaces and interfaces*; 1st ed.; Elsevier: Amsterdam ; Oxford, 2008.

## 2.6 Supporting Information

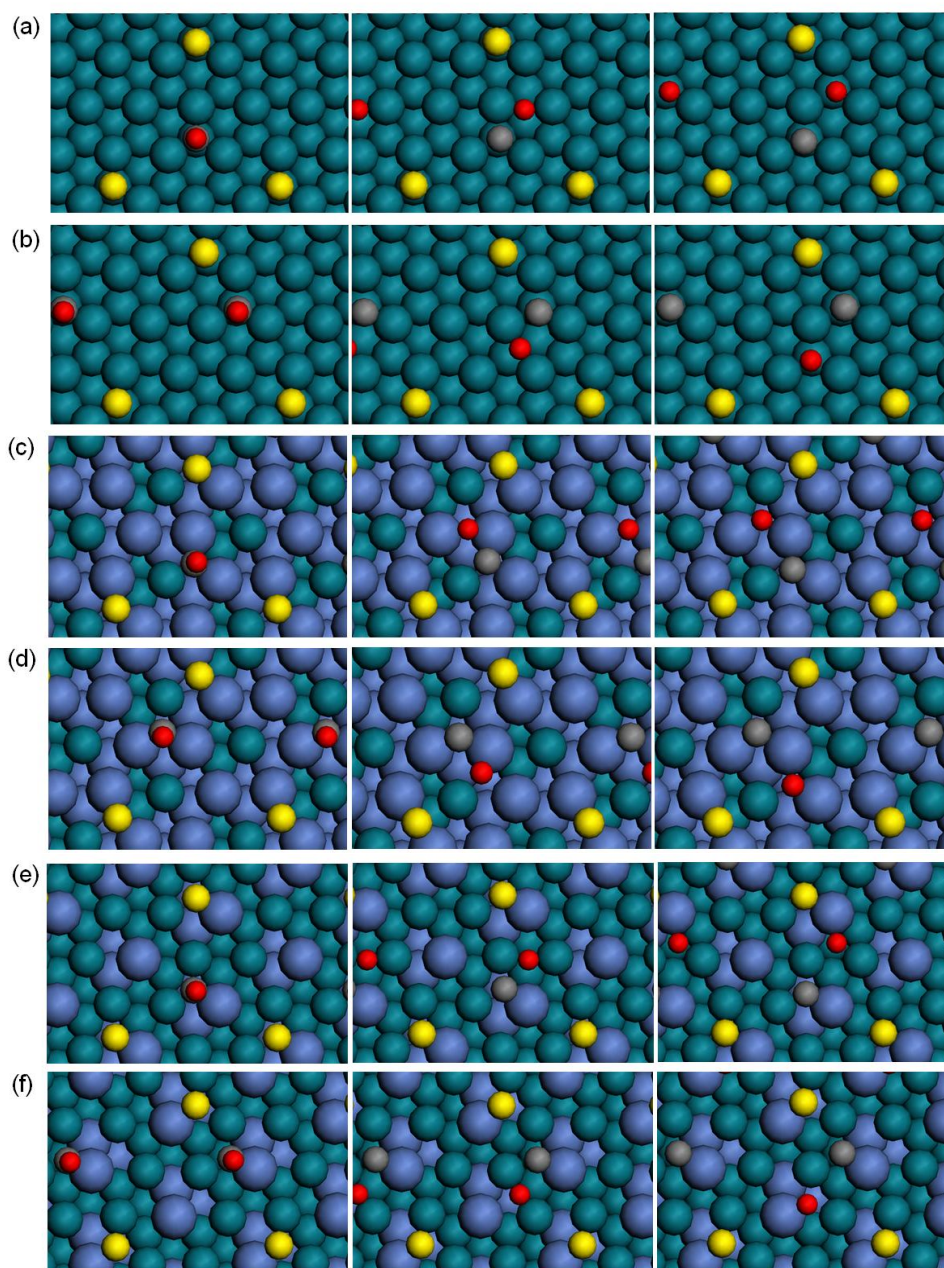


Figure S1. Initial (left), transition (middle), and final (right) states of CO dissociation on each metal for configuration A (a, c, and e) and configuration B (b, d, and f). (Rh and Ni: dark and light spheres in the substrate, respectively. C, O, S: grey, dark, and light adsorbate spheres, respectively.)

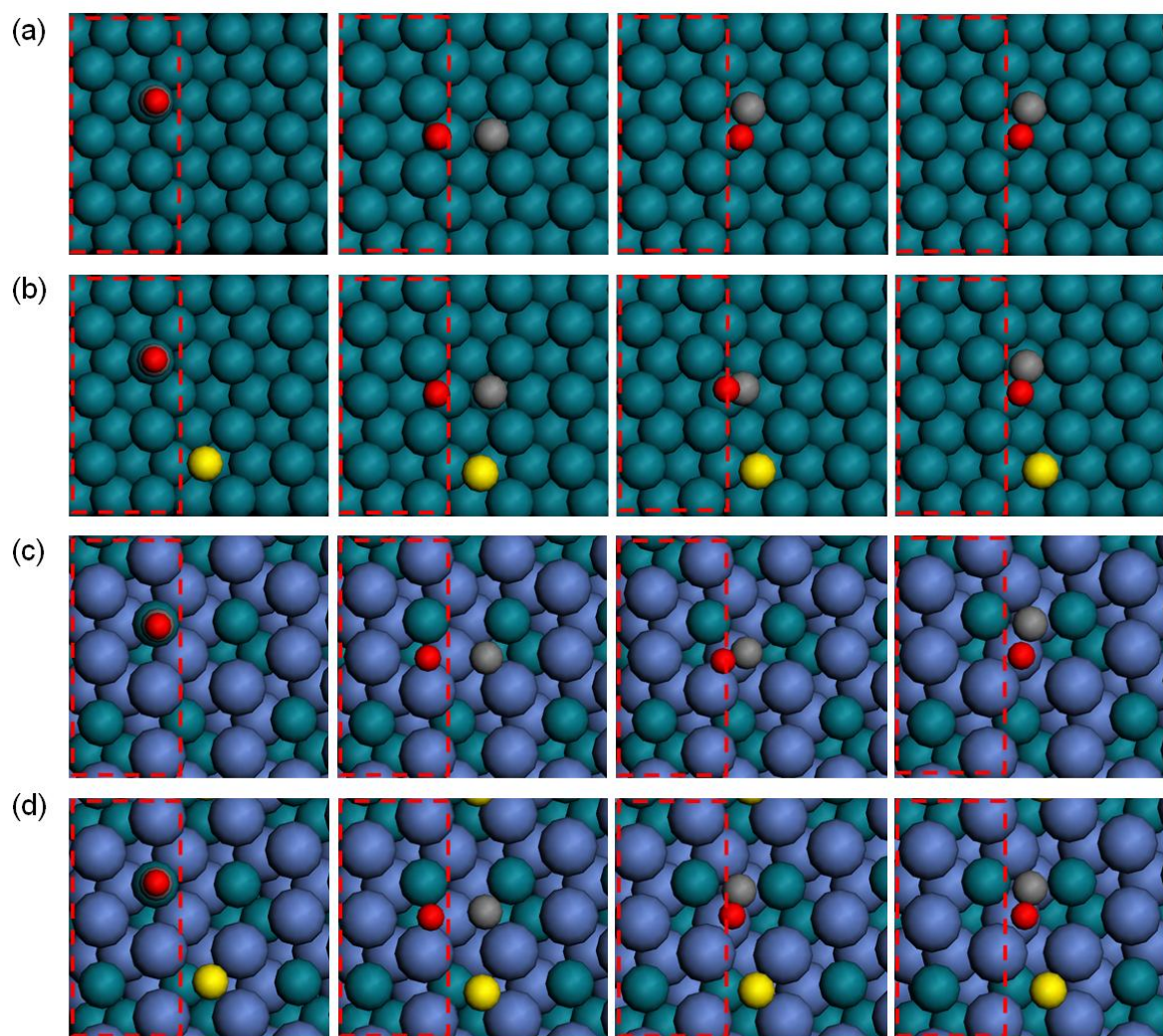


Figure S2. Initial, final, the highest energy image isolated by NEB method, and the transition state obtained by Dimer method (from left to right, respectively) on (a) Rh, (b) Rh with S, (c) Rh<sub>1</sub>Ni<sub>2</sub>, (d) Rh<sub>1</sub>Ni<sub>2</sub> with S. The dashed box indicates the higher level step on the surface.

### Chapter 3

## **An ab initio thermodynamics examination of sulfur species present on Rh, Ni, and binary Rh-Ni surfaces under steam reforming reaction conditions**

This chapter is published as: Kyungtae Lee, Chunshan Song, and Michael J. Janik, *Langmuir* 2012, 28, 5660-5668

**ABSTRACT:** The stable form of adsorbed sulfur species and their coverage were investigated on Rh, Ni and Rh-Ni binary metal surfaces using density functional theory calculations and the *ab initio* thermodynamics framework. S adsorption,  $\text{SO}_x$  ( $x=1\sim4$ ) adsorption, and metal sulfide formation were examined on Rh(111) and Ni(111) pure metals. Both Rh and Ni metals showed a preference for S surface adsorption rather than  $\text{SO}_x$  adsorption under steam reforming conditions. The transition temperature from a clean surface ( $<1/9$  ML) to S adsorption was identified on Rh(111), Ni(111),  $\text{Rh}_1\text{Ni}_2(111)$ , and  $\text{Rh}_2\text{Ni}_1(111)$  metals at various  $\text{P}(\text{H}_2)/\text{P}(\text{H}_2\text{S})$  ratios. Bimetallic Rh-Ni metals transition to a clean surface at lower temperatures than the pure Rh metal. Whereas Rh is covered with  $1/3$  ML sulfur under the reforming conditions of 4 ~100 ppmS and 800 °C,  $\text{Rh}_1\text{Ni}_2$  is covered with  $1/9$  ML sulfur in the lower end of this range (4~33 ppmS). The possibility of sulfate formation on Rh catalysts was examined by considering higher oxygen pressures, a Rh(221) stepped surface, and the interface between a  $\text{Rh}_4$  cluster and  $\text{CeO}_2(111)$  surface.  $\text{SO}_x$  surface species are stable only at high oxygen pressure or low temperatures outside those relevant to steam reforming of hydrocarbons.



### 3.1 Introduction

Hydrogen is a promising energy carrier for efficient, environmentally friendly energy conversions.<sup>1</sup> Hydrogen is produced industrially by the steam reforming of natural gas.<sup>2</sup> In addition to natural gas, liquid hydrocarbons and alcohols may be used as the feed in the reforming reaction for on-board and on-site fuel cell applications.<sup>3-6</sup> A more efficient steam reforming process can be achieved by overcoming four catalytic challenges: sulfur poisoning, intrinsic surface activity, carbon formation, and sintering.<sup>7</sup> Among them, sulfur poisoning is a critical issue since sulfur-poisoned catalysts lose activity and eventually catalyze carbon deposition.<sup>8</sup> Liquid hydrocarbon fuels such as jet fuel and diesel fuel inherently contain a certain amount of sulfur species. The sulfur content can be reduced to less than a few hundred ppm by desulfurization processes (i.e. hydrodesulfurization (HDS), selective alkylation of organo-sulfur molecules, and adsorptive approaches).<sup>9-11</sup> These processes increase the complexity of the system, have limitations in being industrially scaled-up, and cannot provide a completely sulfur-free fuel.<sup>12</sup> The development of sulfur tolerant catalysts can simplify the process and reduce the energy input associated with desulfurization. Rh-Ni catalysts have demonstrated higher sulfur tolerance than pure Rh.<sup>13</sup> We have previously corroborated this result using density functional theory (DFT) methods by showing that the CO dissociation rate, as a key reaction step sensing the sulfur poisoning level in the reforming reaction, is fastest on a binary Rh-Ni metal surface in the presence of sulfur.<sup>14</sup> Here, we report further DFT analysis examining the extent of surface sulfidation of Rh, Ni, and Rh-Ni binary metals under steam reforming conditions. Our results illustrate that sulfur tolerant Rh-Ni surfaces have lower S coverage under reaction conditions. In addition, it is challenging to experimentally identify the extent of oxidation of the sulfur poisoning species.<sup>15</sup> We examine the extent of S oxidation on Rh-Ni binary metal surfaces at varying gas compositions and temperatures.

The main sulfur compounds of liquid fuels such as jet fuel or diesel fuel are benzothiophene derivatives.<sup>11,13</sup> These derivatives are known to be decomposed to H<sub>2</sub>S in a reducing atmosphere and H<sub>2</sub>S

then poisons catalytic surfaces.<sup>16</sup> If sulfur compounds are exposed to an oxidizing atmosphere,  $\text{SO}_2$  is formed.<sup>17</sup> Thus, the conversion of  $\text{H}_2\text{S}$  gas to S and  $\text{SO}_x$  ( $x=1, 2, 3, 4$ ) adsorbed species may occur on the catalyst surface, depending on reaction conditions. Another possible sulfur poisoning path is through the conversion of metal particles to metal sulfides. The formation of  $\text{Ni}_3\text{S}_2$  has been reported at lower temperature and higher  $\text{H}_2\text{S}$  pressure than conditions causing sulfur adsorption on the Ni surface.<sup>18-20</sup> In this study, we consider  $\text{Ni}_3\text{S}_2$  and  $\text{Rh}_{17}\text{S}_{15}$  as metal sulfide phases of Rh and Ni. These are stable phases according to the binary alloy phase diagram<sup>21</sup> for a sulfur:metal atomic ratio of 0.3 at 500 °C. Strohm et al. reported that sulfur poisoning starts to impact fuel conversion when the atomic ratio of sulfur in the fuel to surface Rh reaches 0.3 during reforming, regardless of the  $\text{H}_2\text{S}$  content in the feedstock.<sup>13</sup>

The sulfur poisoning of reforming catalysts was reported to be diminished using bimetallic catalysts by Strohm et al.<sup>13</sup> They showed that a Rh catalyst supported on  $\text{CeO}_2\text{-Al}_2\text{O}_3$  showed an over 97% fuel conversion for sulfur-free jet fuel, whereas it is rapidly deactivated in the liquid fuel with the sulfur content over 10 ppm. This weak sulfur tolerance of Rh was overcome by adding 2 ~ 20 wt% Ni to 2 wt% Rh. The addition of Ni to Rh formed a bimetallic catalyst with a close interaction, which is confirmed by temperature-programmed reduction (TPR),<sup>13</sup> X-ray photoelectron spectroscopy (XPS),<sup>13</sup> and extended X-ray absorption fine structure (EXAFS)<sup>22</sup> analyses. The methane formation reaction was found by Strohm et al. to be more sensitive to sulfur poisoning, deactivating at a 0.15  $\text{S}_{\text{fuel}}:\text{Rh}_{\text{surf}}$  ratio as opposed to a 0.28-0.30 ratio for the overall reforming reaction. Thus, we previously examined the CO dissociation rate, a rate-determining step of methanation, on binary  $\text{Rh}_1\text{Ni}_2$  and  $\text{Rh}_2\text{Ni}_1$  surfaces using DFT calculations.<sup>14</sup> Our results showed that the CO dissociation rate is fastest on the pure sulfur free Rh surface, whereas, in the presence of co-adsorbed sulfur, the rate is fastest on the  $\text{Rh}_1\text{Ni}_2$  binary surface. We observed two phenomena responsible for this behavior. First, the CO dissociation rate in the presence of co-adsorbed S atoms is fastest on the binary metal surface, indicating that adding Ni to Rh lessens the repulsive interactions of S with adsorbates. Second, the binding energy of S on Rh-Ni surfaces is less exothermic

than on the pure Rh surface. The impact of this weaker binding energy on the adsorbed sulfur coverage under operating conditions is examined herein.

Many studies have suggested that sulfur poisoning on catalysts occurs through atomic sulfur adsorption.<sup>16,23-25</sup> Recently, X-ray adsorption near edge structure (XANES) studies suggested that reforming catalyst poisoning is due to atomic sulfur adsorption for a Ni catalyst, whereas sulfate adsorption occurs on a Rh catalyst.<sup>15,26</sup> However, there are also several reports indicating a preference of Rh catalysts toward atomic S adsorption. XPS analysis indicated that atomic S adsorption is preferred under H<sub>2</sub>O environments, whereas S is removed as SO<sub>2</sub> under O<sub>2</sub> environments.<sup>27</sup> XPS and Near-Edge X-ray Absorption Fine Structure (NEXAFS) analysis indicated that dimethyl sulfide is dissociated into S atoms on the Rh surface, but is not on the Ni surface.<sup>28,29</sup> The experimental conditions differ among these studies. Ab initio thermodynamics may be used to determine the stable adsorbed SO<sub>x</sub> species as a function of operating conditions. We compared SO<sub>x</sub> (x=1~4) and S adsorption preferences on the Rh(111) surface, a Rh(221) stepped surface, and a Rh<sub>4</sub> cluster supported on a CeO<sub>2</sub>(111) surface. We report the thermodynamically preferred sulfur poisoning species under steam reforming conditions, compare the stable species and coverage among binary metals (Rh<sub>1</sub>Ni<sub>2</sub> and Rh<sub>2</sub>Ni<sub>1</sub>) and pure metals (Rh, Ni), and examine stepped and supported Rh surfaces.

## 3.2 Methods

### 3.2.1 Electronic structure methods.

Calculations were carried out using the Vienna Ab-Initio Simulation Program (VASP), an ab initio total-energy and molecular dynamics program developed at the Institute for Material Physics at the University of Vienna.<sup>30-32</sup> The electron-ion interactions are described by the projector augmented wave



method.<sup>33</sup> The Perdew–Wang (PW91) version of the generalized gradient approximation (GGA) was used to incorporate exchange and correlation energies.<sup>34,35</sup> The cut-off energy of the plane-wave basis set applied to represent valence electrons was 400 eV for Rh, Ni, and Ni<sub>3</sub>S<sub>2</sub>, 450 eV for Rh supported on CeO<sub>2</sub>, and 500 eV for Rh<sub>17</sub>S<sub>15</sub>. These cut-off energies were determined to produce a change in the total energy less than 0.03 eV with respect to the total energy obtained with a substantially higher cutoff energy. The gamma point only was used for k-point sampling of isolated molecules. All calculations for Ni, CeO<sub>2</sub>, the isolated S atom, and isolated SO<sub>x</sub> molecules were spin-polarized. Structural optimization was carried out by minimizing the forces on all atoms to less than 0.05 eV Å<sup>-1</sup>. Zero-point vibrational energy (ZPVE) was determined by calculating harmonic vibrational modes. For surface systems with adsorbates, their harmonic vibrations for ZPVE were calculated by relaxing only adsorbates. The DFT+U method was adopted to represent an on-site Coulombic interaction in the *f* states of ceria as DFT has a limitation in describing the nature of 4*f* states in ceria.<sup>36-38</sup> The U term enables localization of electrons in the *f* states for reduced ceria structures such as CeO<sub>2-x</sub>. We performed the ceria calculation using a U value of 5 eV, which was previously recommended.<sup>39-41</sup>

### 3.2.2 Model construction.

All isolated molecules were optimized in a 10Å × 10Å × 10Å unit cell. Flat surfaces of Rh, Ni, Rh<sub>1</sub>Ni<sub>2</sub>, Rh<sub>2</sub>Ni<sub>1</sub> and a stepped surface of Rh were terminated by (111) and (221) facets, respectively, and each slab was separated by a vacuum region of 10 Å normal to the surface. The (111) surfaces consist of a total of five metal layers with the top three layers relaxed. The Rh (221) stepped surface has six layers with the top three relaxed, and its detailed description is given in ref<sup>14</sup>. All 3 × 3 surface cells, the Rh<sub>1</sub>Ni<sub>2</sub> and Rh<sub>2</sub>Ni<sub>1</sub>  $\sqrt{3} \times \sqrt{3}$  cells, and the Rh(221) surface used (5 × 5 × 1) gamma centered k-point meshes. Rh and Ni 2 × 2 and  $\sqrt{3} \times \sqrt{3}$  surface cells used (7 × 7 × 1) and (6 × 6 × 1) gamma centered grids. The

optimized lattice parameters for bulk Rh and Ni are 3.800 and 3.520 Å which are within 0.08 and 0.11 % differences from the experimental values.<sup>42</sup> The Rh-Ni binary metals were modeled by regularly distributing Ni and Rh atoms as shown in Figure 3-1 a, b.

Ni<sub>3</sub>S<sub>2</sub> and Rh<sub>17</sub>S<sub>15</sub> bulk structures were based on D<sub>3</sub><sup>7</sup>(R32) and O<sub>h</sub><sup>1</sup>(Pm3m) atomic arrangements, respectively,<sup>43</sup> as shown in Figure 3-1 c and d, which are consistent with previous reports to model and calculate those structures.<sup>44,45</sup> The Brillouin zone was sampled using (4 × 4 × 4) and (3 × 3 × 3) Monkhorst-Pack (MP)<sup>46</sup> grids for Ni<sub>3</sub>S<sub>2</sub> and Rh<sub>17</sub>S<sub>15</sub>, respectively. Bulk Ni and Rh metals used as the reference state for the formation energy calculation of Ni<sub>3</sub>S<sub>2</sub> and Rh<sub>17</sub>S<sub>15</sub> were modeled using the (7 × 7 × 7) and (8 × 8 × 8) MP grids, respectively.

The ceria surface slab is modeled with six layers with a (111) termination from cubic fluorite CeO<sub>2</sub> and each slab is separated by 15 Å of vacuum. The CeO<sub>2</sub>(111) surface is a representative facet constituting a large proportion of a polycrystalline CeO<sub>2</sub> surface.<sup>40,47</sup> The Brillouin zone was sampled with a (1 × 1 × 1) MP grid. We use a 4 × 4 surface unit cell, which has sixteen oxygen atoms on the top layer and sixteen Ce atoms in the layer below. To simulate a Rh particle on a ceria surface, we placed and optimized a Rh<sub>4</sub> cluster on the CeO<sub>2</sub>(111) surface (Figure. 3-1e) at the three-folded site of the CeO<sub>2</sub>(111) surface, as shown to be preferable by Lu et al.<sup>48</sup>

The 0 K binding energies of adsorbates are calculated as the DFT energy difference with zero-point vibrational energy corrections between the adsorbed state and the isolated gas molecule and surface, with negative values indicating an exothermic adsorption.

### 3.2.3 Gibbs free energy determination.

Gas pressures used for Gibbs free energy calculations were chosen based on Strohm et al.'s experimental reforming conditions.<sup>13</sup> Strohm et al. used normal paraffins with an average carbon number of 13 as a feed along with steam where the steam-to-carbon molar ratio is 3:1. Their selectivity in the

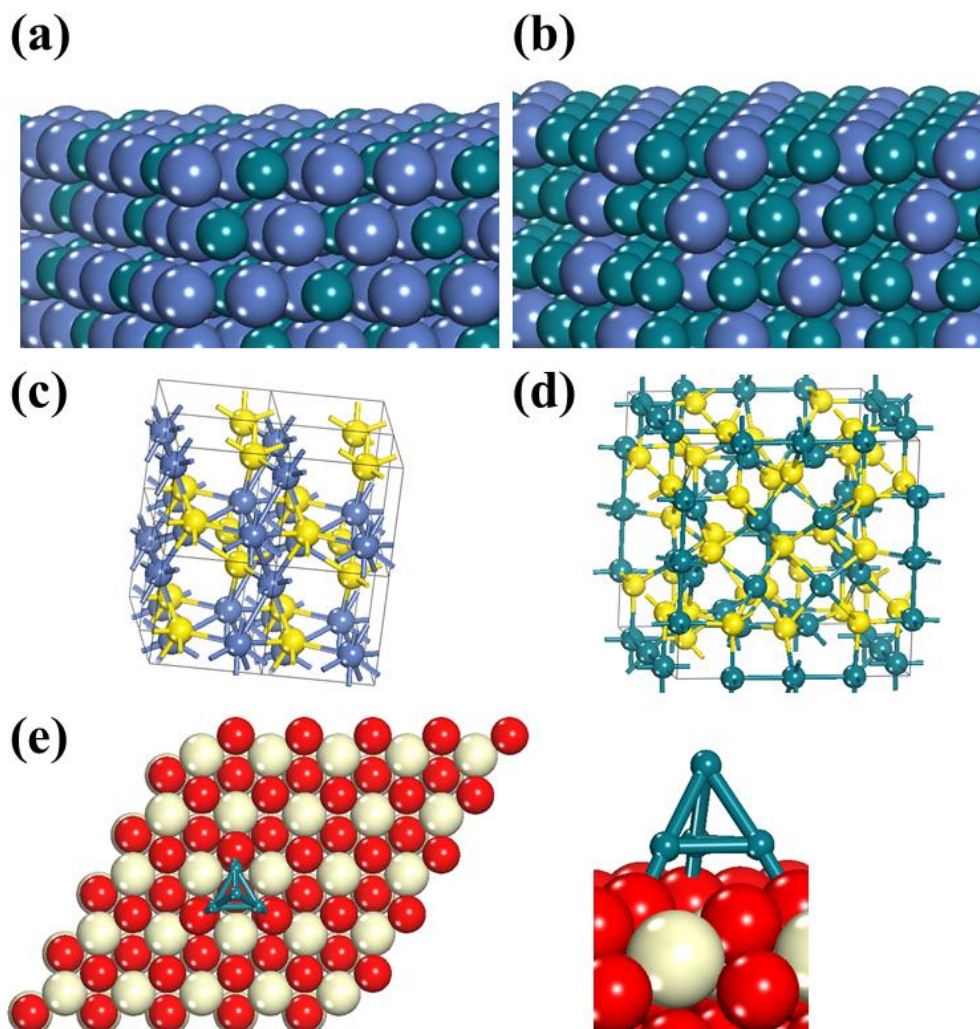
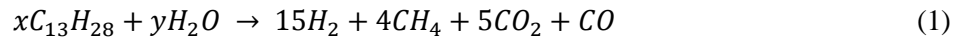


Figure 3-1. Structural images of (a)  $\text{Rh}_1\text{Ni}_2$  surface, (b)  $\text{Rh}_2\text{Ni}_1$  surface, (c) bulk  $\text{Ni}_3\text{S}_2$ , (d) bulk  $\text{Rh}_{17}\text{S}_{15}$ , and (e)  $\text{Rh}_4$  cluster on  $\text{CeO}_2(111)$  surface. ((a-d) dark gray sphere (green): Rh, light gray sphere (blue): Ni, white sphere (yellow): S. (e) large gray sphere (red): O, small gray sphere (green): Rh, white sphere (white): Ce.)

product stream was 15: 4: 5: 1 of  $H_2$ :  $CH_4$ :  $CO_2$ :  $CO$ . This molar ratio is expressed as the following stoichiometric ratio,



Balancing the left and right sides gives  $x=10/13$  and  $y=159/13$  and the excessive steam after the chemical reaction of Eq. 1 was considered in the product stream. Strohm et al. used 4, 33, and 100 ppm of 3-methylbenzothiophene to induce sulfur poisoning ( $x$  ppm denotes the sulfur content of the liquid fuel). We consider  $H_2S$  gas instead of 3-methylbenzothiophene as a sulfur poisoning compound because sulfur compounds are converted into  $H_2S$  under steam reforming condition.<sup>16</sup> If we use 33 ppmS, the molar ratio of  $H_2S$ :  $C_{13}H_{28}$  is 0.00018 ( $P_{H_2S} = 3.24 \times 10^{-6}$  atm based on Eq. 2). For a wide scan, we varied the range of  $H_2S$  pressure from  $1.0 \times 10^{-9}$  to  $6.0 \times 10^{-1}$  atm. The reforming reaction was conducted at a total pressure of 1 atm:

$$P(H_2) + P(H_2O) + P(H_2S) + P(CO) + P(CO_2) + P(CH_4) = 1 \text{ atm} \quad (2)$$

If a pressure change of  $H_2S$  or  $H_2O$  is applied, the other gas pressures are changed proportionately according to Eq. 2. The gas pressure is used to calculate the chemical potentials of each gas by

$$G_{gas} = E_{DFT} + ZPVE + \Delta U(T) + PV - (S_{vib} + S_{trans} + S_{rot})T \quad (3)$$

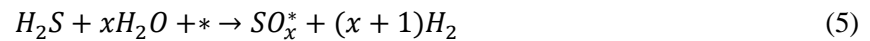
where  $E_{DFT}$  is the 0 K energy obtained from DFT methods, ZPVE is the zero-point vibration energy correction,  $\Delta U(T)$  is the internal energy change relative to 0 K, and the fourth term is a summation of vibrational, translational, and rotational entropies. All of the terms except  $E_{DFT}$  are calculated based on statistical thermodynamic equations in the ideal gas limit<sup>49</sup> using harmonic vibrational frequencies

obtained from DFT methods. The formation free energies of SO, SO<sub>2</sub>, SO<sub>3</sub>, and H<sub>2</sub>SO<sub>4</sub> gases from H<sub>2</sub>S and H<sub>2</sub>O gases by Eq. 3 are in good agreement to those calculated from experimental thermodynamic tables, as given in Table S1. Contribution of solid phonon modes are neglected, presuming these will cancel when considering adsorption or surface reaction. For surface adsorbed species, the chemical potential was calculated as

$$G_{adsorbate} = E_{DFT} + ZPVE + \Delta U(T) - (S_{vib} + S_{conf})T \quad (4)$$

where configurational entropy ( $S_{conf}$ ) is given as  $R \times \ln[(1-\theta)/\theta]$  ( $R$ : gas constant,  $\theta$ : fractional coverage of the surface).<sup>50</sup>

SO<sub>x</sub> (x=0~4) formation on surfaces occurs from H<sub>2</sub>S gas with H<sub>2</sub>O as the O source through the reaction



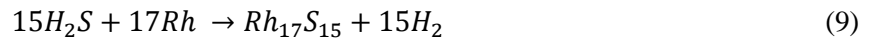
where \* denotes the bare surface and A\* denotes an adsorbed species. The free energy change of SO<sub>x</sub> adsorption is given by

$$\Delta G_{SO_x} = G_{SO_x^*} + (x+1)G_{H_2} - G_{H_2S} - xG_{H_2O} - E_{surface} \quad (6)$$

The chemical reaction of metal sulfide formation and the corresponding free energy change are given as:



$$\Delta G_{sulfide} = E_{Ni_3S_2} + 2G_{H_2} - 2G_{H_2S} - 3E_{Ni} \quad (8)$$



$$\Delta G_{sulfide} = E_{Rh_{17}S_{15}} + 15G_{H_2} - 15G_{H_2S} - 17E_{Rh} \quad (10)$$

We considered three different coverage models of  $\theta = 1/9$ ,  $1/4$ , and  $1/3$ , which were carried out by placing an adsorbate in unit cells of  $3 \times 3$ ,  $2 \times 2$ , and  $\sqrt{3} \times \sqrt{3}$ . To evaluate the free energy changes associated with varying surface coverage, the free energy differences associated with the following transformations were considered:

$$4 \times (G_{surface+adsorbate} \text{ of } \theta = 1/9) + 5H_2S \rightarrow 9 \times (G_{surface+adsorbate} \text{ of } \theta = 1/4) + 5H_2 \quad (11)$$

$$(G_{surface+adsorbate} \text{ of } \theta = 1/9) + 2H_2S \rightarrow 3 \times (G_{surface+adsorbate} \text{ of } \theta = 1/3) + 2H_2 \quad (12)$$

$$3 \times (G_{surface+adsorbate} \text{ of } \theta = 1/4) + H_2S \rightarrow 4 \times (G_{surface+adsorbate} \text{ of } \theta = 1/3) + H_2 \quad (13)$$

where the stoichiometric coefficients properly balance the number of metal atoms used to construct the various coverages as listed in Table S2.

### 3.3 Results and Discussion

#### 3.3.1 $\text{SO}_x$ ( $x=0\sim4$ ) adsorption on Rh and Ni surfaces at 1/9 coverage.

Favorable adsorption sites were investigated in order to calculate free energies of  $\text{SO}_x$  adsorption on Rh(111) and Ni(111) surfaces. For S adsorption, atop, fcc hollow, and hcp hollow sites were examined at a 1/9 coverage. The fcc site is preferred on both metals. For SO adsorption, fourteen configurations were considered by placing vertically and horizontally the SO molecule on the surfaces at various sites. The preferred adsorption mode has the SO molecule vertically adsorbed with S at the hcp site on Rh and S at the fcc site on Ni (Figure 3-2). Eighteen configurations were tested for a  $\text{SO}_2$  molecule and nineteen configurations for  $\text{SO}_3$  and  $\text{SO}_4$  molecules. The higher the number of  $x$  in a  $\text{SO}_x$  molecule, the more adsorption contact points of the oxygen atom on a surface. The most favorable sites for each molecule are illustrated in Figure 3-2 and adsorption energies and bond lengths are specified in Table 3-1. Adsorption energy data shows that all adsorbates bind more strongly to Rh(111) than Ni(111), implying that Rh surface may be more covered by sulfur under reforming conditions.

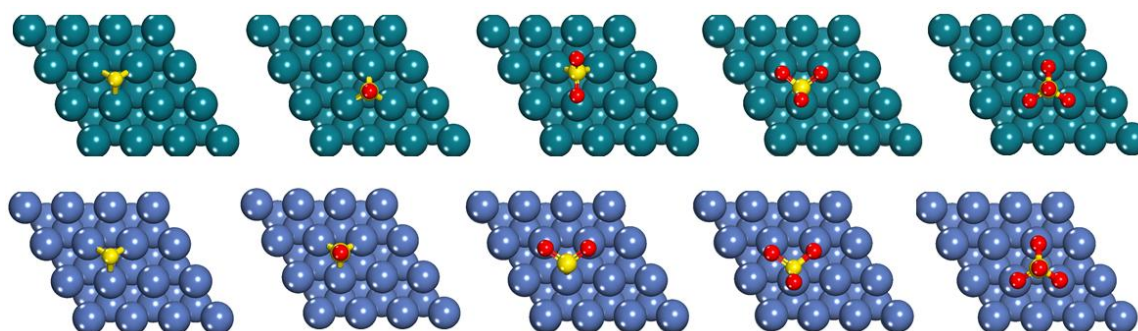


Figure 3-2. The most preferred adsorption configurations of S, SO,  $\text{SO}_2$ ,  $\text{SO}_3$ , and  $\text{SO}_4$  (from left to right) on Rh (top) and Ni (bottom) at 1/9 ML coverage.

Figure 3-3 illustrates the free energy of  $\text{SO}_x^*$  and  $\text{O}^*$  adsorption as a function of  $\text{H}_2\text{S}$  partial pressure at 500 K and 1000 K. The free energy change of  $\text{SO}_x$  adsorption was calculated based on the preferred adsorbate configuration using Eq. 6. The energy change of O atom adsorption was calculated at the preferred fcc hollow site. The calculation of the bulk metal sulfide formation was performed with Eq. 8 & 10, and Figure 3-3 a & c are shaded in the region of  $\text{H}_2\text{S}$  pressures for which bulk sulfide formation is favorable ( $\Delta G_{\text{sulfide}} < 0$ ). Outside the shaded region, a surface adsorbate layer is stable if any  $\Delta G_{\text{SO}_x} < 0$ , and the most stable adsorbate has the lowest  $\Delta G$  value. Low temperatures and high  $\text{H}_2\text{S}$  pressures lead to bulk metal sulfide formation. Intermediate values produce a surface  $\text{S}^*$  layer, whereas high temperatures and low  $\text{H}_2\text{S}$  pressures lead to a clean surface. Under the reforming gas pressures considered, bulk sulfide formation is unfavorable and  $\text{S}^*$  adsorption is preferred over  $\text{SO}_x^*$  ( $x=1\sim 4$ ) or  $\text{O}^*$  adsorption.

Table 3-1. Adsorption energies and bond lengths of  $\text{SO}_x$  adsorption at the most preferred sites on the Rh(111) and Ni(111) surfaces.

	Rh(111)				Ni(111)			
	$\Delta E_{\text{ads}}$ (eV)	$d_{\text{S-M}}^{\text{a}}$ (site), Å	$d_{\text{O-M}}^{\text{b}}$	$d_{\text{S-O}}^{\text{c}}$	$\Delta E_{\text{ads}}$ (eV)	$d_{\text{S-M}}^{\text{a}}$ (site)	$d_{\text{O-M}}^{\text{b}}$	$d_{\text{S-O}}^{\text{c}}$
S	-5.43	2.27 (fcc)	-	-	-5.13	2.14 (fcc)	-	-
SO	-3.28	2.24 (hcp)	-	1.48	-2.77	2.10 (fcc)	-	1.48
$\text{SO}_2$	-1.49	2.27(bridge)	2.18	1.46 (1.54)	-1.26	2.18 (off atop)	1.98	1.55
$\text{SO}_3$	-1.98	2.28 (off atop)	2.10	1.45 (1.56)	-1.73	2.13 (off atop)	1.97	1.45 (1.56)
$\text{SO}_4$	-4.71	-	2.08	1.43 (1.54)	-4.66	-	1.93	1.43 (1.54)

<sup>a</sup>Multiple bonds at bridge and hollow sites are averaged.

<sup>b</sup>When more than two oxygen atoms interact with the surface, the bond lengths are similar and their average values are listed here.

<sup>c</sup>There are two groups of S-O bond differing by whether the O atom is directly interacting with the surface. The first value listed is for  $\text{S-O}_{\text{surface}}$  and the parenthetical refers to the other S-O bonds. The former is listed first and the latter is in parenthesis. If there are multiple S-O bonds of the same type, their average value is listed.



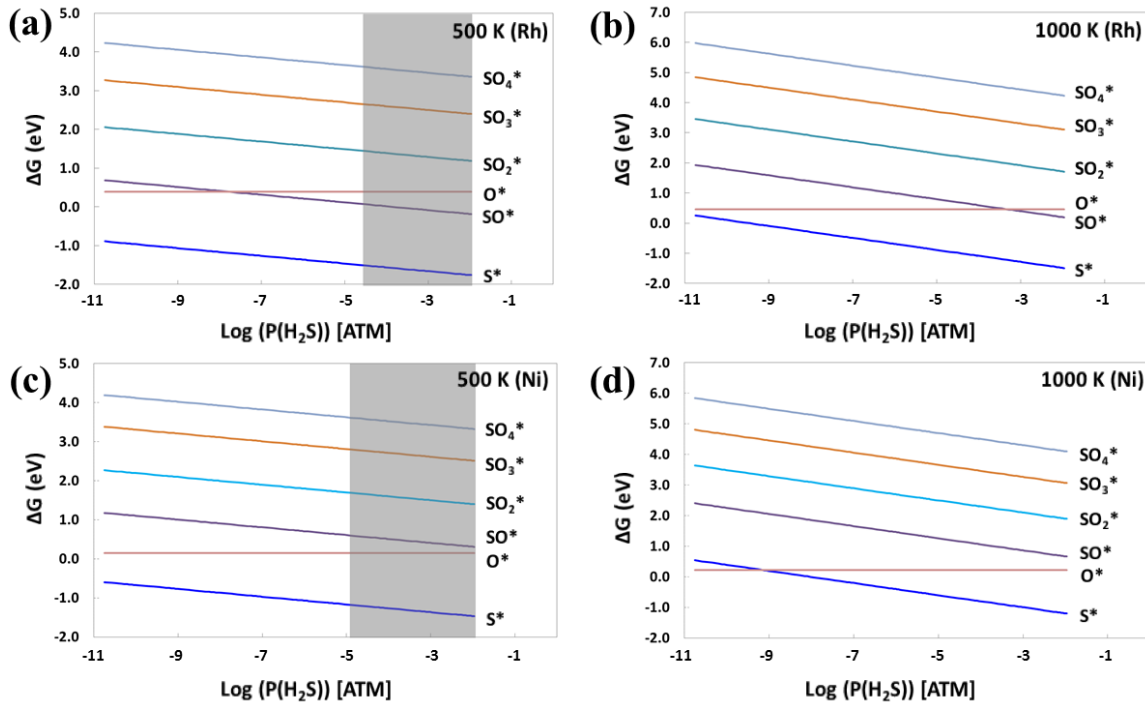


Figure 3-3. Free energy changes for adsorption of S, O,  $SO_x$  ( $x=1, 2, 3, 4$ ) are calculated via Eq. 6 and plotted versus pressure of  $H_2S$  gas on Rh(111) at (a) 500 and (b) 1000 K, and Ni(111) at (c) 500 and (d) 1000 K. The shaded regions represent  $H_2S$  pressures over which the bulk metal sulfides ( $Rh_{17}S_{15}$  or  $Ni_3S_2$ ) are determined to be stable. Gas pressures used for this graphs were calculated to satisfy Eq. 2 at varying  $H_2S$  pressures:  $P(H_2O)=0.411\sim0.415$  atm,  $P(H_2)=0.347\sim351$  atm,  $P(CH_4)=0.0925\sim0.0935$  atm,  $P(CO_2)=0.1157\sim0.1169$  atm,  $P(CO)=0.0231\sim0.0234$  atm, and  $P(H_2S)=1.07\times10^{-2}\sim1.80\times10^{-11}$  atm.

### 3.3.2 Sulfidation phase diagram of pure Rh and Ni metals.

The calculation performed at the specific temperatures and gas pressures of Figure 3-3 can be extended to a wide temperature and pressure range. The experimental conditions for the steam reforming process considered here range from 500 °C to 800 °C and from  $10^{-6}$  to  $10^{-7}$  atm in  $P(H_2S)$ , as mentioned in the section 3.2.3. We considered the temperature range from 400 K to 1800 K and the  $P(H_2S)$  range from  $10^{-2}$  to  $10^{-11}$  atm, well beyond the experimental reforming ranges in order to observe more extensive phase behavior. The stable phases are identified over these ranges in Figure 3-4 a, b where the abscissa is the ratio of  $P(H_2)/P(H_2S)$ . Figure 3-4a exhibits that the adsorbed  $S^*$  phase is stable on Rh(111) at higher

temperatures and lower  $\text{H}_2\text{S}$  pressures than Ni(111), which results from the stronger adsorption of S atoms. Metal sulfide formation for both Rh and Ni occurs at nearly identical conditions. Our Ni(111) phase diagram is compared in Figure 3-4b with experimental data and Wang et al.'s calculated phase diagram,<sup>18</sup> determined using enthalpy values in thermodynamic tables and DFT calculations. Our phase boundary from S adsorption to a clean surface is similar to Wang's et al.'s curve, but the inclusion of configurational entropy in our calculations provides a better match to the experimental data.<sup>51</sup> Our  $\text{Ni}_3\text{S}_2$  formation region differs from Wang's et al. and experimental data. This discrepancy likely arises from our neglect of Ni and  $\text{Ni}_3\text{S}_2$  phonon corrections. This values amounts to a 40~200 kJ mole<sup>-1</sup> correction at the temperatures between 750 and 1500 K in several metal oxides or carbonates.<sup>52,53</sup> The bulk sulfide formation region is well outside that of interest for the reforming reaction, and is not given further consideration.

The effect of steam pressure on the phase diagram was examined by changing the range of  $\text{P}(\text{H}_2\text{O})$  from 0.2 to 0.9 atm. The varied  $\text{H}_2\text{O}$  pressure did not alter the stable phase (i.e., did not lead to an  $\text{SO}_x(x=1\sim4)$  or O species becoming the stable phases), suggesting that though  $\text{H}_2\text{O}$  is an oxygen-containing species, it cannot provide an oxygen source to convert from sulfur to sulfur oxides at  $\text{H}_2\text{O}$  pressures up to 0.9 atm. We further examined the range of  $\text{P}(\text{H}_2)/\text{P}(\text{H}_2\text{O})$  ratio to induce sulfur oxide formation as shown in Figure S2. The logarithm pressure ratios for sulfur oxide formation are less than -5.5, which is far less than normal reforming conditions (e.g. the experimental condition considered herein corresponds to a log ratio of 0.8). This implies that, thermodynamically, there is no driving force for Ni or Rh (111) catalytic surfaces to form adsorbed sulfur oxides under steam reforming conditions. This issue will be addressed in more detail in section 3.3.4.

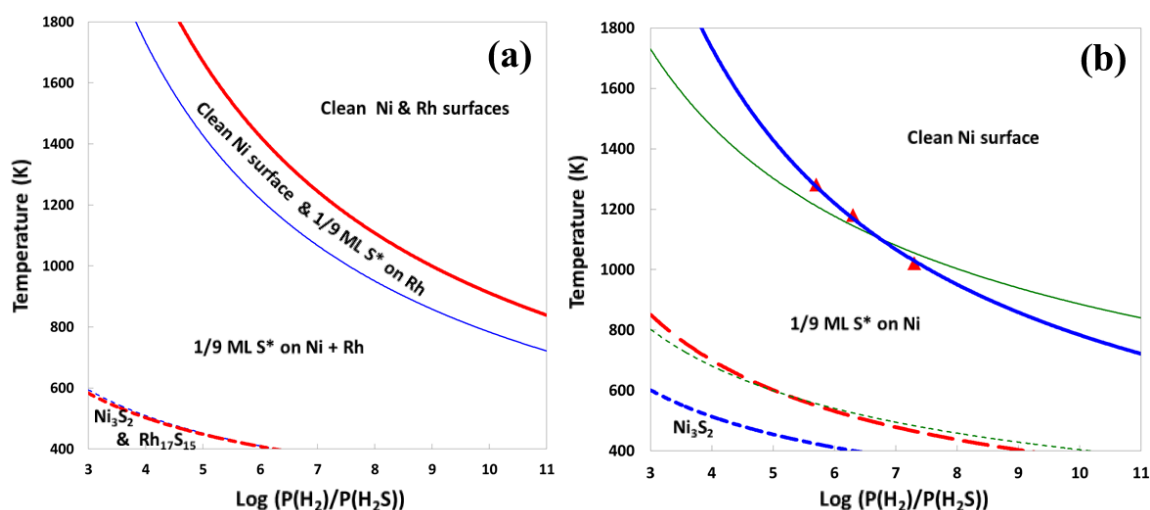


Figure 3-4. Sulfidation phase diagrams of (a) Rh (thick solid and short-dashed lines, red) and Ni (thin solid and short-dashed lines, blue), (b) comparison of our calculated Ni(111) phase diagram (thick solid and short-dashed lines, blue) with literature data: experimental data for the S\*-clean surface transition (▲) and bulk sulfide formation (thick long-dashed line, red)<sup>19, 20, 25</sup> and Wang et al.'s calculation for the S\*-clean surface transition (thin solid line, green) and bulk sulfide formation (thin short-dashed line, green).<sup>18</sup>

### 3.3.3 Rh-Ni binary metal surfaces at varying S\* coverage.

The phase boundaries of sulfur adsorption on Rh<sub>1</sub>Ni<sub>2</sub>(111) and Rh<sub>2</sub>Ni<sub>1</sub>(111) are added to the phase diagram of Rh(111) and Ni(111) in Figure 3-5. Only atomic S adsorption was considered on the binary metal surfaces, as SO<sub>x</sub> species were not found to be favorable on either of the pure metals. Sulfur adsorption energies on both binary metals are calculated at a fcc hollow site, which was reported as the most preferred site in our previous study<sup>14</sup>. The sulfur adsorption energies on Rh<sub>1</sub>Ni<sub>2</sub> and Rh<sub>2</sub>Ni<sub>1</sub> are -5.27 and -5.45 eV, respectively. The phase diagram in Figure 3-5a reflects the adsorption energy trend; Rh<sub>1</sub>Ni<sub>2</sub>(111) has an appreciably larger clean surface region than pure Rh(111). The S\*/clean boundary is drawn based on 1/9 ML S coverage, for which all surfaces are found to be in the S\* region under relevant reforming conditions. For this reason, we further delineate the boundaries to higher coverages of 1/4 and 1/3 ML.

Though the increase in equilibrium  $S^*$  coverage with higher  $H_2S$  pressure may be continuous, we have discretized this into regions of  $1/3$ ,  $1/4$ , and  $1/9$  coverage for comparison among surface compositions. The discrete “phase boundaries” considered between these coverages are therefore an approximation of what would truly be a continuous transition, and the term “phase diagram” is liberally applied in this case. The boundaries of the various coverage regions are exhibited for all surfaces in Figure S1. The phase diagram has four different regions for each surface: sulfur coverage of 0 ML (i.e. clean surface),  $1/9$  ML,  $1/4$  ML, and  $1/3$  ML. In the reforming region, the equilibrium coverage varies considerably between Ni and Rh. To provide a direct analysis of alloying effects, we compare Rh(111) and  $Rh_1Ni_2(111)$  in Figure 3-5b. Experimental conditions of 4, 33, and 100 ppmS at 500 and 800 °C are denoted in Figure 3-5b. According to the calculated phase diagram, both Rh and  $Rh_1Ni_2$  will have a coverage of at least  $1/3$  ML at 500 °C, but the sulfur coverage of  $Rh_1Ni_2(111)$  will be less than Rh(111) in the range from 4 to 33 ppmS at 800 °C. Strohm et al.’s experimental results, suggesting higher S tolerance of Rh-Ni binary catalysts at 500 °C, cannot be exactly explained by this phase diagram. If the transition from  $1/4$  to  $1/3$  ML is considered, the boundary toward  $1/3$  ML on  $Rh_1Ni_2(111)$  would be lowered as shown on pure Rh or Ni metals in Figure S1, however, this transition cannot be modeled on  $Rh_1Ni_2(111)$  because  $1/4$  ML coverage cannot be designed with the Rh:Ni ratio of 1:2. Thus, a sulfur coverage difference between Rh and  $Rh_1Ni_2$  at 500 °C may be more subtle or reflect differences attributed to surface facets other than (111). Despite limitations in modeling the complex experimental system, our results show that a Rh-Ni binary catalyst has a lower equilibrium sulfur coverage than a Rh catalyst at various temperatures and  $H_2S$  pressures.

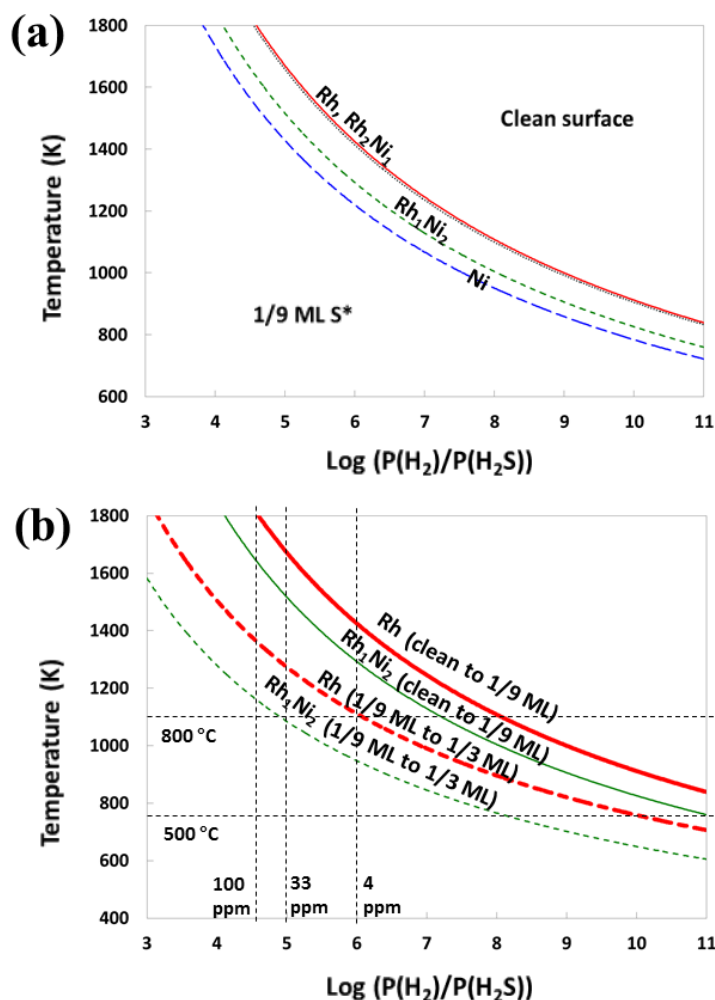


Figure 3-5. (a) Phase diagram of 1/9 ML to “clean surface” transition of Rh (solid line, red), Ni (long-dashed line, blue),  $\text{Rh}_1\text{Ni}_2$  (short-dashed line, green), and  $\text{Rh}_2\text{Ni}_1$  (dotted line, black) (111) surfaces. (b) Phase diagram of Rh (thick solid and short-dashed lines, red) and  $\text{Rh}_1\text{Ni}_2$  (thin solid and short-dashed lines, green) at various sulfur coverages with an indication of the experimental conditions studied by Strohm et al [6]. (clean to 1/9 ML S coverage: solid line, 1/9 to 1/3 ML S coverage: dashed line).

### 3.3.4 Rh(221) stepped surfaces and $\text{Rh}_4/\text{CeO}_2(111)$ .

The phase diagrams discussed in the preceding sections demonstrate  $\text{S}^*$  adsorption is more stable than  $\text{SO}_x^*$  on the Rh(111) surface under reforming conditions. As previous XANES results suggest  $\text{SO}_4$  formation on Rh catalysts following reforming, we further considered the role of surface steps and

support interactions to explain this discrepancy. We also examined whether exposure to higher oxygen pressures could motivate sulfate formation, as XANES experiments were performed ex-situ, likely with brief atmospheric exposure. To include the influence of high oxygen pressure, we made an extreme assumption that all  $\text{H}_2\text{O}$  present would be converted into  $\text{O}_2$ , and therefore used an equilibrium  $\text{O}_2$  gas pressure of 0.17 atm to consider production of  $\text{SO}_x^*$  and  $\text{H}_2$  by reacting with  $\text{H}_2\text{S}$  gas. Figure 3-6 shows that the  $\text{SO}_4$  species becomes the most stable adsorbate on the Rh(111) and Ni(111) surfaces upon exposure to a  $P(\text{O}_2)$  of 0.17 atm at 500 K or 1000K. This is in a good agreement with Nomoto et al.'s results<sup>27</sup> which demonstrated that adsorbed S atoms on Rh(100) desorb as  $\text{SO}_x$  species by reacting with an  $\text{O}_2$  environment, though S atoms stay on the surface under a  $\text{H}_2\text{O}$  environment. Though exposure of surfaces to atmospheric oxygen could explain sulfate formation, it does not explain the observed difference in XANES studies that sulfate formation occurs on a Rh catalyst but not on a Ni catalyst. Our calculations indicate that both metals have a preference to  $\text{SO}_4$  adsorption under atmospheric  $\text{O}_2$  pressure.

One possible cause of the experimental difference in sulfide formation is differences in Rh and Ni particle size. The Rh particle size may be expected to be smaller than Ni because Rh, as a noble metal, is more resistant to sintering.<sup>16</sup> A smaller catalyst particle has a higher fraction of stepped surfaces than a larger one, so Gibbs free energy changes of S and  $\text{SO}_4$  adsorption on the Rh and Ni stepped surfaces (modeled as (221) surfaces) have been compared at 1000 K using Eq. 6. The most stable configurations of S and  $\text{SO}_4$  adsorption were determined by comparing step-bottom and step-top sites. A sulfur atom preferentially adsorbs at the step-bottom site for Ni and at the step-top site for Rh, though the difference in energy in either case is minimal. A sulfate molecule optimally adsorbs at the step-top site for both Rh and Ni, as presented in Figure 3-7. The adsorbate formation energies, calculated via Eq. 6 under the condition of  $P(\text{H}_2\text{S})=3.24 \times 10^{-6}$  atm and 1000 K, on the flat and stepped surfaces are listed in Table 3-2. Even though  $\text{SO}_4^*$  adsorption on the Rh(221) surface is stronger than on Rh(111), its formation is endothermic as opposed to exothermic S formation on the Rh(221) surface. Ni also shows the same

tendency as Rh. Thus, the different fraction of surface step sites between Rh and Ni does not explain the different preference, observed in experimental XANES studies for sulfate formation.

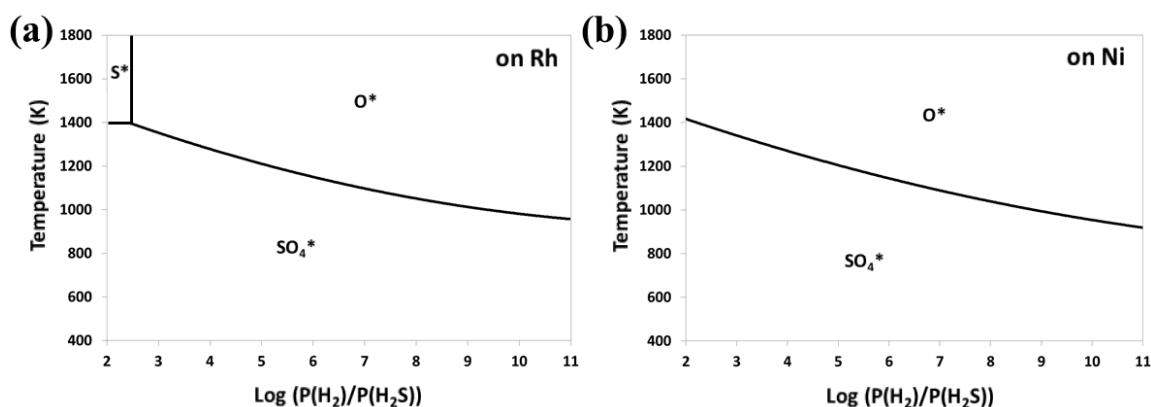


Figure 3-6. Phase diagrams of considering S\*, O\*, and SO<sub>x</sub>\* adsorption on (a) Rh(111) and (b) Ni(111) surfaces at various temperatures under a high O<sub>2</sub> pressure (P(O<sub>2</sub>) = 0.17 atm). Other gas pressures used here were calculated based on Eq. 2: P(H<sub>2</sub>)=0.629~0.634 atm, P(CH<sub>4</sub>)=0.0768~0.0774 atm, P(CO<sub>2</sub>)=0.0959~0.0968 atm, P(CO)=0.0192~0.0194 atm, P(H<sub>2</sub>S)=8.86×10<sup>-3</sup>~1.49×10<sup>-11</sup> atm.

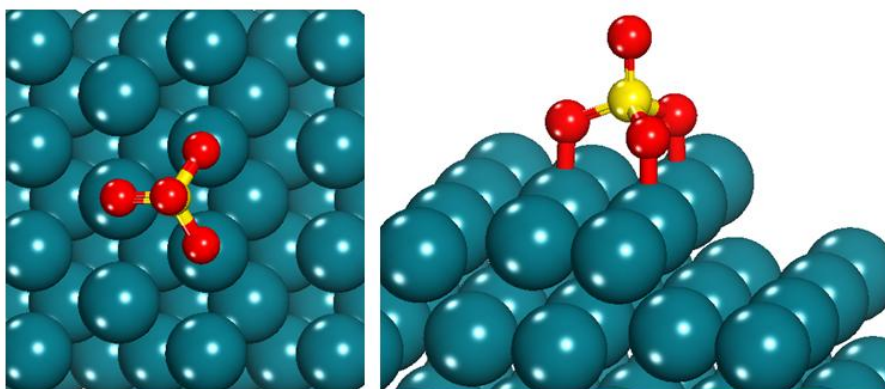


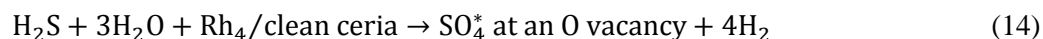
Figure 3-7. DFT optimized structures of SO<sub>4</sub> adsorbed at the step-top site of the Rh(221) surface.

Table 3-2. Gibbs free energy changes (eV) of S and SO<sub>4</sub> adsorption from H<sub>2</sub>S and H<sub>2</sub>O gases on Rh and Ni (111) and (221) surfaces as well as a Rh cluster on the ceria surface. All free energies were calculated at 1000 K and gas pressures of P(H<sub>2</sub>O)=0.42 atm, P(H<sub>2</sub>)=0.35 atm, P(CH<sub>4</sub>)=0.09 atm, P(CO<sub>2</sub>)=0.12 atm, P(CO)=0.02 atm, and P(H<sub>2</sub>S)=3.24×10<sup>-6</sup> atm.

	Rh (111)	Rh (221)	Ni (111)	Ni (221)	Rh <sub>4</sub> on CeO <sub>2</sub>	Rh <sub>4</sub> on CeO <sub>2</sub> with an O vacancy
S	-0.61	-0.67	-0.33	-0.70	-0.99	-1.49
SO <sub>4</sub>	5.11	4.76	4.97	4.53	4.38	2.51

Interaction of Rh clusters with the support may motivate SO<sub>4</sub> formation, possibly through support induced modification of Rh chemical behavior or formation of SO<sub>x</sub> species at the metal-support boundary. The interaction between ceria and supported Rh particles has been modeled by computing the S and SO<sub>4</sub> adsorption energies on a Rh<sub>4</sub> cluster on the CeO<sub>2</sub>(111) surface (denoted as Rh<sub>4</sub>/ceria). We examined two sulfur adsorption sites including sulfur interacting with the Rh<sub>4</sub> cluster and binding at the interface between the Rh<sub>4</sub> cluster and ceria surface. The sulfur atom prefers adsorption to the hollow site exposed by the Rh<sub>4</sub> cluster as shown in Figure 3-8a. The favorable site for SO<sub>4</sub> adsorption is presented in Figure 3-8b. The comparison in adsorption free energy change between S and SO<sub>4</sub> is added to Table 3-2 and the result also indicates a preference for S\* formation rather than SO<sub>4</sub>\* formation for supported Rh<sub>4</sub> clusters.

We also considered if O vacancies over the metal-support interface could motivate SO<sub>4</sub> formation.<sup>47,54</sup> The preferred adsorption configuration (Figure 3-8c) was determined by forming an O vacancy at two different locations near to the Rh<sub>4</sub> cluster. The SO<sub>4</sub> molecule is adsorbed with one O atom filling the oxygen vacancy site and the other two interacting with the Rh<sub>4</sub> cluster. The free energy of SO<sub>4</sub> formation at the Rh<sub>4</sub>/vacancy site is calculated considering the reaction energy for





The free energy for this reaction is compared with other surface models in Table 3-2 and Figure 3-9. The formation of  $\text{SO}_4$  at the  $\text{Rh}_4/\text{vacancy}$  site is favorable compared with  $\text{SO}_4$  formation directly on the  $\text{Rh}_4/\text{CeO}_2(111)$  supported cluster. The adsorption free energy, however, is endergonic and less favorable than  $\text{S}^*$  formation on the  $\text{Rh}_4/\text{ceria}$  surface or the  $\text{Rh}(111)$  surface. The most stable adsorption occurs through the S adsorption to the  $\text{Rh}_4/\text{vacancy}$  surface. The optimal adsorption site has S bound to the  $\text{Rh}_4$  cluster, with the O vacancy nearby causing an electronic effect that strengthens the S- $\text{Rh}_4$  interaction.

We also note that the bulk phase diagram of ceria, experimentally constructed by Ferrizz et al.,<sup>55</sup> also suggests that reduced ceria is stable relative to a ceria oxysulfide or ceria sulfate under reforming conditions. Because the bulk phase diagram of ceria is plotted based on  $\text{P}(\text{O}_2)$  and  $\text{P}(\text{S}_2)$ , we calculated those pressures from the reforming  $\text{P}(\text{H}_2\text{O})$  and  $\text{P}(\text{H}_2\text{S})$  at 900 K and 1000 K using Gibbs free reaction energies of the following reaction equations from thermodynamic tables<sup>54</sup>



With this analysis, reforming conditions are firmly located in the  $\text{CeO}_{2-x}$  phase of the Ce-O-S phase diagram, indicating that there is no transition to formation for the ceria oxysulfide under reforming conditions.

In summary, DFT calculations and *ab initio* thermodynamics considerations indicate that only  $\text{S}^*$  or bulk metal sulfide formation is favorable under a reforming atmosphere. The  $\text{S}^*$  coverage or formation of bulk sulfide is determined by the  $\text{H}_2\text{S}$  pressure and temperature. Exposure to a more oxidizing atmosphere is necessary for formation of  $\text{SO}_x$  ( $x=1\sim4$ ) species, with  $\text{SO}_4^*$  formation favorable under atmospheric oxygen pressures. The discrepancy with experimental results<sup>15,26</sup> may be due to unanticipated oxygen exposure in the experimental studies or factors not considered in our DFT analysis. We did not consider co-adsorption of  $\text{SO}_x$  species with hydrocarbon fragments, the formation of S-containing

hydrocarbons, or allow for more extensive surface reconstruction. Additionally, the DFT results presented consider only the thermodynamically stable species and not the kinetics of processes that would generate these species. Despite these limitations, the reported results are useful in demonstrating that if  $\text{SO}_x$  surface species are formed under reforming conditions, the mechanistic cause is more complex than a simple thermodynamic driving force for their formation on the surface models we considered.

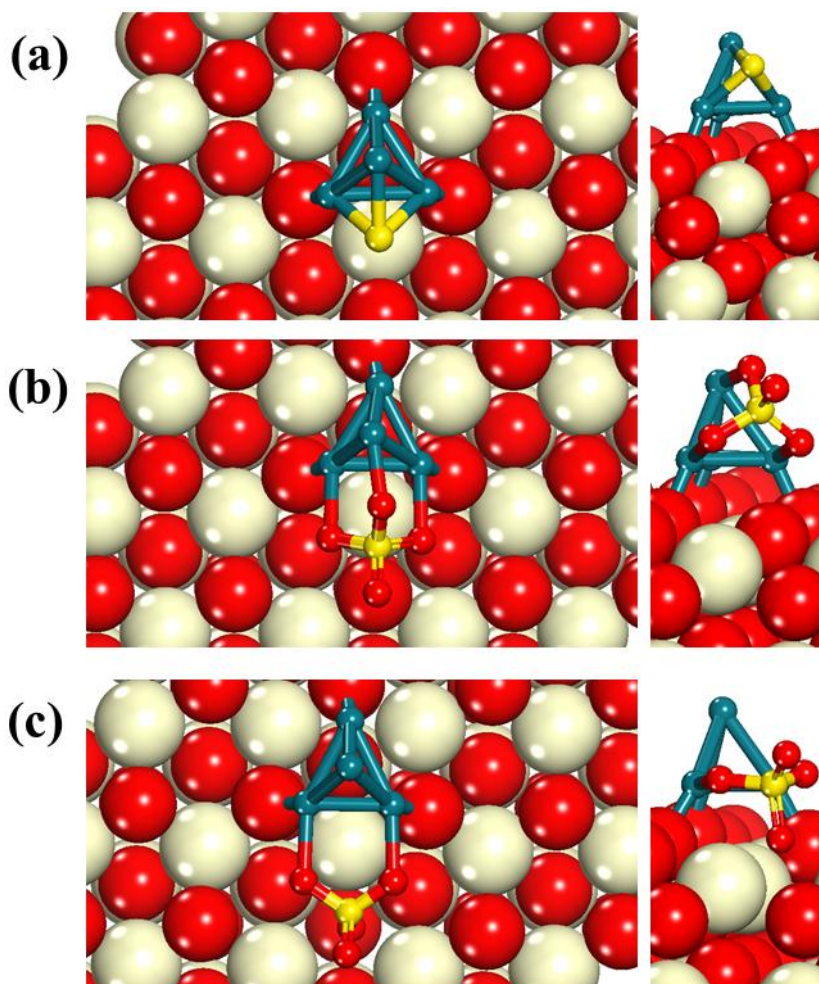


Figure 3-8. DFT optimized structures for adsorption of (a) S and (b)  $\text{SO}_4$  on a  $\text{Rh}_4$  cluster on the  $\text{CeO}_2(111)$  surface and (c) adsorption of  $\text{SO}_4$  on a  $\text{Rh}_4$  cluster on the  $\text{CeO}_2(111)$  surface with an O vacancy

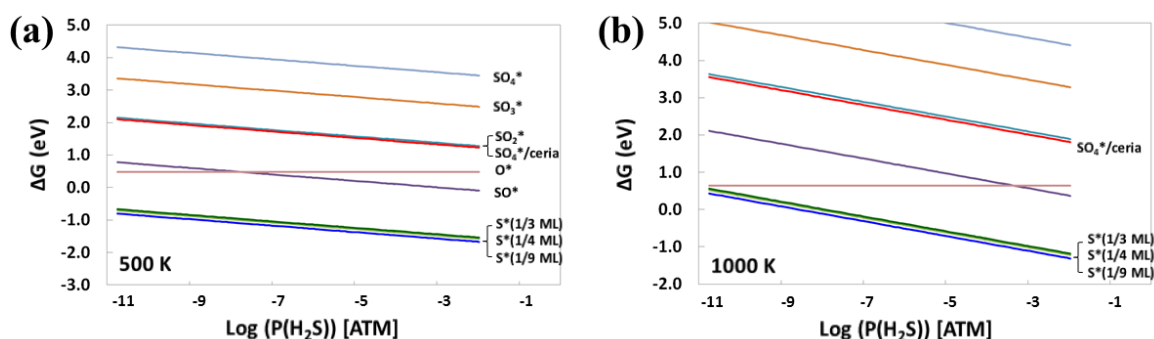


Figure 3-9. Phase diagrams of Rh flat surface and a  $\text{Rh}_4$  cluster on ceria surface with an oxygen vacancy at (a) 500 K and (b) 1000 K. S adsorption on the Rh flat surface included various sulfur coverages such as 1/3, 1/4, and 1/9 ML. The gas pressures used here are the same with those of Figure 3-3.

### 3.4 Conclusions

Sulfur poisoning under the reforming conditions was studied using density functional theory and *ab initio* thermodynamics to construct surface phase diagrams. S or  $\text{SO}_x$  adsorption, O adsorption, and metal sulfide formation were considered on the (111) surfaces of Rh, Ni,  $\text{Rh}_1\text{Ni}_2$ ,  $\text{Rh}_2\text{Ni}_1$ , the (221) surfaces of Rh and Ni, and a  $\text{Rh}_4$  particle on the  $\text{CeO}_2(111)$  surface. Under the steam reforming environment, atomic  $\text{S}^*$  adsorption is preferred, with bulk metal sulfide formation favorable at temperatures below 500 K. This trend is not altered by introducing high  $\text{H}_2\text{O}$  pressures and is more sensitive to the change of  $P(\text{H}_2\text{S})$  than  $P(\text{H}_2\text{O})$  due to the lower equilibrium constant for conversion of  $\text{H}_2\text{O}$  to  $\text{O}_2$ . The lower binding energy of S on Ni leads to a S-free surface area at lower temperatures and higher  $\text{H}_2\text{S}$  pressures than for the Rh surface. This is consistent with the greater sensitivity to S poisoning observed experimentally for Rh catalysts. Predicted  $\text{S}^*$  coverages indicate that  $\text{Rh}_1\text{Ni}_2$  shows higher sulfur tolerance than pure Rh or  $\text{Rh}_2\text{Ni}_1$ .  $\text{Rh}_1\text{Ni}_2$  experiences a phase transition from a 1/3 ML coverage to a 1/9 coverage at 800 °C and less than 33 ppmS, whereas Rh remains at a 1/3 ML sulfur coverage. Binary

Rh-Ni metals may exhibit a greater sulfur tolerance due to a lower equilibrium coverage of  $S^*$  under reforming conditions.

The preference of Rh for  $SO_4^*$  or  $S^*$  formation were investigated with stepped surfaces and a Rh cluster on the  $CeO_2(111)$  surface. The phase diagrams under the reforming conditions show that there is no preference for  $SO_4^*$  formation on all the surfaces considered in this study. With a high  $P(O_2)$ ,  $SO_4^*$  is preferred over  $S^*$  on both Rh and Ni.

### 3.5 References

- (1) Bockris, J. O. *Int J Hydrogen Energ* **2008**, 33, 2129.
- (2) Armor, J. N. *Appl Catal a-Gen* **1999**, 176, 159.
- (3) Rostrup-Nielsen, J. R. *Phys Chem Chem Phys* **2001**, 3, 283.
- (4) Song, C. S. *Catal Today* **2002**, 77, 17.
- (5) Kugai, J.; Velu, S.; Song, C. S. *Catal Lett* **2005**, 101, 255.
- (6) Zheng, J.; Strohm, J. J.; Song, C. *Fuel Process Technol* **2008**, 89, 440.
- (7) Sehested, J. *Catal Today* **2006**, 111, 103.
- (8) Farrauto, R.; Hwang, S.; Shore, L.; Ruettinger, W.; Lampert, J.; Giroux, T.; Liu, Y.; Ilinich, O. *Annu Rev Mater Res* **2003**, 33, 1.
- (9) Bu, J.; Loh, G.; Gwie, C. G.; Dewiyanti, S.; Tasrif, M.; Borgna, A. *Chem Eng J* **2011**, 166, 207.
- (10) Arias, M.; Laurenti, D.; Geantet, C.; Vrinat, M.; Hideyuki, I.; Yoshimura, Y. *Catal Today* **2008**, 130, 190.
- (11) Selvavathi, V.; Chidambaram, V.; Meenalkshisundaram, A.; Sairam, B.; Sivasankar, B. *Catal Today* **2009**, 141, 99.
- (12) Holladay, J. D.; Hu, J.; King, D. L.; Wang, Y. *Catal Today* **2009**, 139, 244.

- (13) Strohm, J. J.; Zheng, J.; Song, C. S. *J Catal* **2006**, 238, 309.
- (14) Lee, K.; Song, C. S.; Janik, M. J. *Appl Catal a-Gen* **2010**, 389, 122.
- (15) Chen, Y. S.; Xie, C.; Li, Y.; Song, C. S.; Bolin, T. B. *Phys Chem Chem Phys* **2010**, 12, 5707.
- (16) Lakhapatri, S. L.; Abraham, M. A. *Appl Catal a-Gen* **2009**, 364, 113.
- (17) Cheekatamarla, P. K.; Lane, A. M. *J Power Sources* **2005**, 152, 256.
- (18) Wang, J. H.; Liu, M. L. *Electrochem Commun* **2007**, 9, 2212.
- (19) Rosenqvist, T. *J Iron Steel I* **1954**, 176, 37.
- (20) Barbouth, N.; Oudar, J. *Cr Acad Sci C Chim* **1969**, 269, 1618.
- (21) Massalski, T. B.; Okamoto, H.; ASM International. *Binary alloy phase diagrams*; 2nd ed.; ASM International: Materials Park, Ohio, 1990.
- (22) Janik, M. J.; Guo, J. H.; Xie, C.; Lee, K. T.; Guo, N.; Miller, J. T.; Song, C. S. *Acs Catal* **2011**, 1, 574.
- (23) Bartholomew, C. H. *Appl Catal a-Gen* **2001**, 212, 17.
- (24) Rodriguez, J. A. *Prog Surf Sci* **2006**, 81, 141.
- (25) Kuhn, J. N.; Lakshminarayanan, N.; Ozkan, U. S. *J Mol Catal a-Chem* **2008**, 282, 9.
- (26) Xie, C.; Chen, Y. S.; Li, Y.; Wang, X. X.; Song, C. S. *Appl Catal a-Gen* **2010**, 390, 210.
- (27) Nomoto, T.; Miura, K.; Yagi, S.; Kutluk, G.; Sumida, H.; Soda, K.; Hashimoto, E.; Namatame, H.; Taniguchi, M. *Surf Sci* **2007**, 601, 3784.
- (28) Yagi, S.; Nomoto, T.; Kutluk, G.; Sumida, H.; Namatame, H.; Taniguchi, M.; Soda, K. *Rev Adv Mater Sci* **2005**, 10, 277.
- (29) Nomoto, T.; Sumi, O.; Yagi, S.; Soda, K.; Namatame, H.; Taniguchi, M. *Surf Interface Anal* **2008**, 40, 391.
- (30) Kresse, G.; Furthmuller, J. *Computational Materials Science* **1996**, 6, 15.
- (31) Kresse, G.; Furthmuller, J. *Physical Review B* **1996**, 54, 11169.
- (32) Kresse, G.; Hafner, J. *Physical Review B* **1993**, 47, 558.

- (33) Blochl, P. E. *Physical Review B* **1994**, *50*, 17953.
- (34) Perdew, J. P.; Burke, K.; Ernzerhof, M. *Physical Review Letters* **1996**, *77*, 3865.
- (35) Perdew, J. P.; Chevary, J. A.; Vosko, S. H.; Jackson, K. A.; Pederson, M. R.; Singh, D. J.; Fiolhais, C. *Physical Review B* **1992**, *46*, 6671.
- (36) Fabris, S.; de Gironcoli, S.; Baroni, S.; Vicario, G.; Balducci, G. *Physical Review B* **2005**, *72*.
- (37) Fabris, S.; de Gironcoli, S.; Baroni, S.; Vicario, G.; Balducci, G. *Physical Review B* **2005**, *71*.
- (38) Kresse, G.; Blaha, P.; Da Silva, J. L. F.; Ganduglia-Pirovano, M. V. *Physical Review B* **2005**, *72*.
- (39) Knapp, D.; Ziegler, T. *J Phys Chem C* **2008**, *112*, 17311.
- (40) Nolan, M.; Grigoleit, S.; Sayle, D. C.; Parker, S. C.; Watson, G. W. *Surf Sci* **2005**, *576*, 217.
- (41) Yang, Z.; Zhansheng, L. A.; Luo, G.; Hermansson, K. *Phys Lett A* **2007**, *369*, 132.
- (42) Donnay, J. D. H.; Ondik, H. M.; United States. National Bureau of Standards. *Crystal data; determinative tables*; 3d ed.; National Bureau of Standards: Washington, 1972.
- (43) Wyckoff, R. W. G. *Crystal structures*; R.E. Krieger Pub. Co.: Malabar, Fla., 1982.
- (44) Wang, J. H.; Cheng, Z.; Bredas, J. L.; Liu, M. L. *J Chem Phys* **2007**, *127*.
- (45) Naren, H. R.; Thamizhavel, A.; Nigam, A. K.; Ramakrishnan, S. *Physical Review Letters* **2008**, *100*.
- (46) Monkhorst, H. J.; Pack, J. D. *Physical Review B* **1976**, *13*, 5188.
- (47) Mayernick, A. D.; Janik, M. J. *J Phys Chem C* **2008**, *112*, 14955.
- (48) Lu, Z. S.; Yang, Z. X. *J Phys-Condens Mat* **2010**, *22*.
- (49) Hill, T. L. *An introduction to statistical thermodynamics*; Dover Publications: New York, 1986.
- (50) Baker, B. G. *J Chem Phys* **1966**, *45*, 2694.
- (51) Matsuzaki, Y.; Yasuda, I. *Solid State Ionics* **2000**, *132*, 261.
- (52) Duan, Y. H.; Sorescu, D. C. *J Chem Phys* **2010**, *133*.
- (53) Fultz, B. *Prog Mater Sci* **2010**, *55*, 247.
- (54) Mayernick, A. D.; Janik, M. J. *J Catal* **2011**, *278*, 16.

- (55) Fertizz, R. M.; Gorte, R. J.; Vohs, J. M. *Appl Catal B-Environ* **2003**, *43*, 273.

### 3.6 Supporting Information

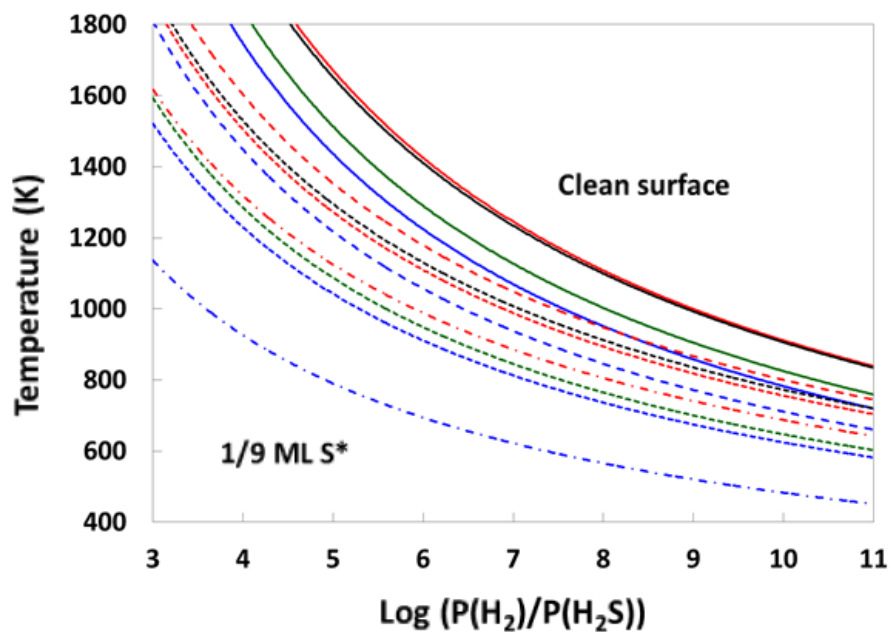


Figure S1. Phase diagram of Rh (red), Ni (blue),  $\text{Rh}_1\text{Ni}_2$  (green), and  $\text{Rh}_2\text{Ni}_1$  (black) at various sulfur coverages (clean to 1/9 ML S coverage: solid line, 1/9 to 1/4 ML S coverage: long-dashed line, 1/9 to 1/3 ML S coverage: short-dashed line, 1/4 to 1/3 ML S coverage: long-dashed line together with dots)

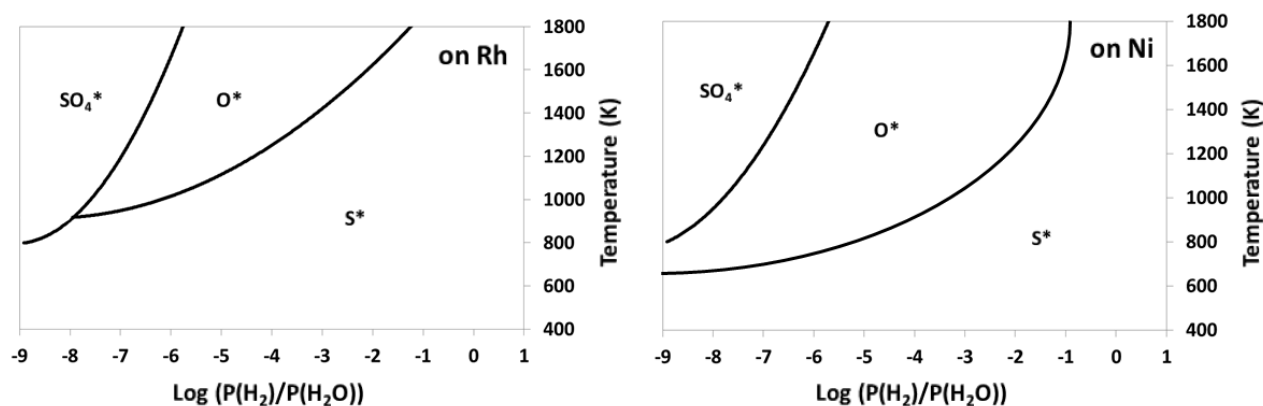


Figure S2. Phase diagrams of considering  $\text{S}^*$ ,  $\text{O}^*$ , and  $\text{SO}_x^*$  adsorption on (a) Rh(111) and (b) Ni(111) surfaces at various temperatures as a function of  $P(\text{H}_2)/P(\text{H}_2\text{O})$  ratio. Gas pressures used here were calculated based on Eq. 2 by changing the  $P(\text{H}_2\text{O})$  from 0.11 atm to almost 1 atm.



Table S1. The formation Gibbs free energies (unit: eV) of SO, SO<sub>2</sub>, SO<sub>3</sub>, and H<sub>2</sub>SO<sub>4</sub> from H<sub>2</sub>S and H<sub>2</sub>O gases calculated using Eq. 3 and experimental thermodynamic tables provided by NIST (National Institute of Standards and Technology)

	$\Delta G$ by Eq. 3	$\Delta G$ by NIST data
SO	2.50	2.35
SO <sub>2</sub>	1.97	1.79
SO <sub>3</sub>	3.61	3.40
H <sub>2</sub> SO <sub>4</sub>	3.05	3.10

Table S2. The number of surface metal atoms and adsorbed sulfur atoms for each sulfur coverage in Eq. 11, 12, and 13. (LHS and RHS indicate the left-hand side and the right-hand side of an equation, respectively.)

coverage	$\theta=1/9$			$\theta=1/4$			$\theta=1/3$		
	unit cell	LHS of Eq. 11	LHS of Eq. 12	unit cell	RHS of Eq. 11	LHS of Eq. 13	unit cell	RHS of Eq. 12	RHS of Eq. 13
the number of surface metal atoms	9	$4 \times 9$ =36	$1 \times 9$ =9	4	$9 \times 4$ =36	$3 \times 4$ =12	3	$3 \times 3$ =9	$4 \times 3$ =12
the number of adsorbed sulfur atoms	1	$4 \times 1$ =4	$1 \times 1$ =1	1	$9 \times 1$ =9	$3 \times 1$ =3	1	$3 \times 1$ =3	$4 \times 1$ =4

## Chapter 4

### **Density functional theory study of propane steam reforming on Rh-Ni binary metals: Sulfur tolerance and scaling/ Brønsted-Evans-Polanyi relations**

ABSTRACT: Enhanced sulfur tolerance on binary Rh-Ni metals is examined for the propane steam reforming process on close packed metal surfaces of Rh, Ni,  $\text{Rh}_1\text{Ni}_2$ , and  $\text{Rh}_2\text{Ni}_1$  with and without co-adsorbed S atoms. To reduce computational cost, scaling and Brønsted-Evans-Polanyi (BEP) correlations are constructed from density functional theory (DFT) methods. The combined use of these methods produces significant errors among these similar metal surfaces, however, BEP relationships applied within reaction types are reliable across Rh, Ni, and binary Rh-Ni surfaces with and without co-adsorbed S atoms. The potential energy surface of propane steam reforming, estimated using the BEP correlations, shows that the C-C cleavages of  $\text{CHC}^*$ ,  $\text{CH}_3\text{CC}^*$  and  $\text{CH}_2\text{C}^*$  along with the O addition to  $\text{CH}^*$  are kinetically significant elementary steps. Three of these steps show only slight barrier increases with co-adsorbed S on the  $\text{Rh}_2\text{Ni}_1$  surface, suggesting an energetic explanation for enhanced S tolerance. The average poisoning effect by the presence of co-adsorbed sulfur for bond breaking was minimized on binary Rh-Ni metals, suggesting a high sulfur resistance can be induced using a bimetallic formulation of Rh and Ni.

## 4.1 Introduction

With the increasing demand to increase energy efficiency, hydrogen has drawn interest as an efficient and environmentally friendly energy carrier. The principal methods for hydrogen production are water electrolysis, partial oxidation of heavy oil or coal, and steam reforming of hydrocarbons.<sup>1</sup> Currently, methane steam reforming is used for most industrial hydrogen production.<sup>2</sup> One of the major potential applications of hydrogen is as a fuel for proton membrane exchange fuel cells (PEMFC) and solid oxide fuel cells (SOFC).<sup>3</sup> A steam reforming unit can be combined with fuel cells for on-board and on-site electricity supply where liquid hydrocarbon fuels such as diesel or jet fuels are practical due to high energy density, safety, handling, and established infrastructures. There are four major challenges to efficient hydrocarbon reforming: insufficient catalytic activity, sulfur poisoning, carbon deposition, and catalyst particle sintering.<sup>4</sup> Sulfur poisoning is a critical issue because liquid hydrocarbon fuels inherently contain a ppm level of sulfur species and a ppb level after a desulfurization process.<sup>4,5</sup> The catalysts poisoned by sulfur species in fuels lose activity and form carbon deposits blocking the catalyst surface.<sup>6</sup> Herein, we examine the reforming mechanism, using propane as a model fuel, in the presence of co-adsorbed sulfur with density functional theory (DFT). Rh-Ni bimetallic catalysts are determined to minimize the S-poisoning effects compared to their monometallic components.

The weak resistance of catalysts to sulfur poisoning can be enhanced by using a binary metal structure. The combination of Rh and Ni for the steam reforming process has been shown to exhibit lower formation of carbon deposits than the pure metal catalysts and a low-cost process by mixing noble Rh with non-noble Ni.<sup>7-9</sup> The addition of Ni to Rh catalysts supported on  $\text{CeO}_2\text{-Al}_2\text{O}_3$  enhanced sulfur resistance with the best longevity from a 2wt% Rh-10wt% Ni (Ni:Rh atomic ratio of 1:0.1) catalyst.<sup>10</sup> CO dissociation is a sensitive reaction step in perceiving the sulfur poisoning level in the reforming reaction. Using density functional theory (DFT), the Rh-Ni bimetallic system was shown to better maintain activity for CO dissociation in the presence of co-adsorbed S atoms.<sup>11</sup> The binary Rh-Ni (111) surfaces showed

weaker sulfur binding and the highest CO dissociation rate with sulfur co-adsorbed compared to pure metals. Charge density analysis identified a reduced interaction between S and CO on the Rh-Ni binary metal.

The main sulfur containing compounds in jet or diesel fuels are benzothiophene derivatives<sup>12</sup> which are decomposed to H<sub>2</sub>S in a reducing atmosphere such as in the steam reforming process.<sup>13</sup> The H<sub>2</sub>S gas may be converted into a variety of sulfur species on a catalyst surface to become an actual sulfur poisoning species. We previously examined possible sulfur poisoning surface species such as metal sulfides, adsorbed S atoms, and adsorbed SO<sub>x</sub> (x=1~4) species using ab initio thermodynamic calculations and concluded that adsorbed S atoms are the sulfur poisoning species under actual steam reforming temperatures and pressures.<sup>14</sup> This result justifies our consideration of S\* as the poisoning species herein. Collectively, our previous work suggests that the Rh-Ni binary metals can reduce sulfur coverage and make elementary reactions more sulfur resistant due to the reduced interaction between S\* and adsorbates.

Though the effect of S\* on CO dissociation energetics was established, the steam reforming process of long-chain hydrocarbons contains numerous elementary steps<sup>15</sup> and CO dissociation is unlikely to be rate determining. In this study, we examine the impact of S\* on the full reaction path of propane steam reforming over Rh, Ni, Rh<sub>2</sub>Ni<sub>1</sub>, and Rh<sub>1</sub>Ni<sub>2</sub> (111) surfaces. Choosing propane as a model fuel enables us to both save computational cost and include a secondary carbon atom, thereby including the relevant C-C, C-H, and C-O bond breaking and forming reactions. Previous computational studies of steam reforming have been limited to C1, C2 hydrocarbons or alcohols.<sup>16-18</sup> Our results can provide insight into S tolerance within other catalytic reactions such as biomass reforming and the reverse reaction of reforming, Fischer-Tropsch synthesis, because these processes also involve C-H, C-O, and C-C bond breaking and formation.

Though consideration of propane reforming rather than longer chain hydrocarbons reduces the reaction complexity, propane reforming contains an enormous number of possible elementary steps. We can reduce computational cost by using Brønsted-Evans-Polanyi (BEP) and scaling relationships. BEP

relationships allow for facile estimation of the maxima of potential energy surfaces along a reaction path by linearly correlating the activation barrier with the reaction energy (traditional BEP) or the transition state energy with the initial or final state energy (non-traditional BEP).<sup>19-22</sup> Applying BEP relationships across similar reactions (C-H dissociation) or across catalyst materials limits the number of activation barriers to calculate with DFT methods. The minima of potential energy surfaces can be estimated by scaling relations that correlate molecular binding energies with atomic binding energies.<sup>22-26</sup> The entire potential energy surface of propane reforming can be mapped out by combining BEP and scaling relations. Most previous studies using scaling and BEP relationships have constructed these relations across a wide range of pure transition metals and estimated reaction energetics with data points scattered over 1 eV from a linear line.<sup>27-30</sup> Thus, the reliability of the combined use of BEP and scaling relationships across a series of similar metal surfaces, such as our system ranging from pure Rh and Ni to binary  $\text{Rh}_1\text{Ni}_2$  and  $\text{Rh}_2\text{Ni}_1$ , is not established. In this study, we address this issue by comparing the combined use of scaling and BEP relations with the use of BEP relations only.

The preferred reaction path of propane reforming is investigated with the aid of previous literature. A general picture of significant bond forming and breaking steps in the steam reforming process together with the preferred reaction path of C1 intermediates is obtained by referring to Blaylock et al.'s DFT study of methane steam reforming on Ni(111).<sup>31</sup> The preferred reaction path of C2 intermediates is selected based on a previous study of dehydrogenation and hydrogenolysis of ethane on Pt(111).<sup>32</sup> The reaction path and adsorption configurations of C3 intermediates ranging from propane adsorption to C-C breaking is based on the preferred path of propane dehydrogenation on Pt(111).<sup>33,34</sup> These previous studies allow us to limit the set of elementary reactions considered.

Herein, we evaluate the scaling and BEP relations in terms of prediction accuracy for the similar Rh, Ni,  $\text{Rh}_1\text{Ni}_2$ , and  $\text{Rh}_2\text{Ni}_1$  (111) surfaces and apply them for the construction of the reaction energy profile of propane steam reforming. From the estimated reaction energetics of propane reforming, we identify key elementary steps and examine the impact of co-adsorbed S on these steps by comparing pure

Rh and Ni metals with binary Rh-Ni metals to determine the elementary mechanism through which binary Rh-Ni metals provide higher sulfur resistance.

## 4.2 Methods

### 4.2.1 Computational methods

Calculations were carried out using the Vienna Ab-Initio Simulation Program (VASP), an ab initio total-energy and molecular dynamics program developed at the Institute for Material Physics at the University of Vienna.<sup>35-37</sup> Exchange and correlation energies were incorporated by the Perdew-Wang (PW91) version of the generalized gradient approximation (GGA).<sup>38,39</sup> The electron-ion interactions are described by the projector augmented wave (PAW) method by Blöchl.<sup>40</sup> The cutoff energy of the plane-wave basis set applied to represent valence electrons was 400 eV. Isolated molecules were optimized in a  $15 \times 15 \times 15$  Å unit cell where only the gamma point was used for k-point sampling. All calculations including Ni atoms and an isolated sulfur atom were spin polarized. Structural optimization was conducted by minimizing the forces on all atoms to less than  $0.05 \text{ eV} \cdot \text{Å}^{-1}$ , with testing versus a criterion of  $0.02 \text{ eV} \cdot \text{Å}^{-1}$  showing no significant difference in energy or structure.

The optimized lattice parameters for bulk Rh and Ni are 3.80 and 3.52 Å, which only deviate by 0.08 % and 0.11 % from the experimental values.<sup>41</sup> The Rh-Ni binary metal was modeled by evenly distributing Rh and Ni atoms in the structure, where the optimized lattice parameters are 3.66 Å for  $\text{Rh}_1\text{Ni}_2$  and 3.76 Å for  $\text{Rh}_2\text{Ni}_1$ . Our previous DFT study showed that the formation of these two bimetallic phases from the constituent pure metals is thermodynamically favorable over 100 °C.<sup>42</sup> The bimetallic structural formation of Rh-Ni catalysts was experimentally verified by temperature-programmed reduction (TPR) and X-ray photoelectron spectroscopy (XPS) analyses.<sup>10</sup> The surfaces of Rh, Ni,  $\text{Rh}_1\text{Ni}_2$ , and  $\text{Rh}_2\text{Ni}_1$  were terminated by the (111) facet with  $3 \times 3$  cell size and a vacuum region of 15 Å normal to

the surface. All the surfaces are composed of a total of five layers with the top three layers relaxed, and reciprocal space was sampled with a  $5 \times 5 \times 1$  gamma centered k-point grid. Transition states were determined using the climbing image nudged elastic band (CI-NEB) method.<sup>43-45</sup> For the application of the CI-NEB, four images are interpolated between the initial and final states and optimized along the reaction coordinate. The transition state was confirmed as the image with the maximum energy value, an imaginary vibrational frequency, and an absolute force tangential to the reaction coordinate below  $0.05 \text{ eV \AA}^{-1}$ .

#### 4.2.2 Scaling and BEP relations

Equilibrium state energies can be estimated using scaling relations which relate atomic binding energies with molecular binding energies. We classify two types of molecular adsorbates along the path of propane reforming, mono-dentate adsorbates and bi-dentate adsorbates; different scaling relations are used for each type. The scaling relation for a mono-dentate adsorbate is expressed as<sup>24</sup>

$$\Delta E(AH_x) = \gamma(x)\Delta E(A) + \xi \quad (1)$$

where

$$\gamma(x) = \frac{x_{max}-x}{x_{max}} \quad (2)$$

$\Delta E(AH_x)$  represents the binding energy of species  $AH_x$  to the surface,  $\Delta E(A)$  represents the atomic binding energy of species A (i.e., C, O) to the surface, and  $x_{max}$  represents the maximum H coordination of heteroatom A. The Eq (1) and (2) are also applied for the case where the hydrogen atoms of  $AH_x$  are replaced by saturated alkyl fragments (R) (e.g.,  $AH_{x-1}R$ ).

For a bi-dentate adsorbate, the scaling relation is<sup>25</sup>

$$\Delta E(AH_xBH_y) = \gamma(x)\Delta E(A) + \gamma(y)\Delta E(B) + \xi \quad (3)$$

where

$$\gamma(x) = \frac{x_{max}-x-z_A}{x_{max}} \quad (4)$$

$$\gamma(y) = \frac{y_{max}-y-z_B}{y_{max}} \quad (5)$$

$$\gamma(x) + \gamma(y) = n - (M/4) \quad (6)$$

$z_A$  and  $z_B$  are the total number of internal single bonds between atom A and other non-H atoms of the molecule and between atom B and other non-H atoms of the molecule, respectively.  $n$  is the number of surface-bonded atoms, and  $M$  is the total number of internal single bonds including A-H bonds of the surface-bonded atoms where the bond between two surface-bonded atoms is counted twice. The detailed derivation for this equation can be found in ref 25.<sup>25</sup> The  $\xi$  values in Eq (1) and (3) are fit constants which we determined using molecular binding energies on the Rh surface and the same  $\xi$  value for a given adsorbate is applied for all other metals. For the molecular binding energies on a sulfur-poisoned surface, atomic binding energies destabilized by a co-adsorbed S atom were substituted into the scaling relation with the use of the  $\xi$  value determined on a sulfur-free surface.

Atomic binding energies without S (or with S) are the relative energies based on the energy sum of atomic gas and the corresponding metal surface without S (or with S). Molecular binding energies without S (or with S) are the relative energy based on the energy sum of propane gas, steam, and the Rh surface without S (or with S) as follows,<sup>33</sup>





$$\begin{aligned}
\Delta E(C_x H_y O_z^*) &= E(C_x H_y O_z^*/metal\ surface) \\
&+ (3 - x) \times [E(C^*/Rh\ surface) - E(Rh\ surface)] \\
&+ (10 - y) \times [E(H^*/Rh\ surface) - E(Rh\ surface)] \\
&+ (1 - z) \times [E(O^*/Rh\ surface) - E(Rh\ surface)] \\
&- E(C_3 H_8) - E(H_2 O) - E(metal\ Surface)
\end{aligned} \tag{7}$$

where \* represents a bare or S adsorbed surface.

With Eq. 7, the molecular binding energy is defined relative to propane gas, steam, and the bare surface where the reference state for removed C, H, or O species uses Rh-based values for all surfaces such that variations in binding energies depend only on the  $C_x H_y O_z$  binding interaction.

Activation barriers can be estimated using BEP relations. A traditional BEP relation represents the correlation between reaction energy and activation barrier, written as

$$E_a = \alpha \Delta E_{rxn} + \beta \tag{8}$$

where  $E_a$  is activation barrier,  $\Delta E_{rxn}$  is reaction energy, and  $\alpha$  and  $\beta$  are constants related to the specific class of reaction. For the case where the traditional BEP does not fit well, the following BEP relation was used

$$E_{TS} = \alpha(E_{IS}\ or\ E_{FS}) + \beta \tag{9}$$

where  $E_{TS}$  is a transition state energy,  $E_{IS}$  or  $E_{FS}$  are an initial state energy or a final state energy, respectively. All the energies ( $E_{IS}$ ,  $E_{FS}$ , and  $E_{TS}$ ) without S (or with S) are relative energies (Eq. 7) on the basis of the energy sum of propane gas, steam, and the corresponding surface without S (or with S).

## 4.3 Results and Discussion

### 4.3.1 Propane reforming reaction path

A previous DFT analysis of methane steam reforming on the Ni(111) surface informed the set of elementary steps we include in our propane reforming analysis.<sup>31</sup> The first important finding is that  $\text{CH}_x$  intermediates prefer C-H dissociation over O or OH addition before reaching the  $\text{CH}^*$  species. The reported activation barriers for  $\text{O}^*$  or  $\text{OH}^*$  addition to  $\text{CH}_3^*$  are 152 and 125  $\text{kJ}\cdot\text{mol}^{-1}$ , respectively, whereas that for C-H breaking of  $\text{CH}_3^*$  is 66  $\text{kJ}\cdot\text{mol}^{-1}$ . We do not include C-O bond forming steps for  $\text{CH}_x$  where  $x > 1$  in our analysis. The addition reactions of O or OH to  $\text{CH}^*$  are key elementary steps with high activation barriers, shown to be rate determining for  $\text{H}_2$  production from methane. Thus we consider O or OH addition only to the  $\text{CH}^*$  and  $\text{C}^*$  adsorbates, and C-H reactions only for other  $\text{CH}_x$  species.

Previous DFT studies of propane dehydrogenation/decomposition further inform our choice of elementary steps to include.<sup>33,34</sup> As a propane molecule adsorbs to the surface, several C-H breaking steps precede a C-C breaking step. There are two possible points within the dehydrogenation sequence at which C-C breaking potentially occurs. The C-C breaking is highly likely to take place at propyne ( $\text{CH}_3\text{CCH}^*$ ) or propynyl ( $\text{CH}_3\text{CC}^*$ ) intermediates, as shown in Figure 4-1, due to high exothermicity of these bond breaking steps. We refer to two reaction paths as the propyne path and the propynyl path. The propyne path has the sequence of propane ( $\text{CH}_3\text{CH}_2\text{CH}_3^*$ ), 1-propyl ( $\text{CH}_3\text{CH}_2\text{CH}_2^*$ ), propylene ( $\text{CH}_3\text{CHCH}_2^*$ ), 2-propenyl ( $\text{CH}_3\text{CCH}_2^*$ ), propyne ( $\text{CH}_3\text{CCH}^*$ ), and  $\text{CH}_3\text{C}^*/\text{CH}^*$ . The propynyl path has the sequence of propane, 1-propyl, 1-propylidene ( $\text{CH}_3\text{CH}_2\text{CH}^*$ ), propylidyne ( $\text{CH}_3\text{CH}_2\text{C}^*$ ), propenylidene ( $\text{CH}_3\text{CHC}^*$ ), propynyl ( $\text{CH}_3\text{CC}^*$ ), and  $\text{CH}_3\text{C}^*/\text{C}^*$ . The adsorption configurations of each intermediate used herein are similar to ref 33.<sup>33</sup>

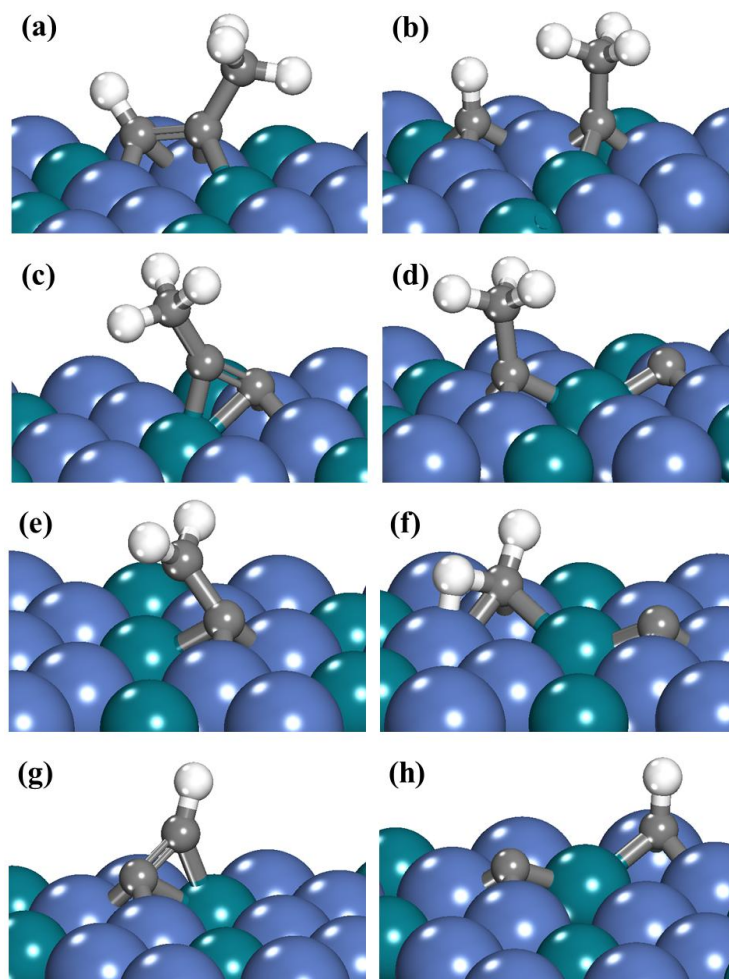


Figure 4-1 Initial and final states of C-C dissociation of propyne (a, b), propynyl (c, d),  $\text{CH}_2\text{C}^*$  (e, f), and  $\text{CHC}^*$  (g, h) on the  $\text{Rh}_1\text{Ni}_2(111)$  surface. Dark-gray spheres (green), Rh; large light-gray sphere (blue), Ni; small light-gray spheres (gray), C; white spheres (white), H.

Both the propyne and propynyl adsorbates produce  $\text{CH}_3\text{C}^*$  after C-C breaking. Previous work of Y. Chen et al.<sup>32</sup> suggests that  $\text{CH}_3\text{C}^*$  preferentially dissociates to  $\text{CH}_2\text{C}^*$ .  $\text{CH}_2\text{C}^*$  can then follow either of two paths, the sequence of  $\text{CH}_2\text{C}^*$ ,  $\text{C}^* + \text{CH}_2^*$ ,  $\text{C}^* + \text{CH}^*$  and the sequence of  $\text{CH}_2\text{C}^*$ ,  $\text{CHC}^*$ ,  $\text{C}^* + \text{CH}^*$ . The initial and final states for the C-C breaking steps for each path are illustrated in Figure 4-1.  $\text{CH}_2\text{C}^*$  has the same activation barrier for both C-C and C-H breakings on Pt(111), so the preferred path can be speculated based on the product stability ( $\text{C}^* + \text{CH}_2^*$  or  $\text{CHC}^* + \text{H}^*$ ) after C-C or C-H dissociation. The

path going through  $\text{CH}_2^*$  is preferred as the activation barrier of C-H dissociation of  $\text{CH}_2^*$  is lower than that of C-C breaking of  $\text{CHC}^*$ . For example, the difference in activation barrier on Pt(111) between those two steps amounts to 0.73 eV. Thus, we can expect  $\text{CH}_3\text{C}^*$  intermediates to prefer the sequence of  $\text{CH}_3\text{C}^*$ ,  $\text{CH}_2\text{C}^*$ ,  $\text{C}^*+\text{CH}_2^*$ ,  $\text{C}^*+\text{CH}^*$  where the initial and final states of the C-C dissociation reaction of  $\text{CH}_2\text{C}^*$  are shown in Figure 4-1 e,f, however, the less preferred path is also considered herein.

Conclusions of previous studies have thus allowed us to limit the number of elementary steps we consider for propane reforming. Within the preferred paths, 28 intermediates and 31 elementary steps remain to be considered. Of these elementary steps, 17 are C-H dissociation/formation, 4 are C-C dissociation, 4 are C-O formation, 5 are O-H dissociation, and one is  $\text{H}_2$  formation.

### 4.3.2 Transition states

To establish a BEP relation, DFT is used to locate several transition states to make a linear plot of activation barriers against reaction energies or transition state energies against initial/final state energies. We selected representative reactions within each reaction type such as C-H, O-H, C-C, C-O, and C-OH dissociation as shown in Table 4-1. Figure 4-2 illustrates initial, transition, and final states for a subset of reaction steps over the Rh(111) surface (All states are illustrated in Figure S1.). Figure 4-2 also shows the coadsorption configuration of initial states with S atoms for consideration of S-coadsorption effects on reaction energetics. The optimal adsorption configurations of the intermediates having a functional group of O or OH were chosen based on previous examination of methanol dehydrogenation on the Pd(111) surface,<sup>46</sup> and  $\text{CH}_4$  reforming reactions on the Ni(111) surface.<sup>47</sup> The adsorption configurations for C-H dissociation of propane and C-C dissociation of propyne and propynyl were referred to the literature of propane dehydrogenation.<sup>33</sup> The activation barrier for  $\text{H}_2$  formation was determined with DFT and is not included in any BEP relationship. Transition states were located for the representative reactions over each of the four surfaces with and without co-adsorbed S atoms. The sulfur atom for each sulfur-poisoned

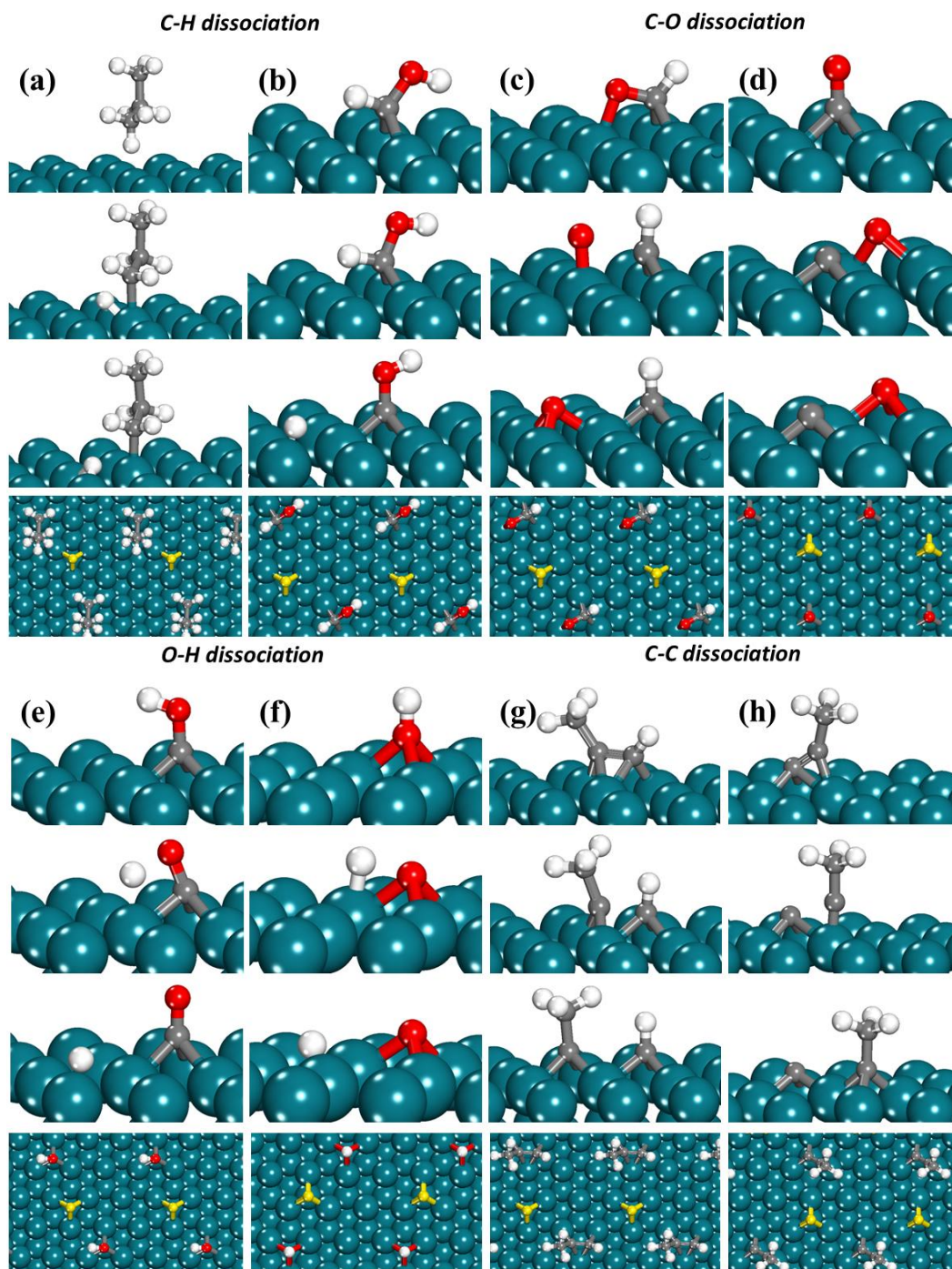


Figure 4-2. Initial (top), transition (middle top), final (middle bottom) states, and initial states with co-adsorbed sulfur (bottom) on the Rh(111) surface of C-H dissociation of (a) propane and (b) CHOH; C-O dissociation of (c) CHO and (d) CO; O-H dissociation of (e) COH and (f) OH; C-C dissociation of (g) propyne and (h) propynyl. Large gray sphere (green), Rh; small gray spheres (gray), C; white spheres (white), H; dark sphere (red), O; light gray sphere (yellow), S.

Table 4-1. DFT calculated activation energies ( $E_a$ , eV) and reaction energies ( $E_{rxn}$ , eV) on each metal surface classified according to reaction type.

		<i>C-H dissociation</i>						<i>C-C dissociation</i>				<i>H<sub>2</sub></i>	
		$\text{CH}_3\text{CH}_2\text{CH}_3 \rightarrow \text{CH}_3\text{CH}_2\text{CH}_2 + \text{H}$		$\text{CHOH} \rightarrow \text{COH} + \text{H}$		$\text{CHO} \rightarrow \text{CO} + \text{H}$		$\text{CH}_3\text{CCH} \rightarrow \text{CH} + \text{CH}_3\text{C}$		$\text{CH}_3\text{CC} \rightarrow \text{C} + \text{CH}_3\text{C}$		$\text{H} + \text{H} \rightarrow \text{H}_2$	
		$E_a$	$E_{rxn}$	$E_a$	$E_{rxn}$	$E_a$	$E_{rxn}$	$E_a$	$E_{rxn}$	$E_a$	$E_{rxn}$	$E_a$	$E_{rxn}$
Rh	clean surface	0.61	0.23	0.05	-0.83	0.33	-1.09	0.81	-0.38	2.13	-0.45	0.56	0.55
Ni		0.84	0.52	0.07	-0.81	0.19	-1.28	0.89	0.12	1.78	0.17	0.93	0.83
Rh <sub>1</sub> Ni <sub>2</sub>		0.63	0.30	0.25	-0.68	0.28	-1.10	0.87	0.12	2.50	-0.03	0.87	0.86
Rh <sub>2</sub> Ni <sub>1</sub>		0.60	0.22	0.36	-0.57	0.32	-1.07	0.92	-0.16	1.72	-0.16	0.52	0.48
Rh	sulfur poisoned surface	0.76	0.41	0.15	-0.69	0.30	-1.10	0.97	-0.20	2.22	-0.31	0.55	0.54
Ni		0.99	0.63	0.18	-0.67	0.15	-1.27	1.06	0.17	1.86	0.21	0.93	0.83
Rh <sub>1</sub> Ni <sub>2</sub>		0.75	0.42	0.38	-0.54	0.30	-1.07	0.95	0.21	2.47 <sup>a</sup>	0.01	0.88	0.84
Rh <sub>2</sub> Ni <sub>1</sub>		0.73	0.38	0.47	-0.44	0.30	-1.06	1.04	-0.08	1.80	-0.06	0.49	0.46
		<i>O-H dissociation</i>				<i>C-OH dissociation</i>				<i>C-O dissociation</i>			
		$\text{COH} \rightarrow \text{CO} + \text{H}$		$\text{OH} \rightarrow \text{O} + \text{H}$		$\text{CHOH} \rightarrow \text{CH} + \text{OH}$		$\text{CHOH} \rightarrow \text{CH} + \text{OH}$		$\text{CHO} \rightarrow \text{CH} + \text{O}$		$\text{CO} \rightarrow \text{C} + \text{O}$	
		$E_a$	$E_{rxn}$	$E_a$	$E_{rxn}$	$E_a$	$E_{rxn}$	$E_a$	$E_{rxn}$	$E_a$	$E_{rxn}$	$E_a$	$E_{rxn}$
Rh	clean surface	0.97	-0.71	0.99	-0.21	0.66	-0.39	1.84	1.01	2.11	-0.13	2.97	1.60
Ni		0.95	-0.96	1.10	-0.08	0.50	-0.78	1.90	0.69	1.91	-0.27	2.91	1.64
Rh <sub>1</sub> Ni <sub>2</sub>		0.89	-0.88	1.15	-0.08	0.59	-0.53	1.91	0.67	1.88	-0.21	2.90	1.64
Rh <sub>2</sub> Ni <sub>1</sub>		0.95	-0.82	1.01	-0.22	0.65	-0.42	1.83	0.73	1.85	-0.14	3.02	1.57
Rh	sulfur poisoned surface	0.97	-0.68	1.04	-0.13	0.65	-0.26	1.92	1.15	2.23	0.06	3.16	2.08
Ni		1.03	-0.93	1.08	0.05	0.56	-0.66	1.96	0.76	2.33	-0.08	3.22	2.08
Rh <sub>1</sub> Ni <sub>2</sub>		0.91	-0.82	1.13	-0.01	0.65	-0.41	1.95	0.72	2.34	0.00	2.96	1.81
Rh <sub>2</sub> Ni <sub>1</sub>		0.97	-0.76	1.04	-0.13	0.71	-0.28	1.88	0.87	1.95	-0.01	3.20	2.10

<sup>a</sup>This  $E_a$  is based on an incomplete transition state which satisfies all the criteria to be a transition state except for the one where the forces on all atoms are less than 0.05 eVÅ<sup>-1</sup>. Even though this is an incomplete data, it is used in a BEP plot because the forces were seldom optimized and the use of this data point improves the BEP prediction.

surface was placed at the site as far from molecular adsorbates as possible, within the 3×3 cell, after the molecular adsorbate was placed at its preferred adsorption site. The sulfur atom is 3~5 Å away from reactant species, depending on the molecular size of the adsorbate. Table 4-1 reports the DFT determined activation energies and reaction energies.

### 4.3.3 Application of scaling and BEP relations

Using the energetics in Table 4-1, three different types of BEP relations, activation barrier versus reaction energy and transition state energy versus initial or final energy, were examined for each metal according to reaction types. Figure 4-3 shows the comparison on Rh(111) where the BEP relationships based on initial or final energies fits well for C-H, O-H, and C-C breaking and the BEP based on reaction energy fits well for C-O and C-OH dissociation. These trends are also found in other metals, as shown by the best fit BEP lines given in Table 4-2. We highlight that the data used in the BEP plots include energetics on both the S-free and S-coadsorbed surfaces. The established BEP plots (Table 4-2) were applied to estimate activation barriers as shown in Figure 4-4 a,c,e where the input parameters (i.e., initial/final state energies or reaction energies) were predicted by scaling relations of Eq. 3. This approach turns out to produce significant deviations from actual  $E_a$  values (i.e., DFT-calculated  $E_a$  values by the NEB method) with the maximum deviations for both HOC-H and OC-H dissociation barriers at 0.3 eV. A small range of metal change such as our system ranging from pure Rh, Ni to binary Rh-Ni metals have about only 0.1 eV difference between minimum and maximum values in the actual activation barrier of

Table 4-2. Representative BEP relations on each metal according to reaction types where  $a$  and  $b$  indicate slope and intercept in a BEP plot, respectively.

Reaction type	Metal	BEP type	$a$	$b$	$R^2$	Reaction type	Metal	BEP type	$a$	$b$	$R^2$
C-H	Rh	$E_{TS}$ vs $E_{FS}$	0.405	0.166	0.95	C-O	Rh	$E_a$ vs $E_{rxn}$	0.474	2.187	1.00
	Rh <sub>2</sub> Ni <sub>1</sub>		0.398	0.185	0.98		Rh <sub>2</sub> Ni <sub>1</sub>		0.623	1.957	0.99
	Rh <sub>1</sub> Ni <sub>2</sub>	0.338	0.174	0.89	Rh <sub>1</sub> Ni <sub>2</sub>		0.459		2.149	0.92	
	Ni	0.432	0.324	0.99	Ni		0.476		2.192	0.94	
C-C	Rh	$E_{TS}$ vs $E_{IS}$	3.402	4.283	0.96	C-OH	Rh	$E_a$ vs $E_{rxn}$	0.863	0.946	0.99
	Rh <sub>2</sub> Ni <sub>1</sub>		2.932	3.563	0.99		Rh <sub>2</sub> Ni <sub>1</sub>		1.011	1.043	0.99
	Rh <sub>1</sub> Ni <sub>2</sub>	4.003	4.662	0.95	Rh <sub>1</sub> Ni <sub>2</sub>		1.123		1.151	1.00	
	Ni	3.698	3.707	0.97	Ni		0.967		1.225	1.00	
O-H	Rh	$E_{TS}$	1.066	1.056	1.00						
	Rh <sub>2</sub> Ni <sub>1</sub>	vs	1.134	1.124	1.00						
	Rh <sub>1</sub> Ni <sub>2</sub>	$E_{IS}$	1.684	1.658	0.98						
	Ni	*	0.105	1.090	0.74						

\* The O-H dissociation on Ni fits better the BEP type of  $E_a$  vs  $E_{rxn}$  than that of  $E_{TS}$  vs  $E_{IS}$ .

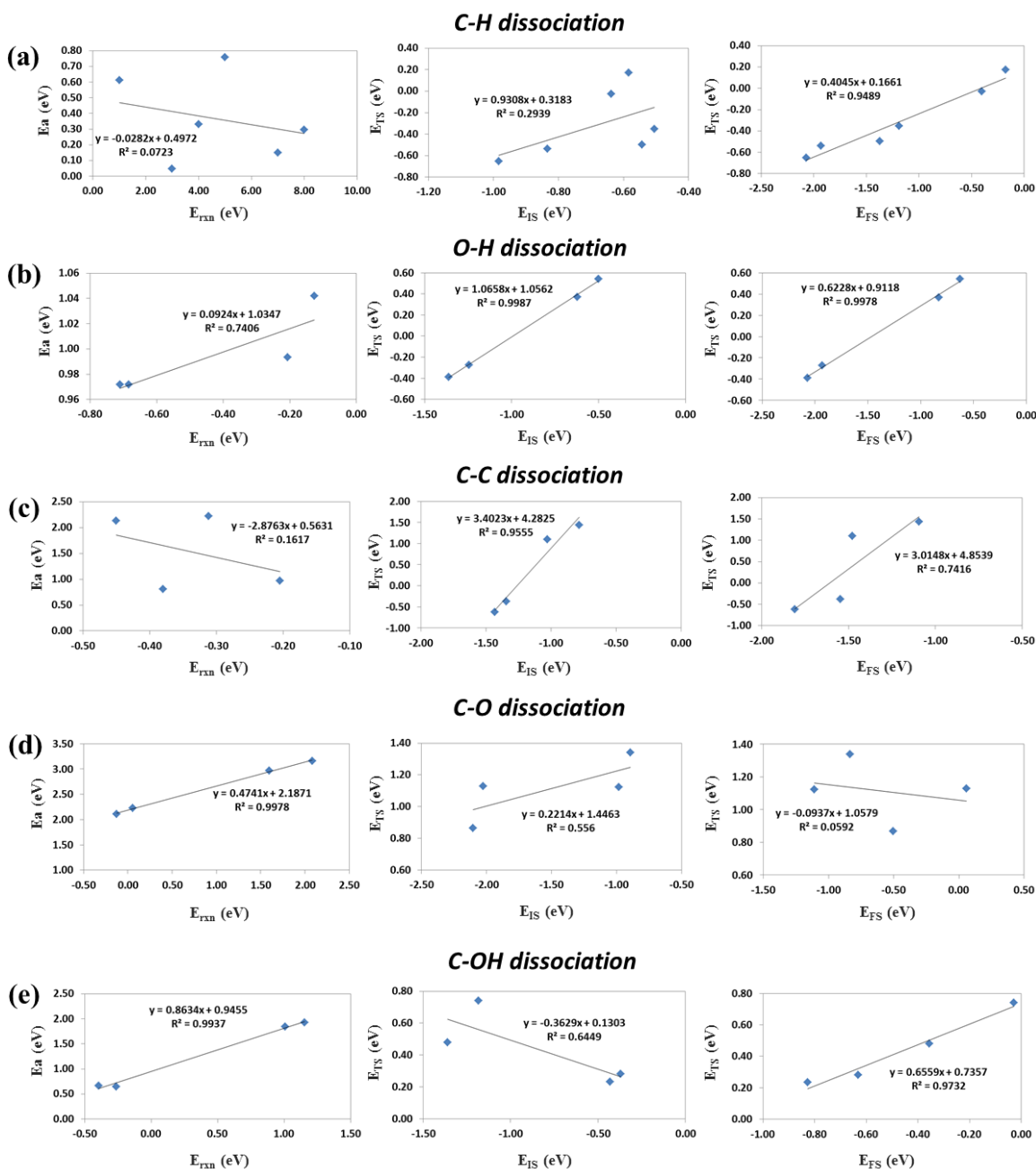


Figure 4-3. Comparison of three different BEP plots according to reaction types (C-H dissociation, a; O-H dissociation, b; C-C dissociation, c; C-O dissociation, d; C-OH dissociation, e) on Rh(111); Left plots are  $E_a$  (activation barrier) versus  $E_{rxn}$  (reaction energy), middle plots are  $E_{TS}$  (relative transition state energy) versus  $E_{IS}$  (relative initial state energy), and right plots are  $E_{TS}$  versus  $E_{FS}$  (relative final state energy). Relative energies are based on the reference state of propane gas, steam, and a corresponding metal surface.



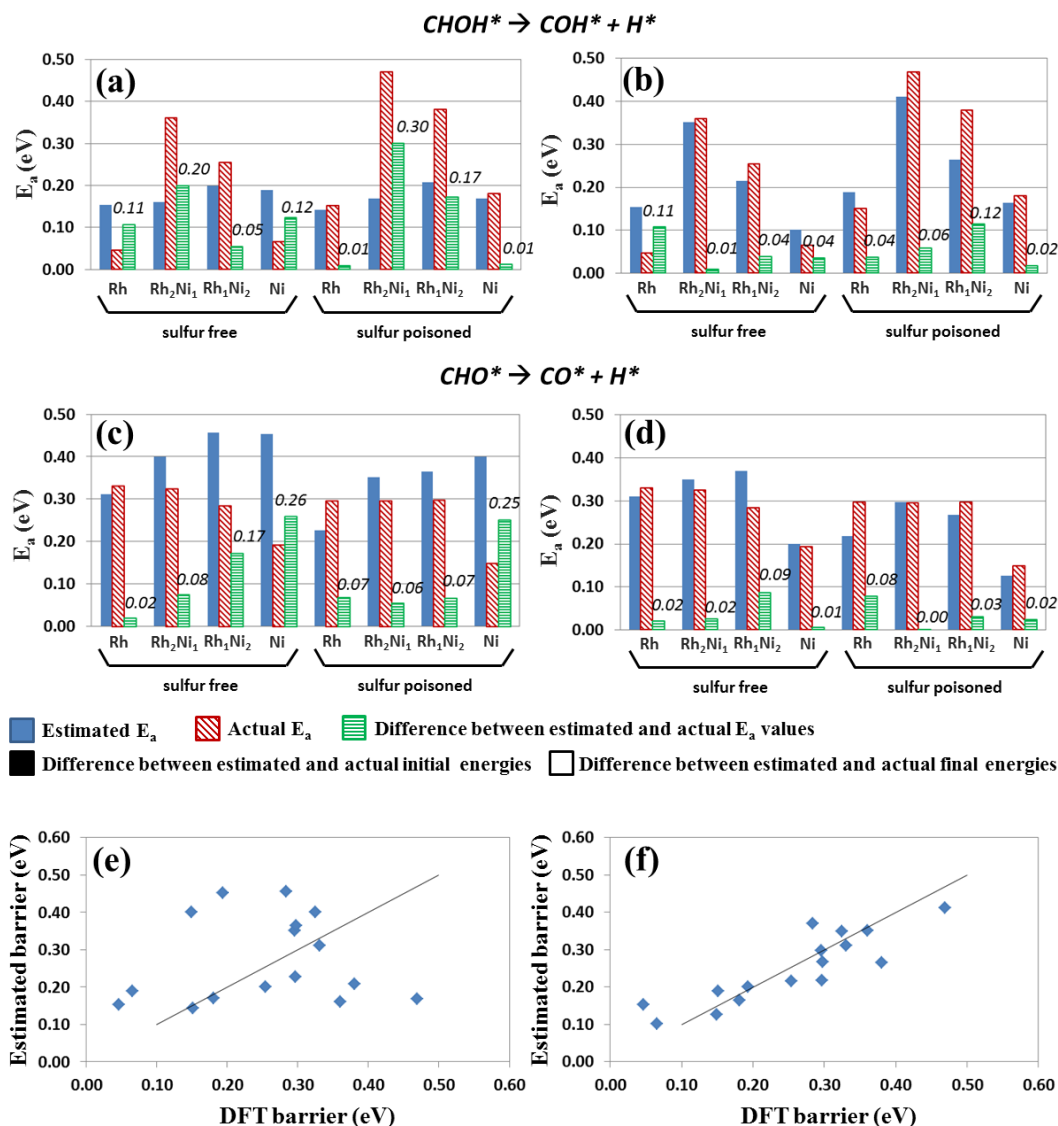


Figure 4-4. Comparison between the  $E_a$  estimates (blue solid bar) (by scaling and BEP relations, a and c; by BEP relations only, b and d) and DFT  $E_a$  values (red diagonal striped bar) for two C-H dissociation reactions of CHOH (a, b) and CHO (c, d). The difference between the two values is indicated by a green horizontal striped bar with a number indicating the size of the bar. Estimation accuracy is compared in e, f by plotting activation barrier estimates (by scaling and BEP relations, e; by BEP relations only, f) versus DFT-calculated barriers for the C-H dissociation reactions of both CHOH and COH.

CHO dehydrogenation (Figure 4-4 c,d), so the error levels in Figure 4-4 a,c are not acceptable for mechanistic comparison among surfaces. For example, in the CHOH dehydrogenation reaction (Figure 4-4a), actual  $E_a$  values are higher on Rh-Ni binary metals than pure metals, whereas the estimated values are similar between binary and pure metals. In the CHO dehydrogenation reaction (Figure 4-4c), the actual  $E_a$  values decrease as the ratio of Ni in binary metals increases and reaches a minimum in pure Ni, but the estimated values in Figure 4-4c show an opposite trend.

By comparing the error bars of activation barrier prediction and those of scaling prediction for initial and final energies, we found that the metal surface with a large error in scaling prediction also has a large error in activation barrier prediction. Figure 4-5 shows the error distribution of the estimation of scaling relationships over each metal in initial state and final state energies for seven elementary steps. The maximum errors for both the initial and final states are about 0.4 eV. If the errors of both initial and final states are accumulated, the maximum error can be compounded leading to significant prediction errors between similar metals. Therefore, these analyses suggest that the combined use of scaling and BEP relationships be avoided across this range of similar metals.

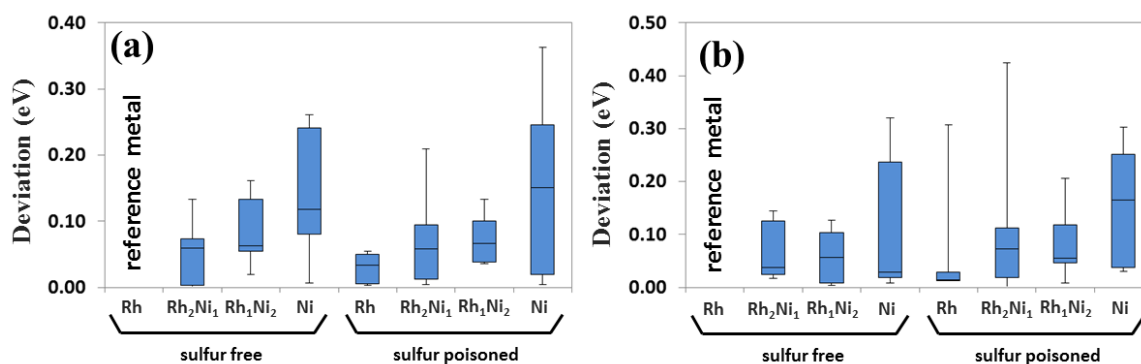


Figure 4-5. Deviation levels of initial (a) and final (b) state energies estimated by scaling relationships from DFT-calculated values on each metal surface for seven elementary steps;  $\text{CHOH}^* \rightarrow \text{COH}^* + \text{H}^*$ ,  $\text{CHO}^* \rightarrow \text{CO}^* + \text{H}^*$ ,  $\text{CHOH}^* \rightarrow \text{CH}^* + \text{OH}^*$ ,  $\text{CHO}^* \rightarrow \text{CH}^* + \text{O}^*$ ,  $\text{CO}^* \rightarrow \text{C}^* + \text{O}^*$ ,  $\text{COH}^* \rightarrow \text{CO}^* + \text{H}^*$ , and  $\text{OH}^* \rightarrow \text{O}^* + \text{H}^*$ . The boxes represent the middle 50 % of the data points (i.e. the bottom and top boundaries of a box indicate a lower quartile and an upper quartile, respectively) and the line in the box indicates the median. The minimum and maximum values among a given data set are indicated by whiskers.

#### 4.3.4 Application of BEP relation without using scaling relation

The DFT-calculated initial and final energies for dehydrogenation of CHOH and COH without using a scaling relation are used in BEP relations to calculate activation barriers and plotted in Figure 4-4 b and d. The use of only BEP provides reliable trends in estimated activation barriers across metals and reduced errors relative to the DFT values. For example, in Figure 4-4 a and c, the estimated  $E_a$  value on Ni is similar to those on binary metals in contrast to the trend of DFT values, whereas using a BEP relationship only (Figure 4-4 b, d), the estimated barriers on Ni are properly lower than Rh-Ni binary metals. The agreement level between estimated and DFT-calculated barriers is examined in Figure 4-4 e, f which verifies that the estimation accuracy is more enhanced by using BEP relations only rather than using combined scaling and BEP relations.

A box plot analysis in Figure 4-6 elucidates differences in estimation accuracy among the four approaches. Merging the data points from all metals for a given reaction type into a single BEP plot, which is shown in Table S1, is also examined in this analysis and denoted as BEP(I). BEP(II) represents the BEP relations listed in Table 4-2. The same box plot analysis for other reactions can be found in Figure S2. The plots in Figure 4-6 exhibit that the combined use of scaling and BEP relations produce significant errors for both SR&BEP(I) and SR&BEP(II). These errors are decreased by using BEP only (i.e., BEP(I) or BEP(II)) as one can find a further decrease in all the indices of box plot. As the errors from SR&BEP(I)/(II) are qualitatively unacceptable, we suggest that the application of only BEP is suitable for the energetic prediction over similar metals. This approach is also supported by a recent statistical study suggesting that the combined use of the two estimation methods produces a critical error and has to be restrained.<sup>48</sup> There is not much difference between the results of BEP(I) and (II), but BEP(II) enhances estimation accuracy for a couple of reactions as shown in Figure 4-6c, thus we estimate the energetics of propane steam reforming based on BEP(II) (i.e., Table 4-2).

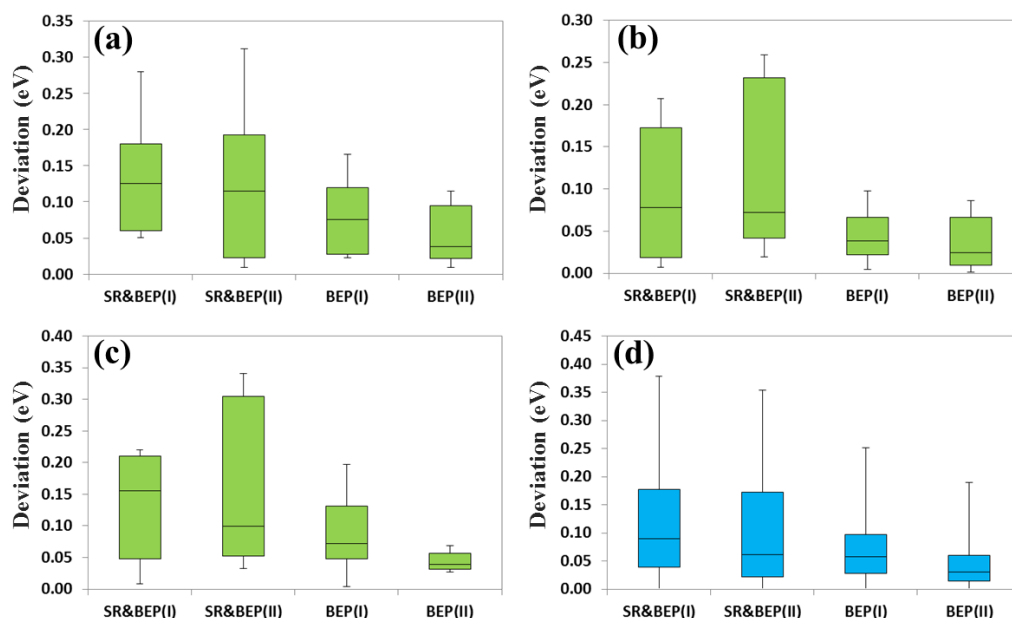


Figure 4-6. Deviation of activation barriers estimated by various estimation methods from DFT  $E_a$  values calculated by the NEB method on each metal for the C-H dissociation reactions of CHOH (a) and CHO (b), the C-OH dissociation reaction of CHOH (c), and seven elementary steps (d) which are  $\text{CHOH}^* \rightarrow \text{COH}^* + \text{H}^*$ ,  $\text{CHO}^* \rightarrow \text{CO}^* + \text{H}^*$ ,  $\text{CHOH}^* \rightarrow \text{CH}^* + \text{OH}^*$ ,  $\text{CHO}^* \rightarrow \text{CH}^* + \text{O}^*$ ,  $\text{CO}^* \rightarrow \text{C}^* + \text{O}^*$ ,  $\text{COH}^* \rightarrow \text{CO}^* + \text{H}^*$ , and  $\text{OH}^* \rightarrow \text{O}^* + \text{H}^*$ . SR, scaling relations; BEP(I), use of an identical BEP relation for all metals for a given reaction type; BEP(II), use of a different BEP relation for each metal for a given reaction type.

### 4.3.5 Energy profile of propane steam reforming

The potential energy surface for all elementary steps along the considered reaction paths is illustrated in Figure 4-7 for the four metal surfaces. DFT methods were used to calculate the initial and final state energies for all species over all four surfaces with and without co-adsorbed S atoms (structures in Figure S3). The BEP relationships given in Table 4-2 were used to calculate all activation barriers. Dashed vertical lines in Figure 4-7 specify reaction sections, and consideration of the full path is done by moving species between sections. For example, the subsequent reactions of  $\text{C}^*$  and  $\text{CH}_3\text{C}^*$  products from the C3 intermediates (propynyl path) section are examined in the C2 intermediates,  $\text{CH}_4$  formation, and

CO formation (III) sections. There are two different reaction paths for C2 and C3 intermediates and three reaction paths for CO formation, which are named as C2 intermediates I/II, propyne/propynyl paths and CO formation I/II/III, respectively. For C3 intermediates, the propyne path is clearly preferred to the propynyl path because the energetics of propyne path are downhill with lower activation barriers, whereas the propynyl path consists of a couple of endothermic reactions with the C-C breaking step having a higher activation barrier. The preference for the propyne path is in line with propane dehydrogenation energetics on the Pt(111) surface based on DFT-calculated values.<sup>34</sup> For C2 intermediates, path II involving the C-H cleavage of  $\text{CH}_2\text{C}^*$  contains an elementary step with the largest activation barrier over the entire elementary steps of propane steam reforming, confirming the path preference expected based on the Pt(111) literature<sup>32</sup> which appears more clearly for the Rh and Ni metals..

For CO formation, the path of OH addition to  $\text{C}^*$  or  $\text{CH}^*$  (i.e., CO formation II/III) is favored over the path of O addition (i.e., CO formation I) due to the OH addition reaction having a lower activation barrier and more exothermic reaction energies in the elementary steps. This is also consistent with the previous energetic analysis of methane steam reforming on the Ni(111) surface, but this study additionally suggests that the reaction flux is more involved in the O addition path (i.e., CO formation I) than the OH addition path (i.e., CO formation II/III) because of the high concentration of  $\text{O}^*$  based on a microkinetic analysis.<sup>31</sup> Thus, we consider both paths for the analysis in the following section.

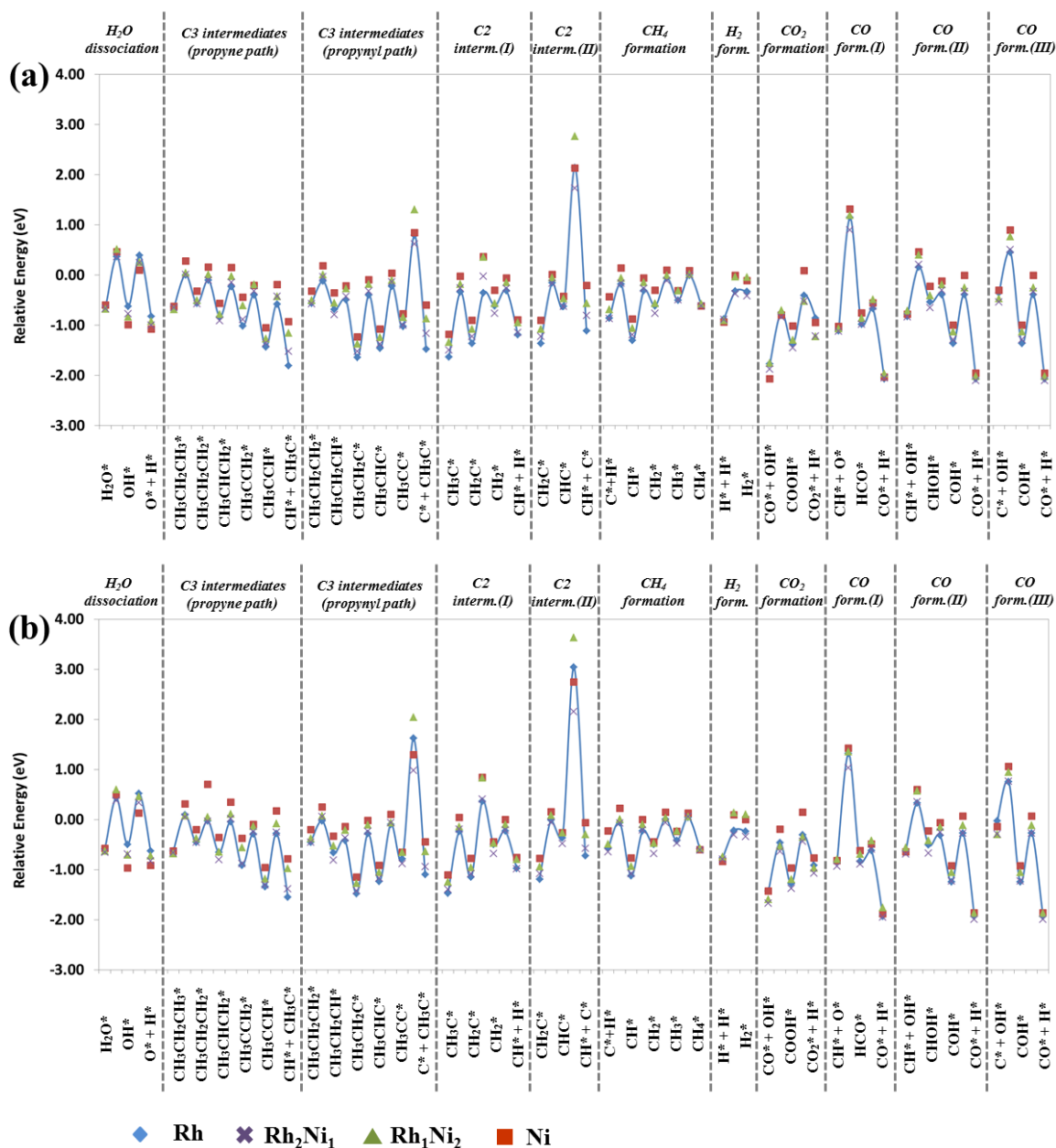


Figure 4-7. Energy profile of propane steam reforming reaction estimated by the BEP relation on four metal surfaces under sulfur free condition (a) and under sulfur poisoned condition (b). The relative energy of each intermediate is defined by Eq. 7.

### 4.3.6 Sulfur tolerance of Rh-Ni binary metals

The energetics of propane steam reforming are analyzed by comparing average activation barriers on sulfur-poisoned surfaces to identify critical elementary reactions in Figure 4-8. The elementary steps with the highest activation barrier, averaged across the four metals, are the C-C cleavage of  $\text{CHC}^*$  followed by the cleavage of propynyl ( $\text{CH}_3\text{CC}^*$ ), the O addition to  $\text{CH}^*$ , the C-C cleavage of  $\text{CH}_2\text{C}^*$ , and then several steps with similar barriers including dehydrogenation steps of C2/C3 intermediates, the propyne C-C breaking, OH addition reactions, and  $\text{H}_2\text{O}$  dissociation reactions. Figure 4-9 shows the comparisons of the activation barriers for both the sulfur free and poisoned surfaces in these critical reaction steps. For the C-C breaking steps of both  $\text{CH}_3\text{CC}^*$  and  $\text{CHC}^*$ , the activation energy on  $\text{Rh}_2\text{Ni}_1$  is lower than Rh for both the sulfur free and poisoned surfaces. In particular, the difference between Rh and  $\text{Rh}_2\text{Ni}_1$  becomes larger in the presence of sulfur, implying the high sulfur tolerance of binary Rh-Ni metals. For the O addition to  $\text{CH}^*$ , which has the third highest activation barrier,  $\text{Rh}_2\text{Ni}_1$  is also the best catalyst in the presence of sulfur. It may be possible for both the C-C breaking steps of  $\text{CH}_3\text{CC}^*$  and  $\text{CHC}^*$  to be excluded as they are less preferred to other competitive paths, as mentioned in the previous section. In this case, the  $\text{O}^*$  addition step to  $\text{C}^*$  is the elementary step having the highest activation barrier where  $\text{Rh}_2\text{Ni}_1$  is the best catalyst. Thus,  $\text{Rh}_2\text{Ni}_1$  is the most sulfur tolerant catalyst for the most critical step for both the cases of inclusion and exclusion of the less preferred paths. In the C-C breaking of  $\text{CH}_2\text{C}^*$ , the binary metals provide similar sulfur resistance to Rh, but in the dehydrogenation step of  $\text{CCH}_3^*$ , which has a significant barrier,  $\text{Rh}_2\text{Ni}_1$  is more sulfur tolerant. The majority of steps have the lowest activation barrier on  $\text{Rh}_2\text{Ni}_1$  in the presence of sulfur.

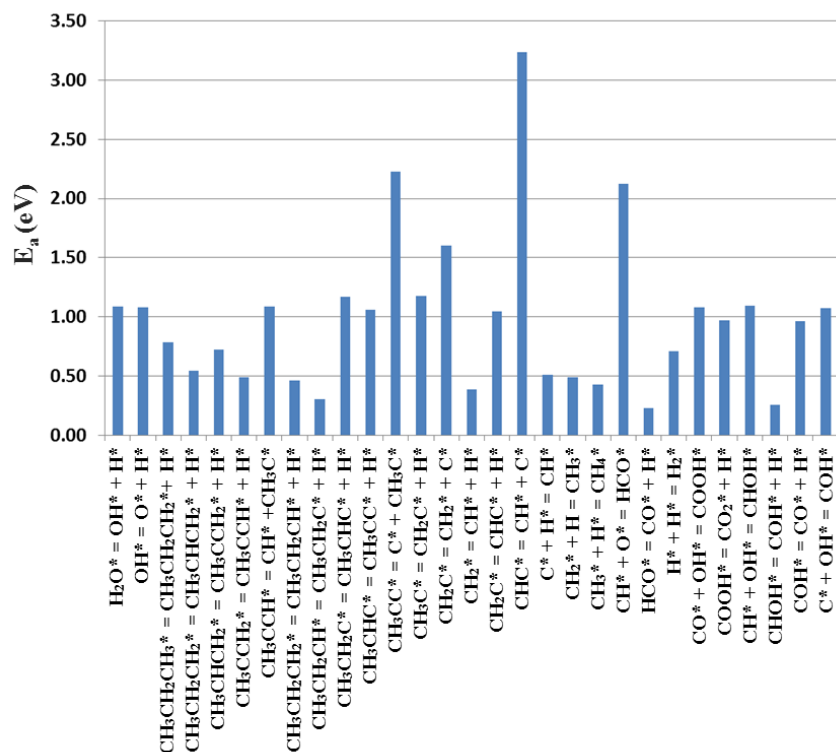


Figure 4-8. Average activation barriers of elementary steps along the preferred reaction paths of propane steam reforming reaction on sulfur-poisoned four metal surfaces

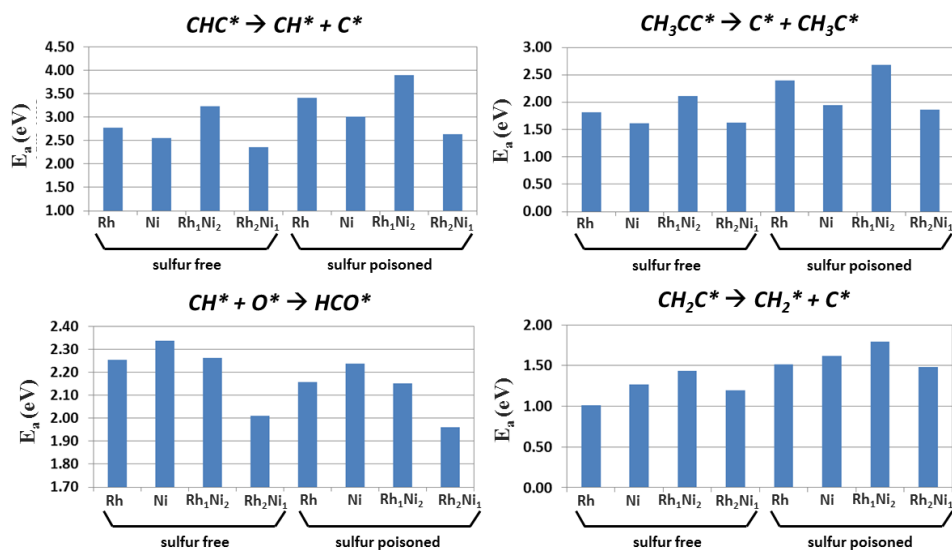


Figure 4-9. Comparison of activation barriers across metals for four elementary reactions with high activation barriers along the reaction path of propane steam reforming



Without more detailed kinetic modeling, we cannot be conclusive as to which steps determine the rate of propane reforming. To broadly consider the impact of sulfur poisoning, we averaged the barrier changes by co-adsorbed  $S^*$  over all the elementary steps according to reaction types in Figure 4-10 a,b. For bond breaking steps (Figure 4-10a), the C-C breaking steps are affected most by sulfur poisoning, and  $Rh_2Ni_1$  presents the highest sulfur tolerance. This is reflected in the comparison of overall deactivation levels averaging all bond breaking steps. Bond formation steps (Figure 4-10b) are promoted by the presence of sulfur, as reflected by decreased activation barriers. The promotion effect of sulfur presence is larger on pure metals than on both  $Rh_1Ni_2$  and  $Rh_2Ni_1$ , but the difference is less than 0.05 eV which is negligible. Finally, the overall S effect on all reaction steps (Figure 4-10c) are minimized most on  $Rh_2Ni_1$  where the sulfur tolerance effect on  $Rh_2Ni_1$  arises from C-C bond breaking steps.

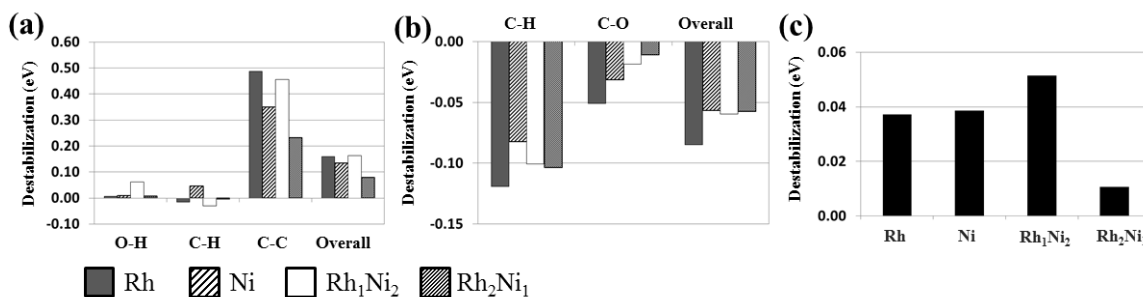


Figure 4-10. Average activation barrier changes on each metal due to co-adsorbed  $S^*$  according to reaction types including (a) dissociation of O-H, C-H, C-C bonds and (b) association of C-H, C-O bonds. (c) Average destabilization levels of all elementary reactions on each metal.

Analysis of elementary reforming energetics suggests that Rh-Ni binary metal surfaces will demonstrate an enhanced S tolerance during steam reforming. Though the experimental studies of Strohm et al. indicated a 10% Ni-2% Rh sample as optimal, our reaction energetics results suggest a  $Rh_2Ni_1$  ratio shows greater sulfur tolerance. These results should be combined with our previous conclusion that the coverage of  $S^*$  under reforming conditions will be lower over higher concentration Ni binary metals in

explaining the experimental indication of Rh-Ni sulfur tolerance.<sup>10</sup> Our previous electronic structure analysis of CO dissociation suggests that the Rh-Ni binary metal surface lessens the repulsive interaction between S\* and other adsorbates, thereby reducing the local poisoning effect.<sup>11</sup> Kinetic modeling is necessary to definitively connect the calculated energetics to the experimentally observed behavior.

#### 4.4 Conclusions

We have examined scaling and BEP relations to predict the energetics of propane steam reforming on the Rh, Ni, Rh<sub>1</sub>Ni<sub>2</sub>, and Rh<sub>2</sub>Ni<sub>1</sub> (111) surfaces. The estimation of activation barriers by the combination of these two methods is too rough to discriminate the energetic trends on such a similar set of metals. The first refinement of estimation can be made by using a different BEP relation for each metal. The combined use of scaling and individual BEP relationships remains unreliable, in agreement with the recent suggestion of Sutton et al. that their combined use be avoided.<sup>48</sup> More effective refinement has been achieved by utilizing BEP relations based on DFT-calculated initial and final energies. For a rational design of catalysts for complex multi-step reactions using estimation methods, a scan for a wide range of transition metals may be a reasonable first step with the combined use of scaling and BEP relations, but a following narrow scan across metals near optimal performance is better restricted to using BEP relationships only.

BEP correlations were used to analyze the propane steam reforming mechanism. To simplify the complex reaction networks, the possible reaction paths of propane steam reforming were selected by referring to several previous reports and the potential energy surface of the elementary steps along those reaction paths was constructed. Four elementary steps with high activation barriers are the C-C cleavages of CHC\* and CH<sub>3</sub>CC\*, O addition to CH\*, and the C-C cleavage of CH<sub>2</sub>C\*. For all the four reactions, the activation barrier on Rh<sub>2</sub>Ni<sub>1</sub> is the lowest in the presence of sulfur, implying that high sulfur tolerance can be induced by binary Rh-Ni metals. The average S impact on activation barriers was compared for each

reaction type, and  $\text{Rh}_2\text{Ni}_1$  exhibits the lowest destabilization and corroborates the trend found in the most critical elementary reactions. Our previous study showed that the sulfur binding strength on Rh-Ni binary metals is weaker than on pure Rh.<sup>11,14</sup> Therefore, our analyses suggest that Rh-Ni binary metals provide relatively high sulfur tolerance compared to pure Rh as they can reduce both the S coverage and its impact on activation barrier increases. A microkinetic model is needed to further connect these energetics with realistic reaction conditions.

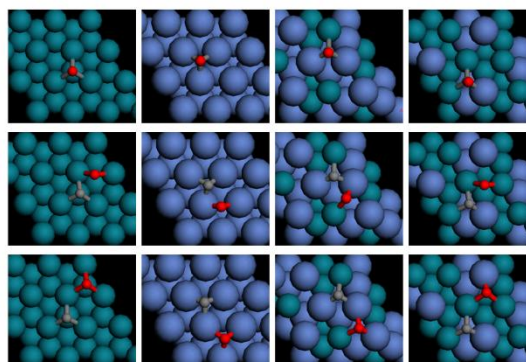
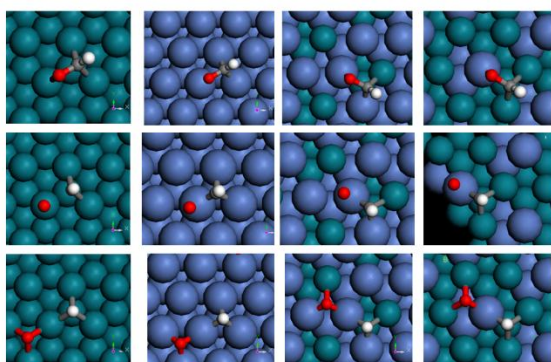
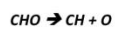
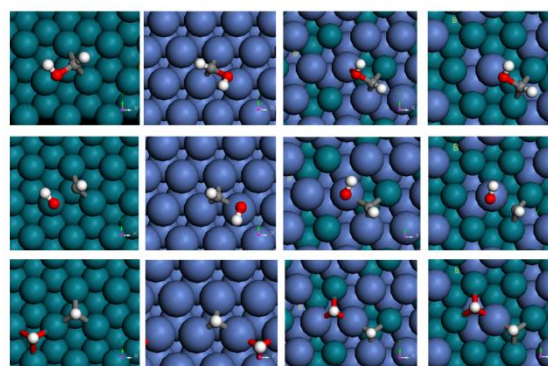
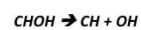
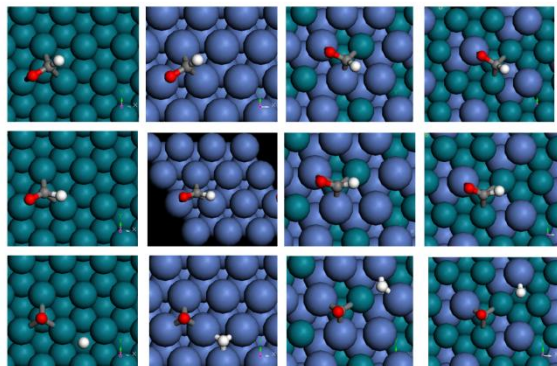
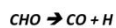
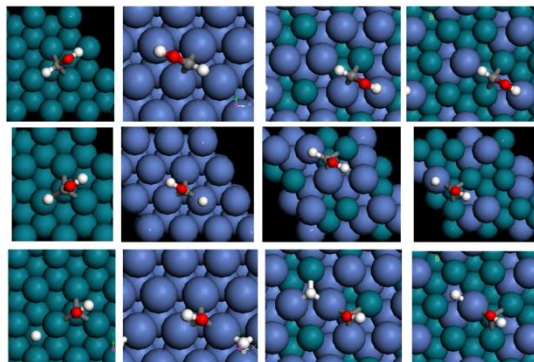
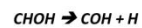
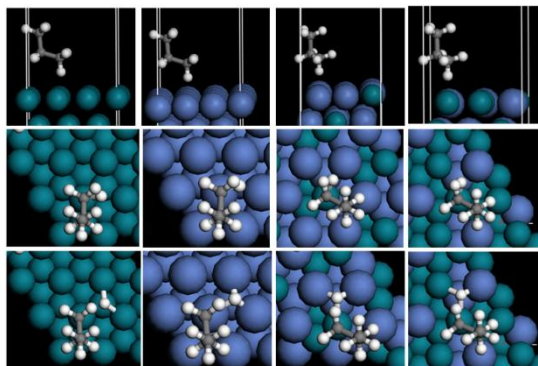
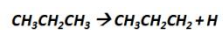
#### 4.5 References

- (1) Bshish, A.; Yakoob, Z.; Narayanan, B.; Ramakrishnan, R.; Ebshish, A. *Chem Pap* **2011**, 65, 251.
- (2) Dal Santo, V.; Gallo, A.; Naldoni, A.; Guidotti, M.; Psaro, R. *Catal Today* **2012**, 197, 190.
- (3) Armor, J. N. *Appl Catal a-Gen* **1999**, 176, 159.
- (4) Sehested, J. *Catal Today* **2006**, 111, 103.
- (5) Galea, N. M.; Lo, J. M. H.; Ziegler, T. *J Catal* **2009**, 263, 380.
- (6) Xie, C.; Chen, Y. S.; Li, Y.; Wang, X. X.; Song, C. S. *Appl Catal a-Gen* **2011**, 394, 32.
- (7) Kugai, J.; Velu, S.; Song, C. S. *Catal Lett* **2005**, 101, 255.
- (8) Kugai, J.; Subramani, V.; Song, C. S.; Engelhard, M. H.; Chin, Y. H. *J Catal* **2006**, 238, 430.
- (9) Li, Y.; Wang, X. X.; Xie, C.; Song, C. S. *Appl Catal a-Gen* **2009**, 357, 213.
- (10) Strohm, J. J.; Zheng, J.; Song, C. S. *J Catal* **2006**, 238, 309.
- (11) Lee, K.; Song, C. S.; Janik, M. J. *Appl Catal a-Gen* **2010**, 389, 122.
- (12) Selvavathi, V.; Chidambaram, V.; Meenalkshisundaram, A.; Sairam, B.; Sivasankar, B. *Catal Today* **2009**, 141, 99.
- (13) Lakhapatri, S. L.; Abraham, M. A. *Appl Catal a-Gen* **2009**, 364, 113.
- (14) Lee, K.; Song, C. S.; Janik, M. J. *Langmuir* **2012**, 28, 5660.
- (15) Rothamer, D. A.; Murphy, L. *P Combust Inst* **2013**, 34, 3021.

- (16) Lin, S.; Xie, D. Q.; Guo, H. *J Phys Chem C* **2011**, *115*, 20583.
- (17) Blaylock, D. W.; Zhu, Y. A.; Green, W. H. *Top Catal* **2011**, *54*, 828.
- (18) Ribeiro, R. U.; Liberatori, J. W. C.; Winnishofer, H.; Bueno, J. M. C.; Zanchet, D. *Appl Catal B-Environ* **2009**, *91*, 670.
- (19) Evans, M. G.; Polanyi, M. *T Faraday Soc* **1938**, *34*, 0011.
- (20) Norskov, J. K.; Bligaard, T.; Logadottir, A.; Bahn, S.; Hansen, L. B.; Bollinger, M.; Bengaard, H.; Hammer, B.; Sljivancanin, Z.; Mavrikakis, M.; Xu, Y.; Dahl, S.; Jacobsen, C. J. H. *J Catal* **2002**, *209*, 275.
- (21) Loffreda, D.; Delbecq, F.; Vigne, F.; Sautet, P. *Angew Chem Int Edit* **2009**, *48*, 8978.
- (22) Saliccioli, M.; Stamatakis, M.; Caratzoulas, S.; Vlachos, D. G. *Chem Eng Sci* **2011**, *66*, 4319.
- (23) Ferrin, P.; Simonetti, D.; Kandoi, S.; Kunkes, E.; Dumesic, J. A.; Norskov, J. K.; Mavrikakis, M. *J Am Chem Soc* **2009**, *131*, 5809.
- (24) Abild-Pedersen, F.; Greeley, J.; Studt, F.; Rossmeisl, J.; Munter, T. R.; Moses, P. G.; Skulason, E.; Bligaard, T.; Norskov, J. K. *Physical Review Letters* **2007**, *99*.
- (25) Jones, G.; Studt, F.; Abild-Pedersen, F.; Norskov, J. K.; Bligaard, T. *Chem Eng Sci* **2011**, *66*, 6318.
- (26) Saliccioli, M.; Chen, Y.; Vlachos, D. G. *J Phys Chem C* **2010**, *114*, 20155.
- (27) Jones, G.; Bligaard, T.; Abild-Pedersen, F.; Norskov, J. K. *J Phys-Condens Mat* **2008**, *20*.
- (28) Wang, S. G.; Temel, B.; Shen, J. A.; Jones, G.; Grabow, L. C.; Studt, F.; Bligaard, T.; Abild-Pedersen, F.; Christensen, C. H.; Norskov, J. K. *Catal Lett* **2011**, *141*, 370.
- (29) Andersson, M. P.; Bligaard, T.; Kustov, A.; Larsen, K. E.; Greeley, J.; Johannessen, T.; Christensen, C. H.; Norskov, J. K. *J Catal* **2006**, *239*, 501.
- (30) Studt, F.; Abild-Pedersen, F.; Wu, Q. X.; Jensen, A. D.; Temel, B.; Grunwaldt, J. D.; Norskov, J. K. *J Catal* **2012**, *293*, 51.
- (31) Blaylock, D. W.; Ogura, T.; Green, W. H.; Beran, G. J. O. *J Phys Chem C* **2009**, *113*, 4898.

- (32) Chen, Y.; Vlachos, D. G. *J Phys Chem C* **2010**, *114*, 4973.
- (33) Yang, M. L.; Zhu, Y. A.; Fan, C.; Sui, Z. J.; Chen, D.; Zhou, X. G. *J Mol Catal a-Chem* **2010**, *321*, 42.
- (34) Yang, M. L.; Zhu, Y. A.; Fan, C.; Sui, Z. J.; Chen, D.; Zhou, X. G. *Phys Chem Chem Phys* **2011**, *13*, 3257.
- (35) Kresse, G.; Hafner, J. *Physical Review B* **1993**, *47*, 558.
- (36) Kresse, G.; Furthmuller, J. *Computational Materials Science* **1996**, *6*, 15.
- (37) Kresse, G.; Furthmuller, J. *Physical Review B* **1996**, *54*, 11169.
- (38) Perdew, J. P.; Chevary, J. A.; Vosko, S. H.; Jackson, K. A.; Pederson, M. R.; Singh, D. J.; Fiolhais, C. *Physical Review B* **1992**, *46*, 6671.
- (39) Perdew, J. P.; Burke, K.; Ernzerhof, M. *Physical Review Letters* **1996**, *77*, 3865.
- (40) Blochl, P. E. *Physical Review B* **1994**, *50*, 17953.
- (41) Donnay, J. D. H.; Ondik, H. M.; United States. National Bureau of Standards. *Crystal data; determinative tables*; 3d ed.; National Bureau of Standards: Washington, 1972.
- (42) Guo, J. H.; Xie, C.; Lee, K. T.; Guo, N.; Miller, J. T.; Janik, M. J.; Song, C. S. *Acs Catal* **2011**, *1*, 574.
- (43) Mills, G.; Jonsson, H.; Schenter, G. K. *Surf Sci* **1995**, *324*, 305.
- (44) Henkelman, G.; Uberuaga, B. P.; Jonsson, H. *J Chem Phys* **2000**, *113*, 9901.
- (45) Henkelman, G.; Jonsson, H. *J Chem Phys* **2000**, *113*, 9978.
- (46) Jiang, R. B.; Guo, W. Y.; Li, M.; Fu, D. L.; Shan, H. H. *J Phys Chem C* **2009**, *113*, 4188.
- (47) Wang, S. G.; Cao, D. B.; Li, Y. W.; Wang, J. G.; Jiao, H. J. *Surf Sci* **2009**, *603*, 2600.
- (48) Sutton, J. E.; Vlachos, D. G. *J Catal* **2013**, *297*, 202.

## 4.6 Supporting Information





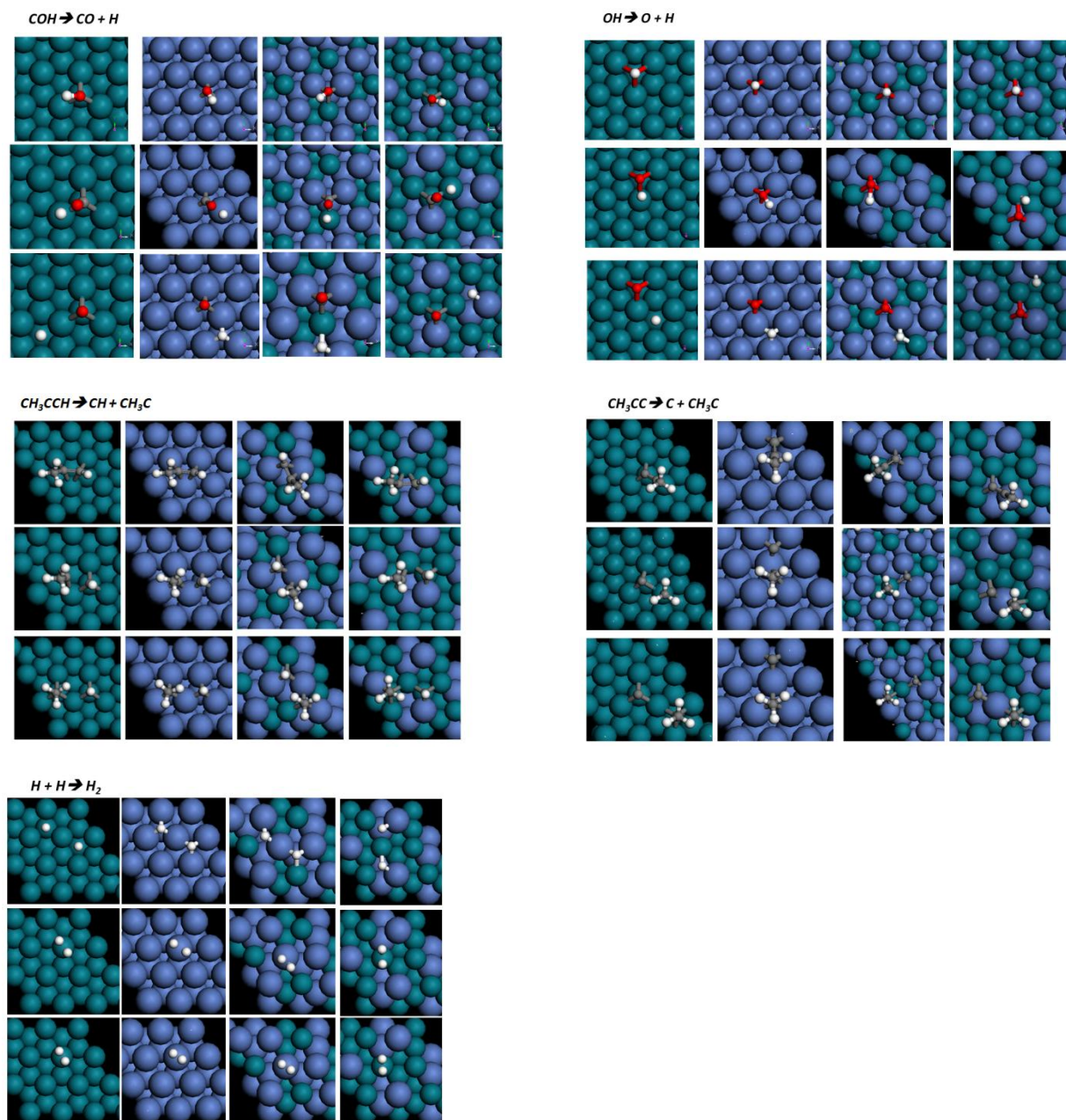


Figure S1. Initial (top), transition (middle), and final (bottom) states on the Rh (left), Ni (middle left),  $\text{Rh}_1\text{Ni}_2$  (middle right), and  $\text{Rh}_2\text{Ni}_1$  (right) surfaces for the reactions titled at each set of figures. Dark-gray spheres (green), Rh; large light-gray sphere (blue), Ni; small light-gray spheres (gray), C; dark sphere (red), O; white spheres (white), H.

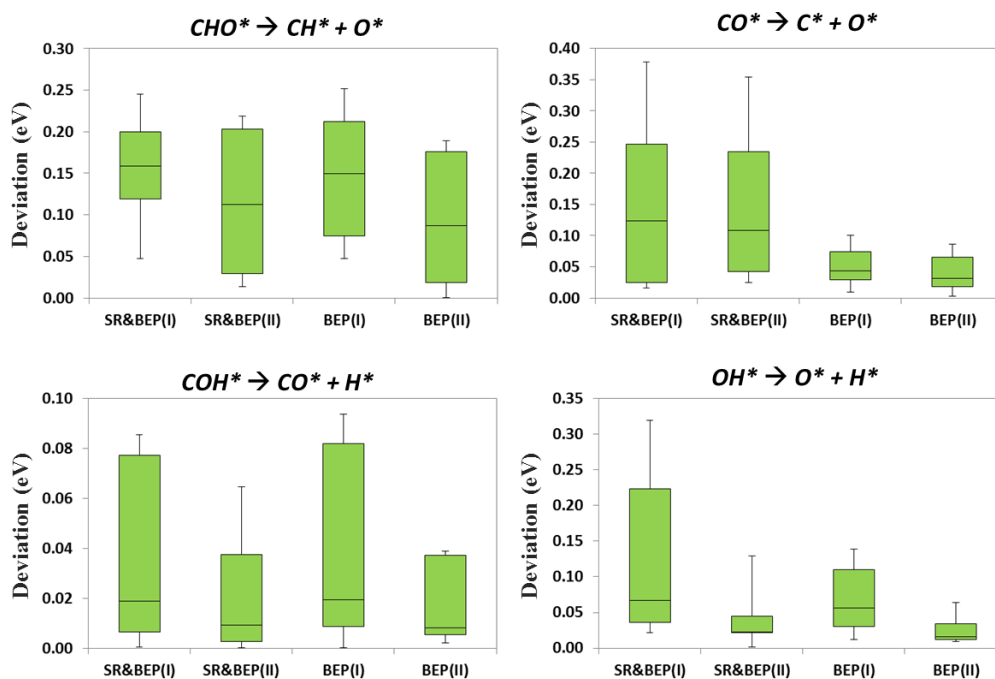
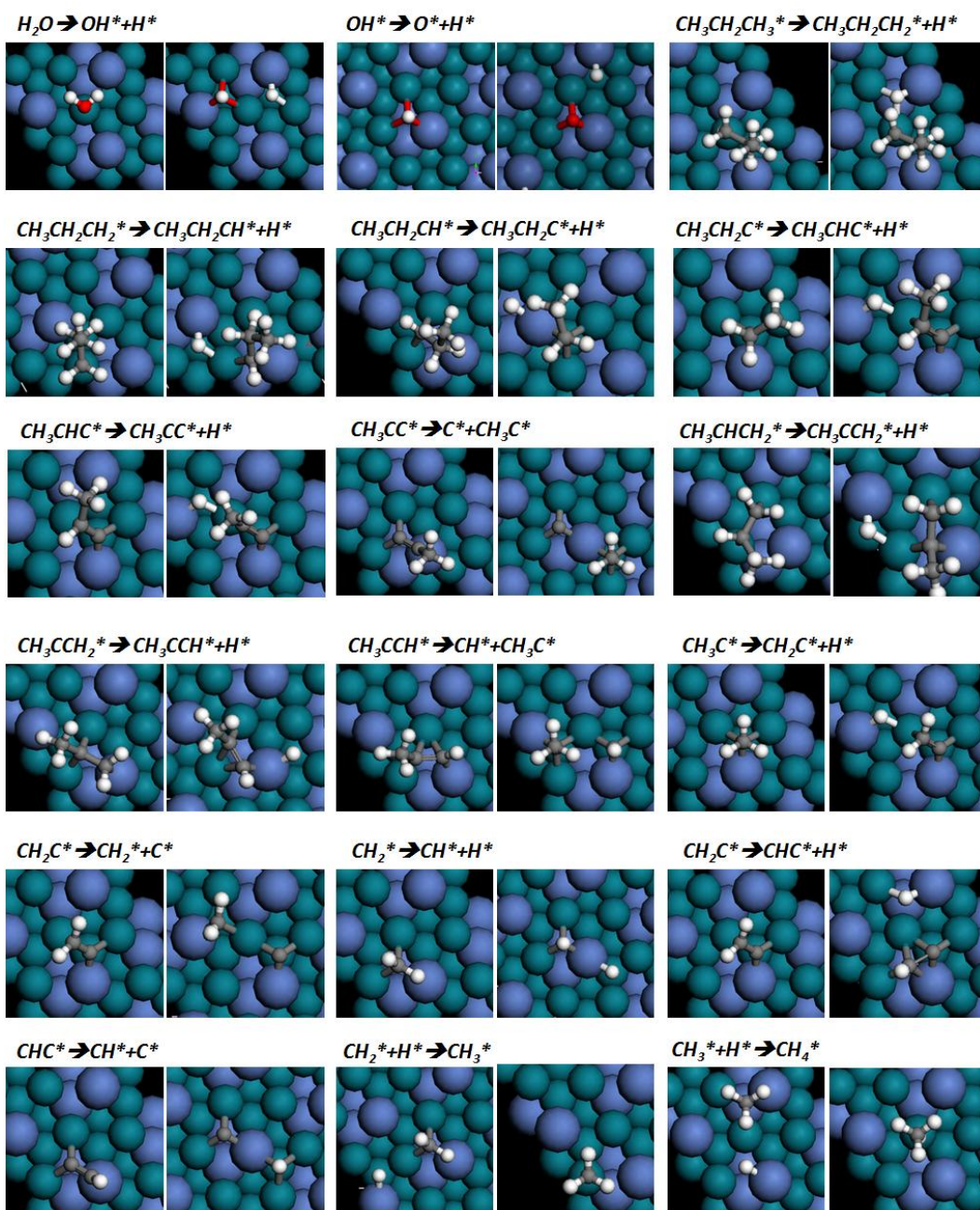


Figure S2. Deviation of activation barriers estimated by various estimation methods from DFT  $E_a$  values calculated by the NEB method on each metal. SR, scaling relations; BEP(I), use of an identical BEP relation for all metals for a given reaction type; BEP(II), use of a different BEP relation for each metal for a given reaction type.





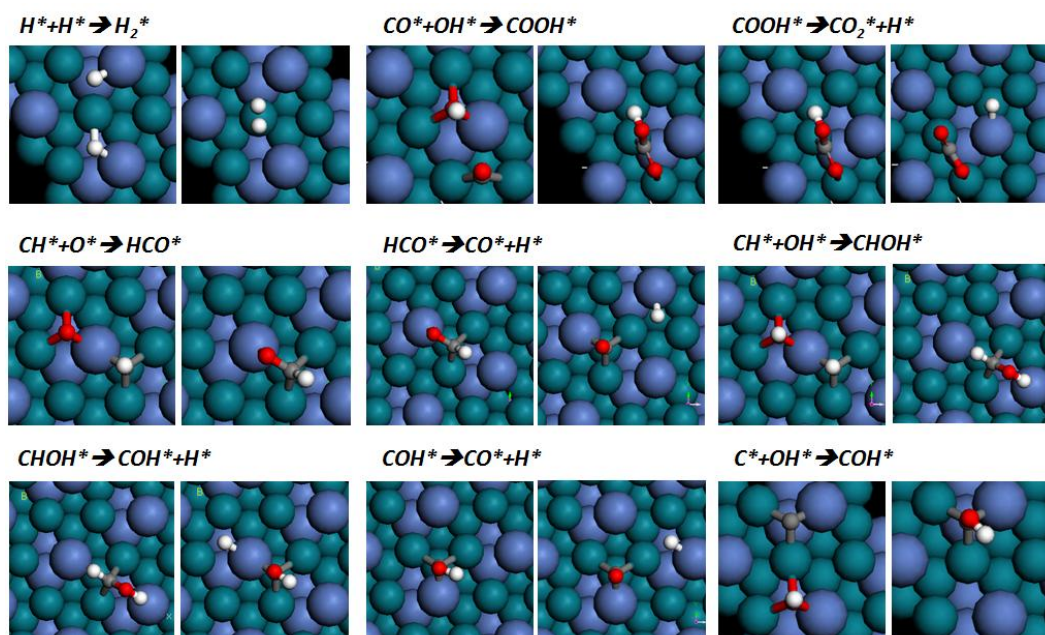


Figure S3. Initial (left) and final (right) states of the elementary steps listed in Figure 4-7. Dark-gray spheres (green), Rh; large light-gray sphere (blue), Ni; small light-gray spheres (gray), C; dark sphere (red), O; white spheres (white), H.

Table S1. BEP relations based on a single BEP over all metals for a given reaction type where  $a$  and  $b$  indicate slope and intercept in a BEP plot, respectively.

Reaction type	elementary steps used	BEP type	$a$	$b$	$R^2$
C-H	$\text{CH}_3\text{CH}_2\text{CH}_3^* = \text{CH}_3\text{CH}_2\text{CH}_2^* + \text{H}^*$ $\text{CHO}^* = \text{CO}^* + \text{H}^*$ $\text{CHOH}^* = \text{COH}^* + \text{H}^*$	$E_{TS}$ vs $E_{FS}$	0.406	0.227	0.93
C-C	C-C dissociation of propyne and propynyl	$E_{TS}$ vs $E_{IS}$	2.972	3.533	0.82
O-H	$\text{COH}^* = \text{CO}^* + \text{H}^*$ and $\text{OH}^* = \text{O}^* + \text{H}^*$	$E_{TS}$ vs $E_{IS}$	1.159	1.163	0.95
C-O	$\text{CHO}^* = \text{CH}^* + \text{O}^*$ $\text{CO}^* = \text{C}^* + \text{O}^*$	$E_a$ vs $E_{rxn}$	0.509	2.122	0.94
C-OH	$\text{CHOH}^* = \text{CH}^* + \text{OH}^*$ $\text{COH}^* = \text{C}^* + \text{OH}^*$	$E_a$ vs $E_{rxn}$	0.939	1.093	0.95

## Chapter 5

### Summary, Conclusions, and Recommendations for Future Study

#### 5.1 Sulfur poisoning species and sulfur tolerance on Rh-Ni binary catalysts

In Chapter 1, a series of research questions was presented. The work presented in Chapters 2-4 is summarized here, where the conclusions reached are connected directly to the list of research questions and the answers for each question are listed in section 5.3. Density functional theory (DFT) was used in this dissertation to investigate the sulfur tolerance mechanism of Rh-Ni binary metals by considering four metal surfaces including Rh, Ni, Rh<sub>1</sub>Ni<sub>2</sub>, and Rh<sub>2</sub>Ni<sub>1</sub>. Chapter 3 examines various sulfur poisoning species such as atomic sulfur adsorption, sulfur oxide (SO<sub>x</sub>, x=1~4) formation, and metal sulfide formation by combining DFT energy values and statistical thermodynamic formulas. Sulfidation phase diagrams as a function of temperature and P(H<sub>2</sub>S)/P(H<sub>2</sub>) pressure ratio on the (111) surfaces show that sulfur adsorption is a thermodynamically preferred sulfur poisoning species under steam reforming conditions. The metal sulfides (i.e., Ni<sub>3</sub>S<sub>2</sub> and Rh<sub>17</sub>S<sub>15</sub>) form at temperatures below 500 K and sulfur oxide formation is not thermodynamically preferred at any temperatures and H<sub>2</sub>S pressures considered. The possibility of sulfur oxide formation is also probed by considering a wide range of H<sub>2</sub>O pressures and different structures such as the Rh(221) stepped surface and the interface between a Rh cluster and ceria support, however the preference for S adsorption is not altered. Thus, the ab initio thermodynamic analysis suggests that the sulfur poisoning species during steam reforming is surface adsorbed S atoms, and their co-adsorption may then affect the reactivity of other adsorbates. The analysis of O 2p projected density of state in Chapter 2 reveals that the

electronic repulsion between co-adsorbed S and reactant CO is reduced on the  $\text{Rh}_1\text{Ni}_2(111)$  surface compared to the Rh(111) surface, indicating that the sulfur poisoning effect through S adsorption is minimized on binary Rh-Ni surfaces. As a result, the activation barrier increase of CO dissociation by co-adsorbed S is retarded on the  $\text{Rh}_1\text{Ni}_2(111)$  surface in contrast to the Rh(111) surface showing a dramatic increase.

Chapter 2 compares the binding energies of sulfur among metals.  $\text{Rh}_1\text{Ni}_2(111)$  has weaker sulfur binding energy than Rh(111), suggesting a lower sulfur coverage on binary Rh-Ni metals. Chapter 3 details sulfur coverages of each metal by constructing sulfur coverage phase diagrams as a function of operating conditions. The  $\text{Rh}_1\text{Ni}_2(111)$  surface experiences a phase transition from a clean surface ( $< 1/9$  ML) to S adsorption at lower temperatures and higher  $\text{H}_2\text{S}$  pressures than the Rh (111) surface, indicating a higher sulfur tolerance on  $\text{Rh}_1\text{Ni}_2(111)$  with respect to sulfur coverage. The specific experimental conditions (4, 33, 100 ppm S at 500 or 800  $^{\circ}\text{C}$ ) are examined in a sulfur coverage phase diagram including various sulfur coverage transitions. The sulfur coverage of  $\text{Rh}_1\text{Ni}_2(111)$  is  $1/9$  ML at higher than 800  $^{\circ}\text{C}$  and less than 33 ppm S, whereas Rh(111) remains at  $1/3$  ML sulfur coverage. The results presented in Chapter 2 and 3 suggest that Rh-Ni binary catalysts provide a sulfur tolerance by lowering sulfur coverage on catalyst surfaces and reducing electronic interactions between co-adsorbed sulfur atoms and reactants as comparison with a pure Rh catalyst.

## 5.2 Propane steam reforming on sulfur tolerant Rh-Ni binary catalysts

The sulfur tolerance on Rh-Ni binary surfaces is examined in Chapter 2 with the CO dissociation step by comparing sulfur-free and sulfur-present conditions. The CO dissociation rate is fastest on pure Rh(111) under a sulfur-free condition, but fastest on Rh<sub>1</sub>Ni<sub>2</sub>(111) under a sulfur-poisoned condition. The dissociation rate of CO is determined by two factors, the adsorption energy of CO and the activation barrier of CO dissociation. The fastest CO dissociation rate on Rh<sub>1</sub>Ni<sub>2</sub>(111) in the presence of sulfur correlates with its low activation barrier rather than CO binding strength. This is also found in a comparison between the Rh<sub>1</sub>Ni<sub>2</sub>(221) and the Rh(221) stepped surfaces. The kinetic aspect of the sulfur tolerant CO dissociation is in line with Chapter 4 which examines the elementary steps of propane steam reforming. In Chapter 4, the significant reaction paths of propane steam reforming are selected from the complex reforming reaction network using previous computational studies and all the potential energy surfaces of the selected elementary steps are estimated by BEP relations using DFT-calculated binding energies of each intermediate. The error analysis of estimation methods indicates that the combined use of scaling and BEP relations is not acceptable over similar metal surfaces from pure Rh, Ni to binary Rh-Ni metals, thus BEP relations only are used for the energetic prediction of propane reforming.

All the potential energy surfaces predicted by BEP relations isolates four elementary steps with relatively high activation barriers which are the C-C cleavages of CHC\* and CH<sub>3</sub>CC\*, O addition to CH\*, and C-C cleavage of CH<sub>2</sub>C\*. For all the four elementary steps, the Rh<sub>2</sub>Ni<sub>1</sub>(111) surface has the lowest activation barrier under a sulfur-poisoned condition. The analysis of average sulfur poisoning impact on activation barriers of all the elementary steps of

propane reforming shows that the destabilization of activation barriers is minimized on the  $\text{Rh}_2\text{Ni}_1(111)$  surface. This trend is also found in the most critical two elementary steps, the C-C cleavages of  $\text{CHC}^*$  and  $\text{CH}_3\text{CC}^*$ . This is consistent with the result of Chapter 2 where the destabilization in the activation barrier of CO dissociation under sulfur-poisoned conditions is retarded on  $\text{Rh}_1\text{Ni}_2(111)$ , leading to the lowest activation barrier among surfaces considered. In summary, the results of Chapter 2-4 show that the  $\text{Rh}_1\text{Ni}_2$  binary surface lowers sulfur coverage and the  $\text{Rh}_2\text{Ni}_1$  binary surface retards the deactivation in the activation barriers of reforming reactions due to sulfur poisoning. Therefore, the studies in this dissertation suggest that sulfur compounds in liquid fuels are less likely to form co-adsorbed sulfur atoms on Rh-Ni binary catalysts and the kinetics of steam reforming reactions is faster on Rh-Ni binary catalysts than pure Rh catalysts under sulfur poisoning conditions.

### 5.3 Answers for Research Questions

1) Why do Rh-Ni binary catalysts maintain the catalytic activity for methane formation under sulfur poisoning condition while the methane selectivity is rapidly dropped on the Rh catalyst?

*Answer)* Rh-Ni binary surfaces are less covered by S atoms and retard an increase in the activation barriers for methane formation by sulfur poisoning.

2) Why is the sulfur poisoning impact of co-adsorbed sulfur atom reduced on Rh-Ni binary metals compared to pure Rh?

*Answer)* Rh-Ni binary surfaces reduce electronic interactions between reactants and co-adsorbed sulfur atoms as compared to a Rh surface.

3) Is there any difference in sulfur poisoning species and their surface coverage between pure metals and Rh-Ni binary metals under reforming conditions?

*Answer)* There is no difference in sulfur poisoning species among surfaces. Sulfur adsorption is the thermodynamically favorable sulfur poisoning path on four surfaces under steam reforming conditions. The surface sulfur coverage on bimetallic Rh-Ni is less than on pure Rh. For example, Rh<sub>1</sub>Ni<sub>2</sub>(111) is covered with 1/9 ML of sulfur at 800 °C and less than 33 ppm S, whereas Rh(111) is covered with 1/3 ML of sulfur at the identical conditions.

4) Which elementary steps and surface intermediates are critical in the propane steam reforming reaction?

*Answer)* There are four critical elementary steps with relatively high activation barriers; the C-C cleavages of CHC\* and CH<sub>3</sub>CC\*, O addition to CH\*, and C-C cleavage of CH<sub>2</sub>C\*. Two of them, O addition to CH\* and C-C cleavage of CH<sub>2</sub>C\*, pertain to the energetically most preferred reaction paths of propane steam reforming. A future microkinetic analysis will identify critical surface intermediates.

5) Do Rh-Ni binary metals provide higher sulfur tolerance for the energetics of either critical steps or the overall reforming reactions?

*Answer)* All the four critical elementary steps mentioned above have the lowest activation barriers on the Rh<sub>2</sub>Ni<sub>1</sub>(111) surface. In overall reforming reactions, the Rh<sub>2</sub>Ni<sub>1</sub>(111) surface offers the lowest destabilization with respect to the average sulfur poisoning impact on activation barriers.

6) What are important factors to design a new sulfur tolerant catalyst?

*Answer)* There are two important factors, sulfur coverage and activation barrier. New sulfur tolerant catalysts are expected to offer either a lower sulfur binding energy or a lower activation barrier in critical elementary steps than binary Rh-Ni surfaces.

#### **5.4 Perspective and Suggestions for Future Study**

This dissertation provides an effective tool for catalyst design by the following stepwise approach: first, the reaction paths of a given chemical process need to be categorized into important and unimportant paths. Second, the potential energy surfaces of reaction paths are predicted by different estimation methods as discussed in Chapter 4 according to the importance of reaction paths. Third, the energetics of the potential energy surfaces is used for microkinetic analysis, thereby identifying key intermediates and elementary steps. Finally, a variety of possible metals for better catalytic performance are investigated based on those intermediates and elementary steps. The selected metals through the whole procedure are finally evaluated by both a microkinetic modeling and an experimental examination.

The microkinetic analysis as a future work prepares a guideline for sulfur tolerant catalyst design. The microkinetic modeling calculates sulfur coverage on each metal surface and identifies significant elementary steps (e.g., the addition of O\* to CH\* and C-C breaking of CH<sub>2</sub>C are expected to be significant according to Chapter 4, but other reactions may more important after the microkinetic analysis) for propane steam reforming to affect fuel conversion and products selectivity. From these results, the sulfur tolerance of Rh-Ni binary metals can be



defined as a function of activation barriers of key elementary steps and surface sulfur coverage, where we can give a weighting for two factors.

This benchmark can be used to initially examine all possible transition metals for a new sulfur tolerant catalyst. For example, one can start with 11 transitional metals examined in a previous computational study of methane steam reforming.<sup>1</sup> If the microkinetic modeling places more weight on the kinetics of key elementary steps than surface sulfur coverage in improving sulfur tolerance, we can decrease the number of interesting transition metals by comparing the activation barriers of the key elementary steps. For this work, the combination of scaling and BEP relations serve as an effective estimation tool. The errors arising from this estimation approach are acceptable for such a wide scan of transition metals. For example, Jones et al. predicted the potential energy surfaces of methane steam reforming on various transition metals using the combination of scaling and BEP relations.<sup>1</sup> If the microkinetic modeling emphasizes sulfur coverage more than the kinetics of key elementary steps, we need to compare sulfur binding energies on the transitional metals considered, some of which can be referred to previous data calculated on 7 transition metals by Alfonso et al.<sup>2</sup>

After using one of two filtering approaches above, we can choose promising transition metals to be expected to derive a stronger sulfur resistance with similar or greater catalytic activity as compared to the Rh, Ni, and Rh-Ni binary metals. Using the transition metals, we can formulate possible bimetallic combinations to have potential in high sulfur tolerance and activity. The energetics of key elementary steps on these binary metals with the pure metals filtered initially are estimated by the use of BEP relations only to increase accuracy as addressed in Chapter 4, thereby adding one more filtering to find promising metals. The screened metals are finally evaluated by microkinetic modeling and compared with the results of Rh-Ni binary

metals. If there is a metal showing a better performance in fuel conversion and products selectivity under sulfur poisoning conditions through the microkinetic analysis than Rh-Ni binary metals, those metals can be tested experimentally in a steam reforming reactor with the feedstock of either propane or jet fuel.

This dissertation discusses the sulfur tolerance mechanism of Rh-Ni binary metals in various aspects and presents a stepwise approach for catalyst development using DFT methods. Future studies will find new sulfur tolerance catalysts and simultaneously offer their sulfur tolerance mechanism based on the computational data with respect to reaction energetics on the metals.

## 5.5 References

- (1) Jones, G.; Jakobsen, J. G.; Shim, S. S.; Kleis, J.; Andersson, M. P.; Rossmeisl, J.; Abild-Pedersen, F.; Bligaard, T.; Helveg, S.; Hinnemann, B.; Rostrup-Nielsen, J. R.; Chorkendorff, I.; Sehested, J.; Norskov, J. K. *J Catal* **2008**, 259, 147.
- (2) Alfonso, D. R. *Surf Sci* **2008**, 602, 2758.

## VITA

### Kyungtae Lee

#### Education

B.S. Chemical Engineering – Seoul National University **2002**

M.S. Chemical Engineering – Seoul National University **2004**

Ph.D. Chemical Engineering – The Pennsylvania State University **2013**

#### Awards and Honors

Catalysis and Reaction Engineering Division at American Institute of Chemical Engineers in Pittsburgh – Travel Award (2012)

Division of Fuel Chemistry at American Chemical Society meeting in San Diego – Travel Award (2012)

PCCS (Pittsburgh-Cleveland Catalysis Society) Symposium – Presentation award (2010)

KIST (Korea Institute of Science and Technology) annual research exhibit – Poster award (2007)

Samsung Electronics HDD (High-Definition Display) center – vice-president award for superior studying group (2004)

#### Publications

1. “Ab Initio Thermodynamics Examination of Sulfur Species Present on Rh, Ni, and Binary Rh–Ni Surfaces under Steam Reforming Reaction Conditions”, **Kyungtae Lee**, Chunshan Song, Michael J. Janik, *Langmuir* 28 (2012) 5660
2. “Expanding the spectral responses of a dye-sensitized solar cell by applying a selective positioning method”, Se Woong Park, **Kyungtae Lee**, Doh-Kwon Lee, Min Jae Ko, Nam-Gyu Park and Kyungkun Kim, *Nanotechnology* 22 (2011) 045201
3. "Improving the Carbon Resistance of Ni-based Steam Reforming Catalyst by Alloying with Rh. A Computational Study Coupled with Reforming Experiments and EXAFS Characterization", Jiahua Guoa, Chao Xie, **Kyungtae Lee**, Neng Guo, Jeffrey T. Miller, Michael J. Janik, Chunshan Song, *ACS Catalysis* 1 (2011) 574
4. “Density functional theory study of sulfur tolerance of CO adsorption and dissociation on Rh-Ni binary metals”, **Kyungtae Lee**, Chunshan Song, Michael J. Janik, *Applied Catalysis A: General* 389 (2010) 122-130
5. “Selective positioning of organic dyes in a mesoporous inorganic oxide film”, **Kyungtae Lee**, Se Woong Park, Min Jae Ko, Kyungkun Kim & Nam-Gyu Park, *Nature Materials* 8, (2009) 665 – 671
6. “Synthesis and characterization of polyaniline nanorods as curing agent and nanofiller for epoxy matrix composite”, Jyongsik Jang, Joonwon Bae, **Kyungtae Lee**, *Polymer* 46 (2005) 3677–3684